UNIVERSITY
OF TRENTO - Italy
Department of Materials Engineering
and Industrial Technologies

Doctoral School in Materials Engineering – XXII cycle

Surface Engineering for Microsensing

Luca Minati

January 2010

Surface Engineering for Microsensing

Author

Minati Luca

Tutors

Prof. Claudio Migliaresi

Dr. Giorgio Speranza

A mio padre

CONTENTS

Thesis Outline

Chapter 1: Introduction

In this chapter the topic of carbon nanotubes and gold nanoparticles is briefly introduced, and the current state of the art is overviewed. The main chemical and physical properties of carbon nanotubes as well as synthesis and functionalization procedures are reported. Regarding gold nanoparticles some general considerations are reported about the optical and chemical properties. At the end of the chapter some analytic techniques used in this Thesis are presented.

Chapter 2: Experimental section

This chapter starts with a brief overview of the synthesis procedure used in each chapter. At the end of the chapter a brief description of the X-ray photoelectron spectroscopy experimental setup are reported, as well as of the principal instruments used in the Thesis work for the sample characterization.

Chapter 3: Functionalization of carbon nanotubes

This chapter describes the characterization procedure and the functionalization processes of multi walled carbon nanotubes. The most relevant results were the high yield of the oxidation of the carbon nanotubes and the high efficiency of grafting of thiol functional groups on the carbon nanotubes surface. This last was verified with different characterization methods. Finally, the interaction of the thiol functionalized carbon nanotubes with gold films and gold nanoparticles was investigated.

Chapter 4: Synthesis and characterization of carbon nanotubes films decorated with gold nanoparticles

In this chapter the carbon nanotubes were deposited on metallic substrates by using an external electric field to induce orientation and migration of the carbon nanotubes in solution toward a chemically modified electrode. The efficiency of the procedure was verified with scanning electron microscopy and atomic force microscopy. The carbon nanotubes films were further decorated with gold nanoparticles deposited by adsorption.
The samples were tested as surface enhanced Raman spectroscopy substrate for the detection of anions in solution.

Chapter 5: optical properties of carbon nanotubes

In this chapter the optical luminescence of functionalized carbon nanotubes and carbon nanotubes gold nanoparticle hybrids are presented. In particular, the carbon nanotubes decorated with gold nanoparticles show a drastic increase of the photoluminescence in solution respect to the carbon nanotubes without the gold nanoparticles. The effect was investigated with the optical spectroscopy and an interpretation of the experimental results is given.

Chapter 6: X-ray photoelectron spectroscopy studies on gold metal nanoclusters/amorphous carbon composite

In this chapter, the characterizations results on gold nanoclusters embedded in a carbon matrix are presented. In particular, the X-ray photoelectron spectroscopy characterization is used to analyze the chemical and structural composition of small gold nanoparticles deposited on carbon. Using a theoretical approach combined to experimental data the size distribution of gold NPs a-C/Au samples is estimated by line-shape analysis of the Au 4f photoemission spectrum. The calculated size distributions are in good agreement with that calculated with different techniques.

Chapter 7: Characterization of Gold nanoclusters synthesized on carbon nanotubes film: evaluation of the size distributions by means of X-ray photoelectron spectroscopy

In this chapter gold nanoclusters are directly synthesized on thiol functionalized carbon nanotubes film and characterized by means of X-ray photoelectron spectroscopy.
Detailed analysis of the Au 4f core line using the methodology presented in the previous chapter is used to study the chemical modifications occurring on the substrate, as well as to obtain information on the nanocluster size distribution after each reducing treatments.

CHAPTER 1

1.1 Introduction to carbon nanotubes

Carbon, because of its electronic configuration is a really versatile element. Pure carbon can assume a few allotropic forms because the four valence electrons can organize with different spatial orientation on the basis of their hybridization. Diamond and graphite are examples of sp3 and sp2 hybridizations (upper left and right in figure 1.1) leading to distinct optical, electrical and mechanical properties. The organization of s and p electrons in sp2 hybrids enables carbon atoms to generate other unique structures. The C60 buckyball (lower left in figure 1.1) was discovered in 1985 by Kroto et al [1]. The carbon nanotubes (lower right in figure 1.1) were discovered in 1991 by Iijima [2]. These carbon structures that couple quantum effects, lower dimensionality and the unique properties of graphene [3, 4] have generated intense research in the material science.

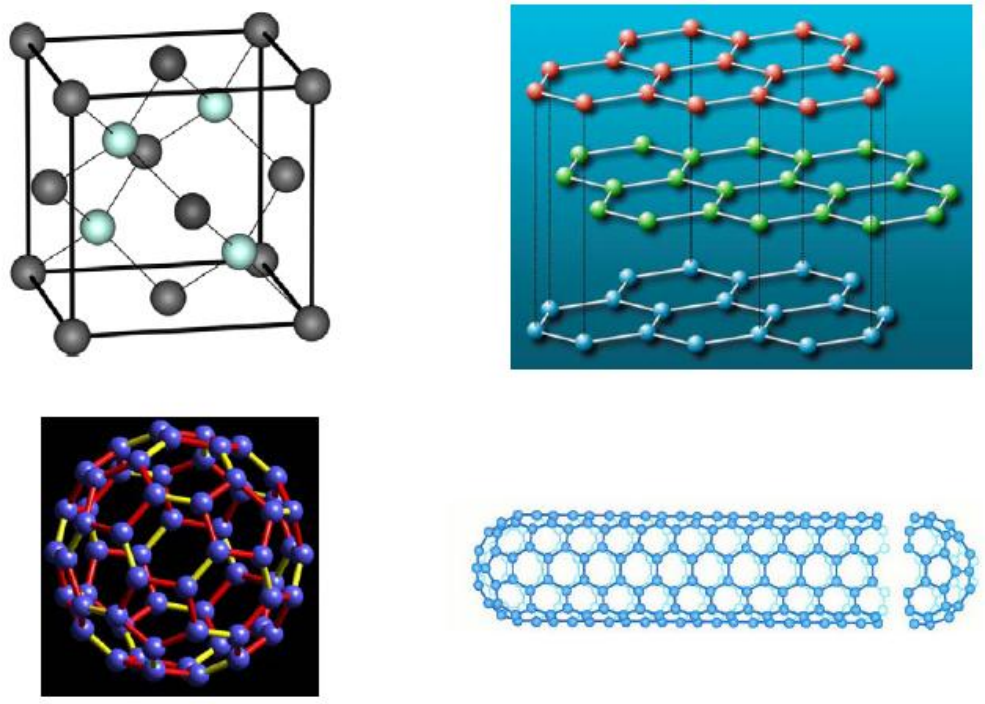

Figure 1.1. *Models of carbon allotropes. From top left: diamond, graphite, nanotube, C60 buckyball (staff.science.uva.nl)*

1.1.1 Structure of nanotubes and characterization methods

The structure of nanotubes originates from that of graphite. Here electrons are organized in wavefunctions lying in a plane and along directions making angles of 120°. This causes the carbon atoms to arrange in hexagons in two-dimensional sheets overlapped each other in a stack leading to the crystalline structure of graphite. The single sheet of graphite is called graphene. A single-walled nanotubes (SWNTs) can be ideally obtained by rolling up a graphene sheet. When more sheets are rolled up together, the nanotube is called multi-walled. They are composed by concentric cylinders of graphene layers.

Multi-walled nanotubes dimensions are typically larger than SWNTs which diameter are in the range of few nanometers. There are plenty of techniques to characterize CNT on the basis of the information desired: the scanning electron microscope (SEM), scanning tunneling microscope (STM), atomic force microscope (AFM) and transmission electron microscopy (TEM) to characterize their structure.

XPS, FTIR, to study the chemistry behind CNT functionalization and processing. CNTs can be produced in many ways, either as a chemical reaction (chemical vapor deposition) or a physical process (arc discharge and laser ablation). Each individual nanotube can be uniquely identified with three quantities: nanotube diameter, chirality and number of walls. These parameters will be briefly introduced in the following of this section, along with methods for their characterization.

Diameter

TEM is the best analytic technique to measure the carbon nanotubes diameter, but its use is limited to suspended nanotubes. AFM suffer from some problems related to the limited tip curvature that leads to an overestimation of the nanotubes diameters. Raman spectroscopy is another tool to measure small SWNTs. The radial breathing mode (RBM) phonons, where all carbon atoms oscillate radially with the same phase, generate a strong peak in Raman spectroscopy at around 200 cm^{-1}. The peak position, being inversely proportional to tube diameter allows its estimation.

Number of walls

The best analytic technique to discriminate between single and multi walled carbon nanotubes is TEM. On the other hands TEM require carbon nanotubes in suspensions. When nanotubes are integrated into devices however, they are typically sitting on substrates, making TEM unable to be used in these experiments.

Chirality

When the graphitic sheet is rolled up along the symmetry axis Z to form the CNT, the hexagons may be organized in a spiral mode. The chirality describes the inclination of the hexagon spiral along Z. Chirality is more difficult to probe because it comes from atomic scale details. STM has been shown to be the best technique to resolve the arrangement of carbon in SWNTs [5, 6] but it is rather complex and requires conductive substrates.

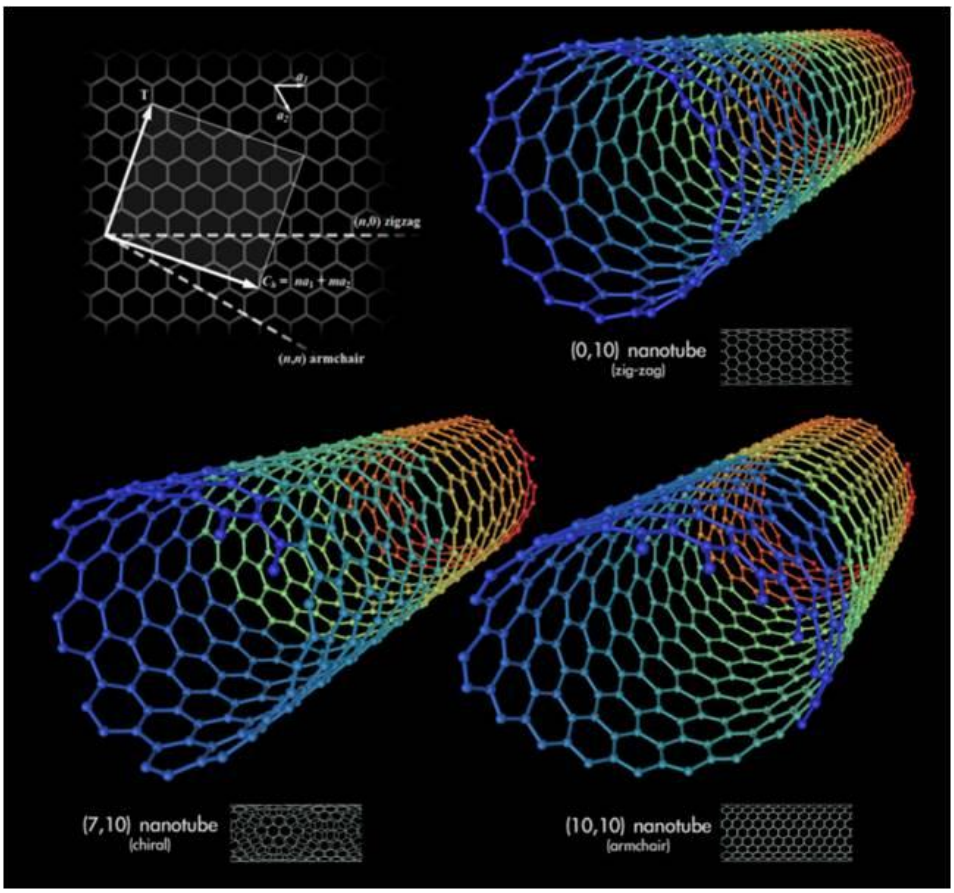

Figure 1.2. *Scheme of the chirality for single-walled carbon nanotubes.*

Another possibility is to use Raman spectroscopy. When the diameter of a nanotube is small, a precise measurement of diameter can reveal also its chirality since there is one-to-one correspondence between these two quantities. The RBM peak positions in Raman can be used as the most accurate way to measure tube diameter and thus chirality [7].

Defects

STM is the best analyric technique to detect defects in SWNTs [8]. Another possibility is the Raman spectroscopy [9]. When defects are present in the carbon nanotubes, the D-band, typical around 1340 cm^{-1} in Raman spectroscopy appears. The presence of defects may lead to a change in the electronic band structure on the SWNT , leading to a modification of RBM peak magnitude.

1.1.2 Properties of nanotubes and potential applications

The unique electronic, mechanical and biological properties of the carbon nanotubes along with potential applications will be presented in this section. Besides them, the small size of nanotubes also leads to many unique advantages that will also be discussed.

Electronic properties

SWNTs have interesting electrical properties. These arise from quantization effects due to the reduction from a macroscopic three-dimensional system to one having one infinite dimension and the remaining two measurable on an atomic scale. SWNTs are made of graphene, which has high intrinsic electron mobility [4] due to the lack of lattice defects as compared to most other semiconductor materials. In SWNT situation is different. Their diameters are too small that the electron wave vectors along the circumferences are quantized leading to a series of sub-bands in the electronic structure. It also makes SWNTs either metallic or semiconducting depending on their chirality. SWNTs have remarkable electrical performances. Defect-free SWNTs can have mobility larger than 10.000 cm^2V/S^{-1}. The band structure and one dimensionality also make carbon nanotubes a unique optoelectronic material. The electron density of states in nanotubes has a number of singularities, associated with the onsets of sub

bands (Van Hove singularity see figure 1.3). Therefore, nanotubes can be viewed as semiconductors with multiple bandgaps, which can efficiently absorb lights of a wide spectrum [10]. Thanks to the electronic structure CNT are luminescent in the UV, visible and the infrared regions, each of these transition are strictly related to band-band transitions. The first observation of intrinsic luminescence is due to O'Connel et al. in nanotubes isolated in SDS aqueous micelles [11]. Since then, luminescence of SWCNTs has been confirmed by other groups for single self-suspended nanotubes grown between catalyst pillars by chemical vapor deposition technique [12]. Indeed, it is possible to observe SWCNTs luminescence at room temperature in various conditions as far as tubes are isolated.

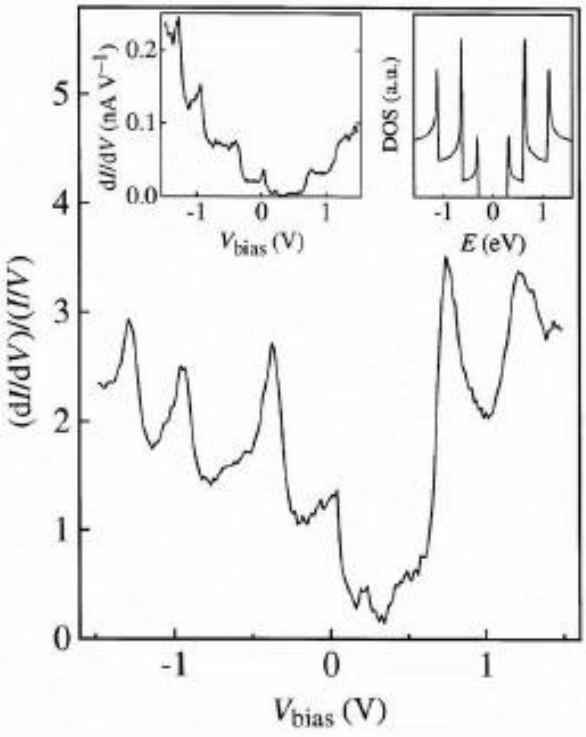

Figure 1.3. *(dI/dV)/(I/V) measure of the density of states versus V. The asymmetric peaks correspond to Van Hove singularities of the carbon nanotube. The left-inset displays the dI/dV data. The right inset is the calculated density of states (DOS) for a (16,0) tube.[6]*

Mechanical properties

The utility of nanotubes as the strongest or stiffest elements in nanoscale devices or composite materials remains a powerful motivation for the research in this area. The Young's modulus of nanotubes (~ 1TPa) is five times higher than that of steel [13]. The largest experimental value observed for MWNTs is about 60GPa [14]. In comparison, the tensile strength of steel is less than 1GPa. At the same time, CNTs are extremely light.

Chemical properties

Because of their molecular-scale size, carbon nanotubes are sensitive to environments. Defect-free SWNTs are chemically inert. SWNTs are ideal materials to make detectors that are capable to reach single-molecule level sensitivity [15]. Potential applications are not limited to sensors. SWNTs have large surface to volume ratio which makes them an interesting material as electrodes in electrochemistry [16]. The high stability of SWNTs renders them appealing as hydrogen storage candidates [17]. Finally, SWNTs has been used as carriers for cells drug delivery [18]. However, there are some concerns regarding the toxicity of SWNTs induced by the easy internalization in cells. Recent studies showed that SWNTs injected in mice could be excreted within a couple months [18] without any toxic effect.

1.1.3 Nanotube Growth Methods

Arc-discharge and laser ablation methods have been actively used in the past ten years for the nanotubes growth. They all involve sublimating graphite in a reduced atmosphere or rare (inert) gases, brought to temperatures above 3200°C that is the sublimation temperature of graphite and condensing the resulting vapour under a high temperature gradient.

Arc-Discharge and Laser Ablation

An arc discharge is generated between two graphite electrodes placed face to face in the machine's principal airtight chamber under a partial pressure of helium or argon.
Arc-discharge is an excellent method for producing both high quality multi-walled nanotubes and single-walled nanotubes. MWNTs can be obtained by controlling the growth conditions such as the pressure of inert gas in the discharge chamber. [19]
The laser ablation technique is rather similar to the arc method as it also consists of sublimating graphite in a reduced atmosphere and has been proven to lead to very similar structures to those obtained by the arc method.
Ablation of a graphite target with a focused laser beam is realized in an inert atmosphere at low pressure [20]. The growth of high quality SWCNTs was achieved by Smalley and co-

workers using a laser ablation method [21]. The method utilizes intense laser pulses to ablate a carbon target containing 0.5 atomic percent of nickel and cobalt. The target is placed in a tube-furnace heated to about 1200°C. During laser ablation, a flow of inert gas passes through the growth chamber to carry the grown nanotubes downstream to be collected on a cold finger.

Catalytic CVD Growth

Catalytic Chemical Vapor Deposition (CVD) processes make possible the growth of carbon filaments of various sizes and shapes at low temperature (≤1000 °C) from carbon-containing gaseous compounds, which decompose catalytically on transition-metal particles [22, 23]. CVD growth relies on the capability to provide the atoms needed to form the solid deposit from a gas source that decomposes under the action of temperature.

The growth process involves heating a catalyst material to high temperatures in a tube furnace and flowing a hydrocarbon gas through the tube reactor for a period of time. Materials grown over the catalyst are collected upon cooling the system to room temperature. The key parameters in nanotubes CVD growth are the hydrocarbons, catalysts and growth temperature. The active catalytic species are typically transition-metal nanoparticles formed on a support material such as alumina. The general nanotube growth mechanism in a CVD process involves the dissociation of hydrocarbon molecules catalyzed by the transition metal and dissolution and saturation of carbon atoms in the metal nanoparticles. The precipitation of carbon from the saturated metal particle leads to the formation of tubular carbon solids in *sp*2 structure. Tubule formation is favored over other forms of carbon such as graphitic sheets with open edges.

1.1.4 Carbon nanotubes modification

Purification

A large problem with nanotube application is next to large-scale synthesis also the purification. The as-produced SWNT soot contains a lot of impurities. The main impurities in the soot are graphite sheets, amorphous carbon, metal catalyst and the smaller fullerenes.

Purification may consist of controlled oxidation, by mean of chemical, [24] or plasma treatments [25]. Chemical oxidation, among the other purification systems, can create terminal and surface defects readily saturated by oxygen-containing functional groups such as, for example, -COOH allowing further functionalization. Refluxing in dilute nitric acid can be considered as a mild oxidation for CNTs, introducing the carboxylic acid groups only at those defects initially present on the carbon nanotubes. The atomic abundance of the carboxylic groups generated with this oxidant remains constant along with the treating time. The oxidation processes begin mainly with the oxidation of the initial defects that arise during the growth of the CNTs and are accompanied by processes that can be roughly divided into two steps: (1) the defect-generating step and (2) the defect-consuming step.

Specifically, during the defect-generating step, the oxidation agents attack the carbon nanotubes skeleton and generate oxygen-containing functional groups such as -OH and –C=O. The rate of the reaction depends on the oxidants ability to generate -C-OH groups and to transform them into –C=O groups. During the defect-consuming step, the graphene structure of the tube is destroyed by the oxidation of the generated active sites. The defect-consuming step mostly counts on the ability of the oxidant to etch/destroy the graphite-like structure around the functional groups.

The sulphuric and nitric acid mixture (normally 1:3 HNO_3/H_2SO_4) is normally used to introduce a high amount of defect and functional groups in the carbon nanotubes [26], as well as to reduce the carbon nanotubes length.

Functionalization

Functionalization is based on making SWNTs more soluble than the impurities by attaching other groups to the tubes. Now it is easy to separate them from insoluble impurities, such as metal, with filtration.

The lack of solubility and the difficult manipulation of carbon nanotubes cause some limitations to their use. Indeed, as-produced CNTs are insoluble in all organic solvents and aqueous solutions. This is the reason beyond the interest in investigating the CNT functionalization even before potential applications.

It was demonstrated that CNTs could interact with different classes of compounds [27] forming supramolecular complexes or undergo regular chemical reactions. This makes them more soluble, so improving their integration into inorganic, organic, and biological systems. The main approaches for the modification of carbon nanotubes can be grouped into two

principal categories: (a) the covalent attachment of chemical groups through reactions onto the carbon nanotubes walls (b) the non-covalent adsorption of various functional molecules. The first class of CNT modifications, involving strong chemical bonds between tubes and interacting molecules, in its turn, can be roughly divided into two categories: a direct bond of functional groups to the graphitic surface and functionalization of CNTs by strong oxidizing agents to form carboxylic bonds.

Covalent functionalization on the carbon nanotubes backbone

SWNTs have been found to react when treated with molecular fluorine at temperatures between 150 and 600 °C [28]. Other examples include the interactions with anilines, [29] the reactions with nitrenes, carbenes and radicals. Moreover, an efficient method for obtaining covalent modified soluble CNTs was developed by Prato [30]. The most successful approach for the in situ generation of azomethine ylides is based on the decarboxylation of immonium salts derived from condensation of amino acids with aldehydes. The 1,3-dipolar cycloaddition of azomethine ylides was found to be very effective in the functionalization of CNTs. In principle, any moiety could be attached to the tubular network to generate a wide variety of functionalized CNTs.

Chemical functionalization of oxidized CNTs

The covalent functionalization of carbon nanotubes can be obtained by using functional groups grafted on the surface of the carbon nanotubes by acid treatment. The creation of terminal carbons in the shortening and purification process on nanotubes, which upon oxidation are converted to carboxylic acids, are ideal platforms for the functionalization of the carbon nanotubes [31, 32].

Activation of the carboxyl moieties with thionyl chloride and subsequent reaction with amines is one of the most used reaction. Figure 1.4 shows a typical functionalization procedure that, at last, conjugates SWCNTs with an amine. [33]

Amide bond was the first strategy used, by Haddon to achieve soluble nanotubes [29].

By bonding long alkyl amines, CNTs that are insoluble in organic solvents becomes soluble in chloroform, dichloromethane and aromatic solvents. This result was the basis of many further analogous experiments. Water soluble MWCNTs were realized by Sun and co-

workers substituting the terminal alkyl amine with the aminopolymer poly(propionylethylenimine-co-ethylenimine) (PPEI-EI).

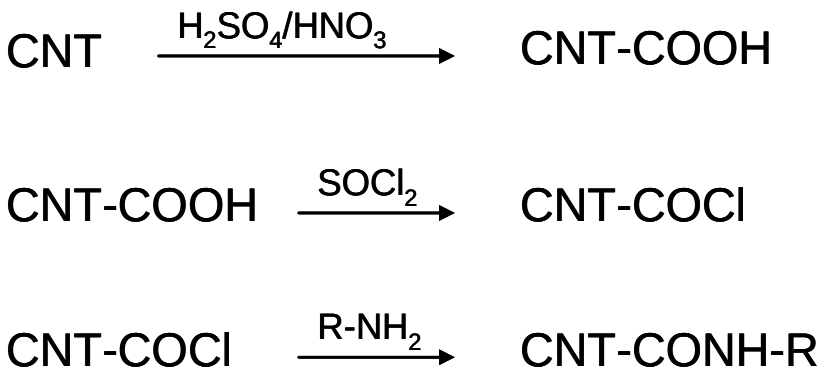

Figure 1.4*. CNT functionalization with primary amine via thionyl chloride acylation.*

Diimide-activated reactions

Concerning bio conjugation between carboxylic and amino groups, the most exploited reaction family involves the carbodiimides molecules. Carbodiimides are used to induce the formation of amide bonds between carboxylic groups and amine. There carbodiimides can be water-soluble and water-insoluble. The water-soluble ones are the most common choice for biochemical reactions. Water-insoluble carbodiimides, instead, are used frequently in peptide synthesis and other conjugations involving molecules soluble only in organic solvents.

As an example 1-ethil-3-(3-dimethylaminopropyl) carbodiimide hydrochloride (EDC) is the most popular carbodiimide for use in biological field. Excess reagent and the by-product of the cross-linking reaction are both water-soluble and may be easily removed by dialysis or gel filtration [34]. Carbon nanotubes, with their –COOH induced groups, are frequently functionalized by means of diimide-activated amidation. It is an alternative and blander method respect to acyl halides functionalization, to bind CNTs to functionalized amine.

Another kind of functionalization between the carboxylic groups of the CNTs and aminic groups was found by Liu and co-workers [26]. In this paper, he presented an amidation reaction mediated by dicyclohexylcarbodiimide (DCC) molecules in ethanol. Using this strategy, he was able to couple carboxylic functional groups of the carbon nanotubes with ammine groups of a short chain thiol forming thiol functionalized carbon nanotubes.

Carbon Nanotubes Arrays

Well-aligned CNT structures are requested for potential CNT applications, such as field emission displays, field emission transistors, superhydrophobic surfaces, chemical sensors, and CNT reinforced. The first examples of aligned CNTs was produced by cutting thin slices of a CNT-polymer composite [35]. Controlled CNT arrays are usually synthesized by growing CNTs on catalyst (e.g. Fe, Ni, Co) pre-patterned substrates in a chemical vapor deposition (CVD) reactor [36] or by self-assembling functionalized CNTs on a substrate [26].
Concerning CVD, iron oxide nanoparticles were used to produce both SWCNTs and MWCNTs arrays. [40]. Even suspended, SWCNT networks were synthesized by contact printing of catalyst onto the tops of silicon pillars [36].
On the other hand, CNT arrays were manipulated with functionalized CNTs using the self-assembling strategy. Oxidized CNTs obtained by acid treatment were self-assembled on silver [37] and Fe coated silicon substrates exploiting the interactions between carboxylic groups of CNTs and substrates surface [38]. Finally, thiol functionalized shortened CNTs were self-assembled on gold substrates [39].

1.2 Introduction to metal clusters

Although nanoparticle research appears to be a quite modern subject, metal clusters were already put into application in antiquity. Noble metals, for example, played an important role in the coloring of glasses and ceramics. One of the most famous examples is the roman Lycurgus Cup, dated between 5th and 4th century B.C. It transmits ruby-red and reflects green light (figure 1.5). Examination with modern equipment revealed gold and silver nanoparticles present in the cup [41]. At that time, of course, the existence of nanoparticles was unknown and it was until 1857 that Faraday found the role of small particles on coloring when he dissolved gold in a colloidal suspension and observed the same deep ruby color.

Figure 1.5*. The Lycurgus Cup (4th Century B.C) is ruby red in transmitted light and green in reflected light, due to the presence of gold colloids.*

1.2.1 Metal cluster electronic structure

Nanoparticles are scientifically interesting nowadays because they represent a kind of transition between atom and bulk solid. The electronic configuration of nanosized particles is known to be different from the bulk state [42]. As electron configuration defines most of the

bulk physical and chemical nature, nanoparticles can be expected to show different behavior respect to the macroscopic systems counterparts. For example, metals exhibit a transition from metal to semiconductor when the size is reduced. A simple model, which takes into account the decrease of the density of states at the Fermi level in small clusters, can be used to explain this behavior. In big clusters or bulk material individual electronic states form band structures typical of metals (figure 1.6). For small particles, the band structure is composed by discrete levels corresponding to a transition to atomic structure due to the spatial confinement of conduction electrons. If the energetic difference between the levels exceeds the values for thermal energies, the cluster shows nonmetallic behavior. The metal-nonmetal transition size can be estimated by the *Kubo criterion*: [43]

$$\delta \approx 2E_f/3N_{aZ} \geq k_B T \qquad (1)$$

where E_f the width of the conduction band, N_{aZ} is the number of cluster atoms and z their valence. For gold (z = 1) the result is: $\delta \approx 8\text{eV}/N_A$. This implies that the semiconductive nature of metal clusters can be observed at room temperature only for very small particles. This model does not take into account changes of the electronic configuration due to the quantization effect but it gives an upper size limit for quantization effects. It also illustrates that metal-to-insulator transitions are an intrinsic feature arising from the decrease of the particle size.

The thermodynamic properties of small particle are known to be different to that of the bulk material. For example, nanoclusters exhibit a lowered melting point respect to the bulk counterparts. [44]

Nanoparticles are interesting for a variety of electronic applications, such as Single-Electron Transistors (SET) [45, 46] and as electronic contacts to molecules [47]. The investigation of optical properties of individual clusters is a very active field [48, 49, 50]. Catalytic activity can also be strongly enhanced using nanosized metals [51].

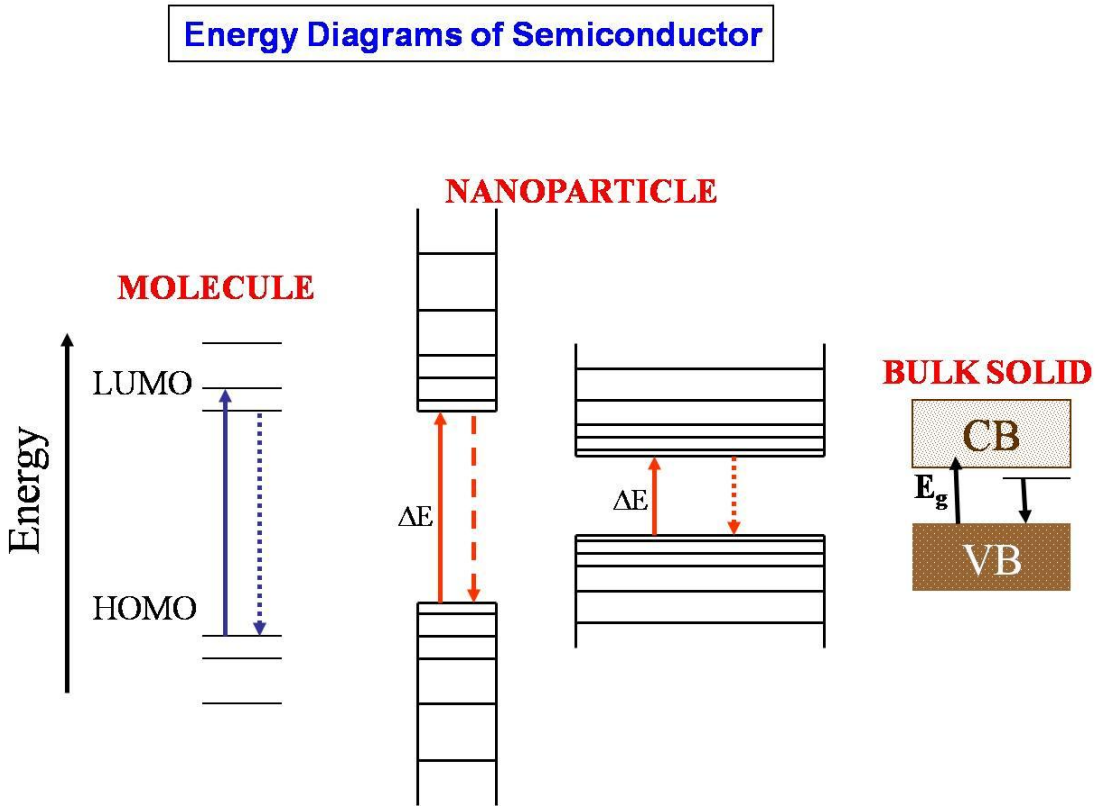

***Figure 1.6**. Representation scheme of the density of states near the Fermi level for single molecules, nanoparticles and bulk solid structure.*

Much effort is put in the examination of such finite-size effects, as they promise to be useful for future application. Different chemical and physical techniques have been developed to grow nanoparticles [52, 53 54]. Contrary to physical methods, wet chemical procedures usually have the advantage of yielding macroscopic amounts of particles. This procedure also allows to synthesize passivated particles surrounded by a shell of organic molecules, preventing particle aggregation. [55, 56]

The particle growth normally leads to a distribution of cluster sizes. Physical methods may provide size-selected particles, but with a much lower yields. The above discussions make it obvious that a detailed knowledge of nanoparticle properties and their dependence on the cluster environment (like passivating molecules) is of primary interest in order to build nanoscale structures.

1.2.2 Optical properties of metal nanoparticles

Theories of Photon-Plasmon Interaction

This paragraph introduces the theories that describe the photon-plasmon interaction. The surface plasmon wavefunction, defined as oscillations of the conduction band electrons in a film, is induced by an interaction between a photon and electrons. The maximum transfer of energy occurs when the surface reflectivity of the metal decreases, an indication of the photon energy transfer to the surface to the formation of plasmon waves. This condition is fulfilled within a certain range of wavelengths. The outcome of this phenomenon is surface plasmon resonance. To describe the excitation of the surface plasmon oscillation, the Mie theory is commonly used.

Exciting Surface Plasmons

The aim is to determine the proper parameters to excite surface plasmons in order to characterize its behavior. To generate a surface plasmon, an evanescent wave is produced. This wave penetrates the metallic surface and induces an oscillation of the electrons at the metal-dielectric surface causing the surface plasmon resonance (SPR).
SPR occurs when the modulus of the wave vector k of the surface plasmon equals the modulus of wave vector k of the incident light. A second equation takes into account the spatial directions of these two vectors:

$$k_{light} = k_{SP}$$

$$n_p \sin(\theta)\frac{2\pi}{\lambda} \approx \frac{2\pi}{\lambda_P}\sqrt{\frac{\varepsilon_{nr}\, n_s^2}{\varepsilon_{nr} + n_s^2}} \qquad (2)$$

where n_P is the refractive index of the prism coupler, ε_{nr} is the real portion of the dielectric constant of the metal, λ is the incident wavelength, λ_P is the wavelength of the surface plasmon, and θ is the angle of incidence.

The refractive index, dielectric constant, and the wavelength of the surface plasmon are constants that depend on the type of sample used; the angle and wavelength of incidence are the variable components that alter the surface plasmon resonance. Since the dielectric constant of a metal is complex, the surface plasmon wave is also complex. In addition, the dielectric function depends heavily on the wavelength of the incident light, influencing the overall surface plasmon resonance.

For metallic particles, the excitation of surface plasmons also depends on the polarizability of that particle. Polarizability is the relative tendency of a charge distribution, like the electron cloud of an atom or molecule, to be distorted from its normal shape by an external electric field. In general, the excitation of a system involves the light scattering. The scattering is a process based on up to two photons which occurs when incident light is transmitted through a system. A portion of the light leaves the system with unchanged frequency (or energy) while the remaining portion is scattered. The intensity and polarization of the scattered light depends on the observation direction. Therefore, the scattered light has characteristics associated not only with the incident source but also with new combinations of frequencies generated from photon interactions.

Mie Theory

In 1908, researcher Gustav Mie developed a theory that mathematically describes the scattering of incident light by spherical particles. The Mie theory is a rigorous solution for the scattering intensity from a spherical, homogeneous and isotropic particle of any diameter *d* in a non-absorbing medium [57]. Mie began his mathematical description by applying spherical coordinates to Maxwell's equations with suitable boundary conditions and parameters such as the particle size, characteristics of the particle material and of the surrounding medium. For such kind of system, the solution describes the multipole oscillations for the extinction cross-section of nanoparticles [58].

Mie also determined that the scalar electromagnetic potentials associated with the particles could be derived from their electric and magnetic fields. Furthermore, his solution related the interaction of electromagnetic incident light and small spheres with the optical properties of bulk material, specifically the frequency-dependence of the material dielectric constant. [58]

Let us consider nanoparticles that are much smaller than the wavelength of the incident light ($r/\lambda \ll 1$). In this case, according to the calculations from Mie, only the dipole oscillations are significant for the extinction cross-section:

$$\sigma_{est}(\omega) = 9\frac{\omega}{c}\varepsilon_m^{1.5} V \frac{\varepsilon_2(\omega)}{[\varepsilon_1(\omega) + 2\varepsilon_m]^2 + \varepsilon_2(\omega)^2} \qquad (3)$$

where V is the spherical volume $(4\pi/3)r^3$, ω is the frequency of the incident light, c is the speed of light, and ε_m and $\varepsilon(\omega)=\varepsilon1(\omega)+i\varepsilon2(\omega)$ are the dielectric constants of the surrounding medium and the material, respectively. Note that resonance is achieved when the conditions $\varepsilon_1(\omega) = -2\varepsilon_m$ and $\varepsilon_2(\omega)$ is independent on the angular frequency are fulfilled. [59]

Equation 3 has been used to determine the absorption spectra of small metallic nanoparticles. The Mie's theory is then able to explain the red color associated with gold nanoparticles in aqueous solution.

Mie's theory assumed low concentration and non-interacting nanoparticles systems. This assumption implies that the electric field generated by a single nanoparticle does not interact with that of other nanoparticles. If the particles distance becomes small, a change in the absorption wavelength occurs in the plasmon resonance and a secondary absorption peak, at longer wavelengths, is observed.

1.2.3 Gold Nanoparticles

Bulk gold is particularly appreciated for its low reactivity toward oxidation. It is infact defined *noble metal*. Although gold is the subject of one of the most ancient themes of investigation in science it is object of an exponentially increasing number of publications, especially in the context of emerging nanoscience and nanotechnology with nanoparticles and self-assembled monolayers (SAMs).

Synthesis

Among the conventional methods of synthesis of AuNPs by reduction of gold (III) derivatives, the most popular one for a long time has been that using citrate reduction of $HAuCl_4$ in water, which was introduced by Turkevitch in 1951 [60]. It leads to AuNPs with diameter of around 20 nm. In 1973 Frens, [61] proposed to vary the ratio between the

reducing/stabilizing agents (the trisodium citrate to gold ratio) to control the AuNPs size (between 10 and 147 nm).

Applications

As already mentioned, one of the properties, which can vary extremely as the size of the particle becomes very small, is its catalytic activity. At nanometer scale, this activity can depend on the geometric and electronic structure of the particle. For supported nanoparticles, the influence of the substrate should be also taken into account. The catalysis of noble metal nanoparticles became especially important at the end of the 1980´s as M. Haruta and co-workers discovered that gold nanoparticles can exhibit a high catalytic activity for reactions such as CO-oxidation, propylene epoxidation and other industrial reactions, specially at low temperature (about 200 K) [62].

Due to the sensitivity of noble metals to light gold nanoparticles have been used as drug carriers for biomedical applications [63]. For example, microcapsules filled with a drug, can be delivered directly to its target location within a cancer cell, avoiding undesired side effects of medications. In order to release the drug, these nanoparticles are introduced into together with a dye in microcapsules. The Au nanoparticles act as strong absorption centers so that a laser pulse leads to a local heating which breaks the capsules with release of their content. Many of these special properties are based on quantum confinement effects at nanometer scale. A simple explanation of this effect relates the material properties with the degree of freedom of electrons which in its turn depends on the nanoparticle size. AuNPs have been used to manipulate the selectivity between solutes in capillary electrophoresis. Therefore, the AuNPs serve as large surface area platforms for organofunctional groups that interact with the capillary surface, the analytes, or both. The apparent mobility of target analytes as well as the electro-osmotic flow could be altered, which leads to enhanced selectivity. [64]

The use of AuNPs has also been extended to chip-based capillary electrophoresis devices, the AuNPs in the microchannels acting as a rectifier. Electromagnetic coupling effects with lithographically produced AuNPs were investigated by photon scanning tunneling microscopy. The surface plasmon propagation on microstructured metal thin films was examined in order to provide an interface between the nano-optical device and classical far-field optics. [65]

The optical manipulation of particles on waveguide surfaces offers a controllable tool for application to particle sorting, sensing, and atomic mirrors. In this context, potassium-ion-

exchanged optical waveguides in glass for evanescent field propulsion of AuNPs were optimized. [66] Encapsulation techniques are currently used to reduce photo-oxidation in commercial devices. In particular, utilization of AuNPs in optoelectronic devices often enhances the optical and electrical properties as well as the stability, this technique effectively inhibits photoluminescence decay. [67]

1.3 Characterization techniques

Characterization and comprehension of material physical and chemical properties are of fundamental importance in order to evaluate their potentiality and to explain their responses during applications. In this thesis, characterization allows controlling CNT properties during production, purification and modification, as well as surfaces of all the carbon nanotubes employed in this work. A wide range of tools allows researchers to study carbon materials and their properties, although each of these techniques reveals only a portion of the full spectrum of characteristics. The following paragraph describes some of the techniques employed to characterize CNT and gold nanoparticles.

1.3.1 Photoelectron spectroscopy

X-ray photoelectron spectroscopy (XPS) is a quantitative spectroscopic technique that measures the elemental composition, empirical formula, chemical state and electronic state of the elements that exist within a material. It is based on the photoelectric effect, explained by A. Einstein in 1905 [68]. X-ray absorption by an atom in solid leads to emission of an electron either from deep core-levels (core lines) or from weakly bonded electrons (valence band). A fraction of these electrons escape into the vacuum system.
The kinetic energy E_K of the photoelectron is related to the energy of the photon $h\nu$ by the following expression:

$$E_K = h\nu - E_B \qquad (4)$$

where E_B is the electron binding energy, h is the Planck constant and υ is the frequency of the radiation. The additional amount of energy that an electron needs to overcome the energy difference between the Fermi energy (Ef) and the vacuum energy (E_{vacuum}) is known as work

function of the sample (Φ_{sample}). Considering this additional energy, the kinetic energy (E_K) that an electron has after leaving the sample, is given by:

$$E_K = h\nu - E_B - \Phi_{sample} \qquad (5)$$

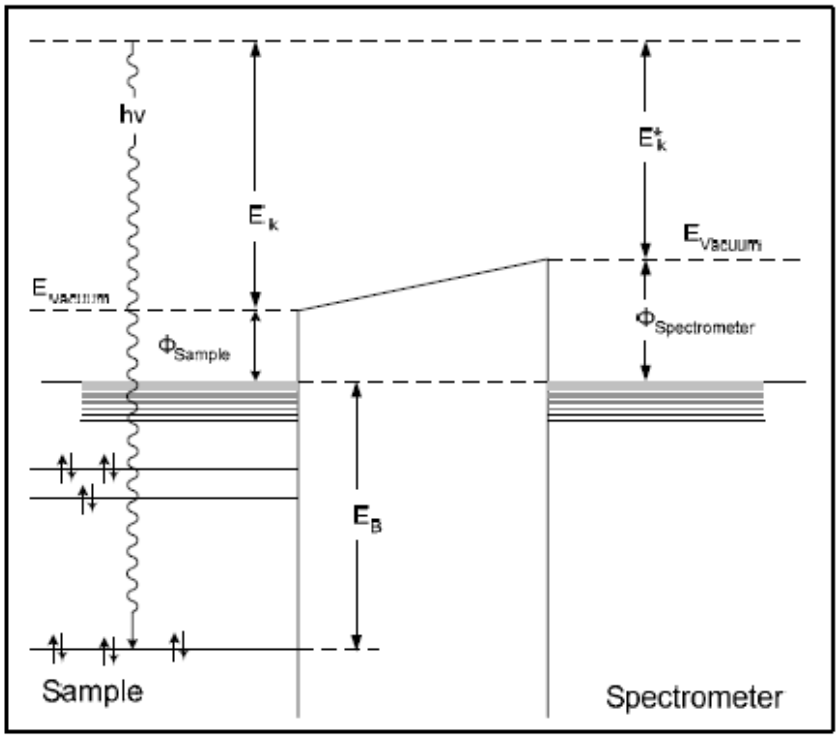

Figure 1.7. *Schematic energy diagram of X-ray photoemission.*

Since the spectrometer possesses its own work function (Φspectrometer), the kinetic energy E_K measured by the spectrometer is given by (see figure 1.7):

$$E_K = h\nu - E_B - \Phi spectrometer \qquad (6)$$

One-electron approximation

The first approximation used to explain the single electron photoemission effect was given by Koopmans [69]. Using this approach, the binding energy of an electron is considered equal to the energy difference between initial state (atom with n electrons) and final state of the atom

(atom with n-1 electrons). Therefore, the binding energy of this electron is equal to the orbital energy ε with the negative sign:

$$E_B = Ef_{inal}(n\text{-}1) - E_{initial}(n)\ E = -\varepsilon \qquad (7)$$

This approximation, does not take into accounts the effects of surrounding electrons due to the positive hole created by the ejected photoelectron. This approximation of the photoemission effect implies that the rearrangement of the surrounding electrons around the atoms is neglected

Initial state effects

Although the core level binding energies of a given element are sufficiently unique to allow the precise identification, they are not fixed values. The electronic configuration is influenced deeply by chemical bonding. The electronegativity and oxidation state of the neighboring atoms can change the electronic configuration, with the appearance of shifts or modifications in the lineshape of the peaks [70].

Information from these shifts provides a quantitative method of chemical analysis. The ability to discriminate atoms with different chemical shifts is limited by the peak widths. Apart the instrumental resolution, the width of the photoemission peaks is determined by the lifetime of the positive core hole created by the photoemission process. Because of the nature of the screening process of the positive hole, the deeper the core hole, the higher are the numbers of de-excitation channels.

Final state effects

The core hole created by the photoemission has a polarizing effect on the surrounding electrons. The electronic response is referred to as relaxation. The system relaxation energy corresponds to the energy difference between the excited electron system that have loose an electron and the relaxation of the system. There are some differences depending on the material. In a bulk metal, the positive charged state created by the photoemission is completely shielded by the conduction electrons and the cores of neighboring atoms. For

isolated metal nanoparticles deposited on poorly conducting substrate [71], the number of conduction electrons and neighboring atoms is limited by the particle size and the positive hole can be screened less efficiently.

Auger Peaks

Figure 1.8 shows the sequence of events following the photoemission. The K level is show as being ionized by an hν radiation. Following the creation of a core hole in the K level, the atom relaxes by filling the hole via a transition from an outer level (L_1). As a results the energy difference becomes available to eject a second electron ($L_{2,3}$**)**. In this Auger process illustrated in figure 1.8, the final state is a doubly ionized atom with core holes in the L_1 and $L_{2,3}$ shells. The energy of the ejected electron in the example of figure 1.8 is:

$$E_{KL1L2,3} = E_K - E_{L1} - E_{L2,3} \qquad (8)$$

In general, the analysis of the Auger peaks can be used to detect elements. It is worth mentioning that Auger peaks always accompany XPS, but they usually rise with broader and more complex structure than photoemission peaks.

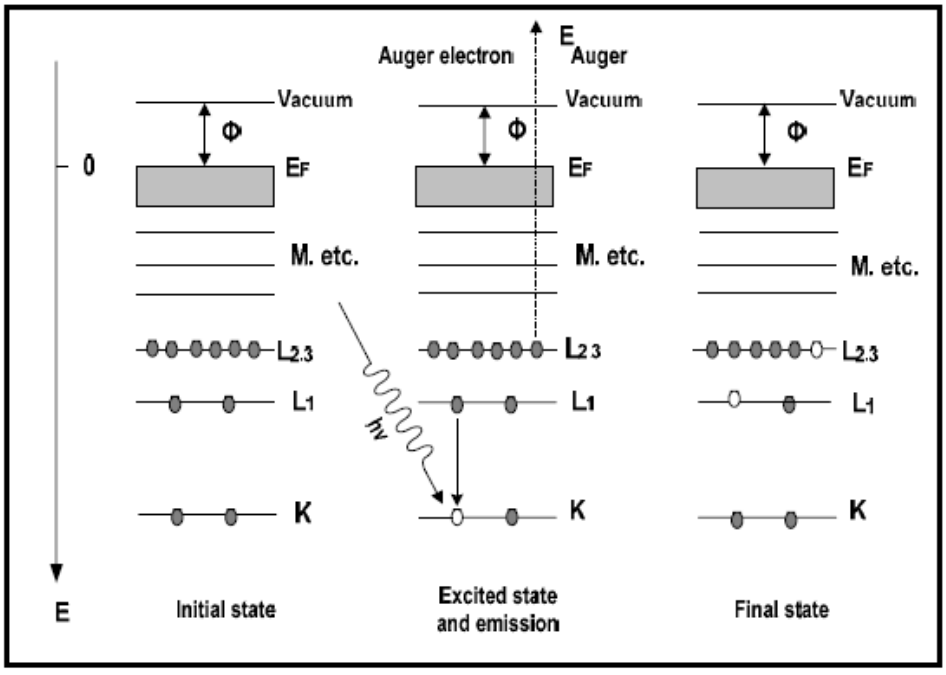

Figure 1.8. *Schematic diagram of the Auger emission in solid.*

Spin-orbit splitting

The total angular momentum of a single isolated electron is obtained by summing the electronic spin S and angular momenta L. For example in a 3d orbital, the total angular momentum J may assume two different values corresponding to J=L+S = 5/2 and J+L-S=3/2. These configurations give rise to two states characterized by different energies which give origin to the spin orbit splitting of the 3d core level. This splitting can be observed in the Ag 3d XPS spectrum. In this case, Ag $3d_{5/2}$ states are at lower binding energy than the state $Ag3d_{3/2}$. For other orbitals like the s orbitals, the angular momentum L = 0. Therefore, for s core level there is not any splitting. These states are called *singlet* in XPS. In contrast, p, d, f orbitals with angular momentum equal to 1, 2, 3, show spin-orbit splitting.

1.3.2 Electron microscopy

In electron microscopy, the electrons interact with the atoms that make up the sample producing signals that contain information about the sample's surface topography, composition and other properties such as electrical conductivity.

The signals result from interactions of the electron beam with atoms at or near the surface of the sample. In the most common or standard detection mode, secondary electron imaging or SEI, the SEM can produce very high-resolution images of a sample surface, revealing details about less than 15 nm in size. Scanning electron microscopy allows to image a rope of SWCNTs in a sample or to view the MWCNTs films [72], (figure 1.9) as well as to characterize surface morphology of other materials. Although the resolution does not allow imaging of individual SWCNT, it can be used, combined with other techniques, to determine the amount of impurities such as amorphous carbon or metal catalyst particles, which typically coexist with CNTs. SEM is also useful for analyzing carbon nanotubes decorated by gold nanoparticles as we see later on.

Although SEM can be useful in imaging the MWCNTs, the transmission electron microscopy (TEM) is much more helpful for structural studies of carbon nanotubes. It allows to determine the number of walls in a MWCNT or to image the isolated SWCNTs residing inside a bundle. In addition, careful measurements of the tube diameters, as well as investigation of structural defects in CNTs are possible. An important benefit that comes with using electron microscopy techniques is the use of energy-dispersive X-ray diffraction (EDX).

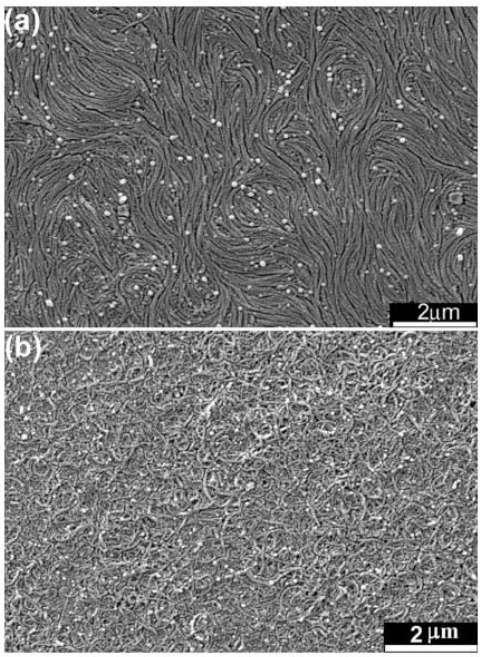

***Figure 1.9**. SEM pictures of CNT films [72].*

Energy dispersive X-ray spectroscopy is an analytical technique used for the elemental analysis or chemical characterization of a sample. As a type of spectroscopy, it relies on the investigation of a sample through interactions between electromagnetic radiation and matter, analyzing x-rays emitted by the matter.

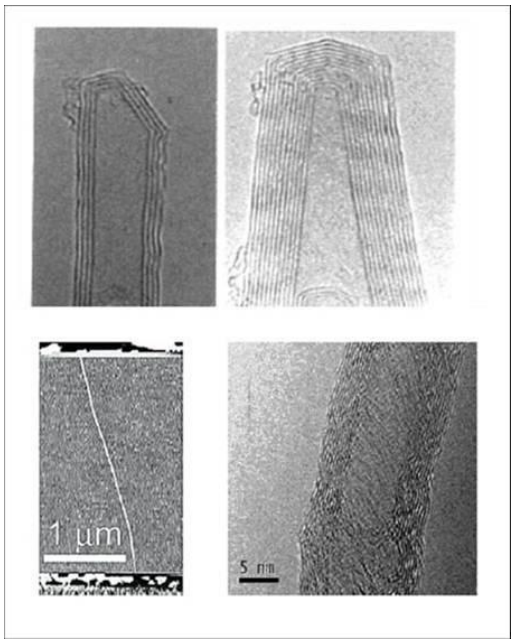

***Figure 1.10.** TEM micrograph showing the layered structure of a MWCNT.*

1.3.3 Atomic force microscopy

Scanning probe microscopies have been exploited to investigate the electrical and mechanical properties of individual nanostructures such as carbon nanotubes.

The atomic force microscopy (AFM) is a very high-resolution type of scanning probe microscopy. In SPM, images are obtained by measuring changes in the magnitude of the interaction between the probe and the specimen surface as the surface is scanned beneath the probe. Hence, the resolution will depend on the sharpness of the probe tip, and the accuracy with which the sample can be positioned relative to the probe.

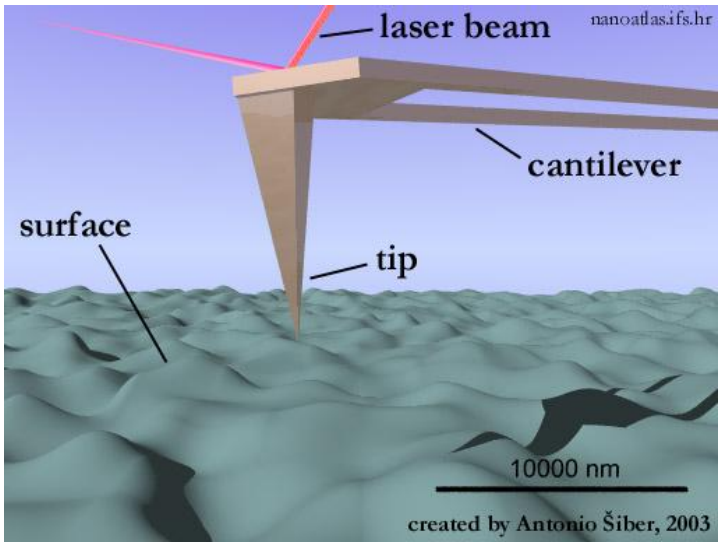

Figure 1.11. *Schematic representation of the atomic force microscope.*

The system is composed by a micro-fabricated, extremely sharp spike mounted on the end of a cantilever. The second fundamental component of an AFM is the scanning mechanism, an accurate positioning system done by means of a piezoelectric transducer. Typically, the deflection is measured using a laser spot reflected from the top surface of the cantilever into an array of photodiodes

1.3.4 Raman spectroscopy

Raman spectroscopy is a spectroscopic technique used to study vibrational, rotational, and other low-frequency modes in a system. Typically, a monochromatic light is employed,

usually from a laser in the visible, near infrared, or near ultraviolet range. For carbon nanotubes, several Raman modes have been identified as disorder-induced modes, such as D mode (1350 cm^{-1}) and D' mode (1620 cm^{-1}). The Raman spectrum (figure 1.12) of carbon structure contains two main bands: The G-mode is the "in-plane" symmetry E_2g mode whereas the D-band (1200–1300 cm^{-1}), attributed to the A_1g (sp3-bonded) stretching mode resulting from the presence of a disordered structure or lattice defects in the graphite structure. The intensity ratio of the G-line (IG) to the D-line (ID) in Raman spectra is a useful parameter to evaluate the quality of carbon materials. A high ID/IG ratio is indicative of the presence of defects inside the carbon layer.

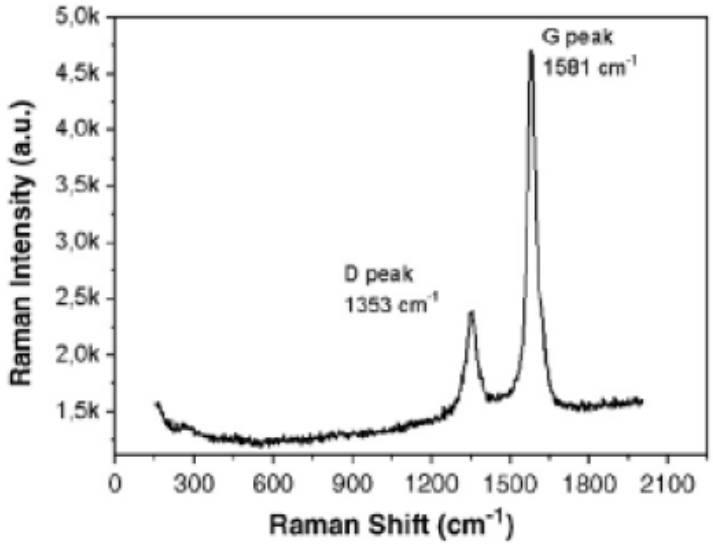

***Figure 1.12**. Typical Raman spectrum of a MWCNT* .[73]

The D* mode is the second-order overtone mode and appears between 2500 and 2900 cm^{-1}.
It is assigned to the first overtone of the D mode and often called D*mode. Moreover, contrary to the D mode, the D* intensity increases with the decreasing of the lattice disorder [73]. Out of all Raman modes observed in the spectra of SWNTs, the radial breathing modes are unique to SWNTs. They appear between 150 cm^{-1} and 300 cm^{-1} from the elastically scattered laser line. It corresponds to the vibration of the carbon atoms in the radial direction, as if the tube is breathing. An important point about these modes is the fact that the energy of these vibrational modes depends on the diameter of the SWNTs.

1.3.5 Fourier transform infrared spectroscopy

Infrared spectroscopy is widely used in both research and industry as a simple and reliable technique for measurement, quality control and dynamic measurement. FTIR can give both qualitative and quantitative information, although it is most important and characteristic use is in the identification of chemical bonds. Adsorptions are typically collected in medium infrared region (4000 – 400 cm^{-1}) where functional groups undergo to a clean dipolar moment change as a consequence of a vibrational or a rotational motion [74]. FTIR application in CNT field is therefore not particularly useful in pristine material characterization, but can provide interesting information about functional groups grafting on the tubes after functionalization processes.

1.3.6 UV-vis spectroscopy

UV-vis spectroscopy has recently been reported as an important tool for characterizing the electronic band structure and quantitatively estimating the purity of bulk SWCNTs [75]. SWCNTs produced with a range of diameters, are mixtures of metallic and semiconducting tubes. The one-dimensional nature of the SWCNTs means that their electronic structure exhibits clear van Hove singularities (VHS). The UV-vis spectroscopy is also useful for the analysis of metal nanoparticles or metal nanoparticles composite both in the solid state and in solutions. The well known Surface Plasmon Resonance (SPR) of small gold nanoparticles falls in the range of the visible and is very sensible to the environment of the nanoparticles and to the interparticle distance as seen previously.

1.3.7 Fluorescence spectroscopy

Fluorescence spectroscopy is used to characterize functionalized CNTs. As we will see the acid treated carbon nanotubes as well as the functionalized carbon nanotubes present luminescence in the visible region. This allows a control of the efficiency of functionalization of the carbon nanotubes.

References

[1] J. Kroto. *Nature* **318** *(*1985) 162.

[2] S. Iijima, T. Ichihashi, *Nature* **354** (1991) 56.

[3] J. Novoselov, *Nature* **306** (2004) 666.

[4]A. K. Geim, K. S. Novoselov, *Nature Mat.* **6** (2007) 183.

[5] T. W. Odom, J.-L. Huang, P. Kim, C. M. Lieber *Nature* **391** (1998) 62.

[6] J. Wildoer, L. C. Venema, A. G. Rinzler, R. E. Smalley, C. Dekker *Nature* **391** (1998) 59.

[7] M. S. Dresselhaus, G. Dresselhaus, A. Jorio, A. G. Souza Filho, M. A. Pimenta, R. Saito. *Acc. Chem. Res.* **35** (2002) 1070.

[8] M. Ouyang, J. L. Huang, C. M. Lieber. *Ann. Rev. Phys. Chem.* **53** (2002) 201.

[9] S. K Doorn, M. J. O'Connell, L. X. Zheng, Y. T. Zhu, S. M. Huang, J. Liu. *Phy. Rev. Lett.* **94** (2005) 127403.

[10] D. A. Stewart, F. Leonard. *Phys. Rev. Lett.* **93** (2004) 107401.

[11] M. J. O'Connel, S. M. Bachilo, C. B. Huffman, V. Moore, M. S. Strano, E. Haroz, K. Rialon, P. J. Boul, W. H. Noon, C. Kittrell, J. Ma, R. H. Hauge, R. B. Weisman, R. E. Smalley, *Science* **297** (2002) 593.

[12] Y. Lefebre, P. Finnie. *Phys. Rev. Lett.* **90** (2003) 217401.

[13] M. M. J. Treacy, T. W. Ebbesen, J. M. Gibson. *Nature* **381**(1996) 678.

[14] M. F.Yu, O. Lourie, M. J. Dyer, K. Moloni, T. F. Kelly R. S. Ruoff. *Science* **287** (2000) 637.

[15] M. Kruger, M. R. Buitelaar, T. Nussbaumer, C. Schonenberger, L. Forro *App. Phys. Lett.* **78** (2001) 1291.

[16] I. Heller, J. Kong, K. A. Williams, C. Dekker and S. G. Lemay *J. Am. Chem. Soc.* **128** (2006) 7353.

[17] S. Masashi, T.Taishi, Y.Atsuo, A. Masafumi, K.Hiromichi *Chem. Phys. Lett.* **358** (2002) 213.

[18] Z.Liu, X. Sun, N. Nakayama-Ratchford, H. Dai, *ACS Nano,* (2007) **1** 50.

[19] T. W. Ebbesen, P. M. Ajayan, *Nature* **358** (1992) 31.

[20] D.Tasis, N. Tagmatarchis, A Bianco,. M. Prato *Chem. Rev*. **106** (2006) 1105.

[21] A. Thess, *Science* **273** (1996) 483.

[22] R.T.K. Baker, P.S. Harris: *Chemistry and Physics of Carbon*, 14, ed. by P.L. Walker Jr. and P.A. Thrower (MarcelDekker, 1978) 83.

[23] K.P. De Jong, J.W. Geus: *Catal. Rev. Sci. Eng*. **42** (2000) 481.

[24] S. Bandow *Appl. Phys. A* **67**(1998) 23.

[25] K.S. Han, H.S. Kim, M.S. Song, M.S. Park, S.S. Han and J.Y. Lee *Appl. Phys. Lett.* **86** (2005) 263105.

[26] J. Liu *Science* **280** (1998) 1253.

[27] D. Pantarotto, *J. Am. Chem. Soc.* **125** (2003) 6160.

[28] E. T. Michelson, *J. Phys. Chem. B* **103** (1999) 4318.

[29] Sun, Y. *J. Am. Chem. Soc.* **123** (2001) 5348.

[30] Maggini, M. *J. Am. Chem. Soc.* **115** (1993) 9798.

[31] J. Chen, *Science* **282** (1998) 61.

[32] M. A. Hamon *Chem. Phys. Lett.* **347** (2001) 8.

[33] Y. Wang, *Chem. Phys. Lett.* **402** (2005) 96.

[34] G. T. Hermanson, *Bioconjugate techniques, Academic press* **1995**.

[35] P. M. Ajayan, O.Stephan, C. Colliex, D. Trauth, *Science* **265** (1994) 1212.

[36] N. R. Franklin, H. J. Dai, *Adv. Mater.* **12** (2000) 890.

[37] B. Wu, J. Zhang, J. Wei, S. M. Cai, Z. F. Liu, *J. Phys. Chem. B.* **105** (2001) 5075.

[38] D. Chattopadhyay, I. Galeska, F. Papadimitrakopoulos *J. Am. Chem. Soc*. **123** (2001) 9451.

[39] Z.F. Liu, Z.Y. Shen, T. Zhu, S.F. Hou, L.Z. Ying, Z.-J.Shi, Z.-N. Gu, *Langmuir* **16** (2000) 3569.

[40] S. S. Xie, B. H. Chang, W. Z. Li, Z. W. Pan, L. F. Sun, J. M. Mao, X. H. Chen, L. X.Qian, W. Y. Zhou, *Adv. Mater.* **11** (1999) 1135.

[41] D. J. Barber, I. C. Freestone, *Archeometry* **32** (1990) 33.

[42] M. Mason, *Phys. Rev. B* **27** (1983) 748.

[43] R. Kubo, A. Kawabata, S. Kobayashi, *Annu. Rev. Mater. Sci*. **14** (1984) 49.

[44] T. P. Martin, Y. Naher, H. Schaber, U. Zimmermann, *J. Chem. Phys*. **100** (1994) 2322.

[45] B. Wang, H. Wang, H. Li, C. Zeng, J. G. Hou, *Phys. Rev. B* **63** (2000) 35403.

[46] K.-H. Park, M. Shin, J. S. Ha, W. Soo Yun, Y.-J. Ko, *Appl. Phys. Lett*. **75** (1999) 139.

[47] A. Shipway, E. Katz, I. Willner, *ChemPhysChem* **1** (2000) 18.

[48] M. Alvarez, J. Khoury, T. Schaff, R. Whetten, *J. Phys. Chem. B* **101** (1997) 3706.

[49] S. Linden, J. Kuhl, H. Giessen, *Phys. Rev. Lett.* **86** (2001) 4688.

[50] G. Lamprecht, G. Schider, R. Lechner, H. Ditlbacher, F. Aussenegg, *Phys. Rev. Lett.* **84** (2000) 4721.

[51] A. Cho, *Science* **299** (2003) 1684.

[52] M.-H. Schaffner, J.-F. Jeanneret, F. Patthey, W.-D. Schneider, *J. Phys. D: Appl. Phys.* **31** (1998) 3177.

[53] X. M. Lin, H. M. Jaeger, C. Sorensen, K. Klabunde, *J. Phys. Chem. B* **105** (2001) 3353.

[54] M. Hostetler, J. Wingate, C.-J. Zhong, R. Murray, *Langmuir* **14** (1998) 17.

[55] M. Brust, C. Kiely, *Coll. Surf. A* **202** (2002) 175.

[56] C. Gutierrez-Wing, P. Santiago, J. Ascencio, A. Camacho, M. Jose-Yamacan, *Appl. Phys. A* **71** (2000) 237.

[57] G. Mie, *Annalen der Physik,* **25** (1908) 377.

[58] S. Link, Mostafa A. El-Sayed, *Int. Rev. Phys. Chem.* **19** (2000) 409.

[59] U. Kreibig, Michael Vollmer, *Optical Properties of Metal Clusters*, Springer Series in Materials Science. Berlin: Springer-Verlag, (1995).

[60] J. Turkevitch, P. Stevenson, C. Hillier, *J. Discuss. Faraday Soc.* **11** (1951) 55.

[61] G. Frens *Nature: Phys. Sci.* **241** (1973) 20.

[62] M. Haruta, *Catal. Tod*. **36** (1997) 153.

[63] R.Gastpar, M. Gehrmann, M. A. Bausero, A. Asea, C. Gross, J.A. Schroeder, G. Multhoff *Cancer Res*. **65** (2005) 5238.

[64] M.Pumera, J.Wang, E.Grushka, R. Polsky, *Anal. Chem.* **73** (2001) 5625.

[65] J. R. Krenn, M.Salerno, N. Felidj, B. Lamprecht, G. Schider, A. Leitner, F. R. Aussenegg, J. C.Weeber, A. Dereux, J. P. Goudonnet *J. Microsc.* **202** (2001) 122.

[66] L. N. Ng, B. J.Luff, M. N. Zervas, J. S. Wilkinson, *Opt. Comm.* **208** (2002) 117.

[67] J. H. Park, Y. T. Lim, O. O. Park, Y. C. Kim, *Macromol. Rapid Comm.* **24** (2003) 331.

[68] A. Einstein, *Annalen der Physik* **7** (1905) 132.

[69] T. Koopmans, *Physica* **1** (1933) 104.

[70] D. C. Lim, I. L.-Salido and Y. D. Kim, *Surf. Sci*. **600** (2006) 507.

[71] P. S. Bagus, C. R. Brundle, G. Pacchioni, F.Parmegiani, *Surf. Sci. Rep.* **19** (1993) 265.

[72] C,Du, J. Yeh, N. Pan *J. Mater. Chem.* **15** (2005) 548.

[73] T. C. Chieu, *Phys. Rev. B* **26** (1982) 5867.

[74] D. A. Skoog, J. J. Leary, *Chimica analitica strumentale, Edises* (1995).

[75] M.E. Itkis, *Nan. Lett*. **3** (2003) 309.

CHAPTER 2

2.1 Experimental Section

In this paragraph CNT functionalization procedures as well as the instrumentation used in this Thesis are described.

2.1.1 Materials

Multi-walled carbon nanotubes: (MWCNTs) (Nanoamor USA) Purity: > 95%, outside diameter: 10-20 nm, inside diameter: 5-10 nm, length: 0.5-2 μm, SSA: ~ 200 m^2/g, bulk density: ~0.17 g/cm^3, true density: ~2.1 g/cm^3.

Cysteamine: (Sigma-Aldrich USA) Linear Formula: $NH_2CH_2CH_2SH$ Molecular Weight: 77.15 (purity 98%).

N,N′-Dicyclohexylcarbodiimide: (SigmaUSA**)** Acronymus: DCC, Formula: $C_6H_{11}N=C=NC_6H_{11}$ Molecula ar Weight: 206.

Gold colloids: (Aldrich) Au Molecular Weight:196.97 Au nanoparticles contaminations <0.01% tannic acid <0.04% sodium citrate 0.02% sodium azide as preservativeconcentration ~0.01% $HAuCl_4$ ~1, mean particle size 10 nm, particle size distribution 8.5-12.0 nm.

Tetrachloroauric acid: (Aldrich), Linear Formula: $HAuCl_4$, Molecular Weight: 339.79 (anhydrous basis) 99.99% trace metals, degree of hydration, ~3, density 3.9 g/mL at 25 °C.

Other chemicals and solvents used

REAGENT	FORMULA	COMPANY
Acetone	CH_3COCH_3	Sigma-Aldrich
Dimethylformamide	C_3H_7NO	Sigma-Aldrich
Chloroform	$CHCl_3$	Carlo Erba
Dicloromethane	CH_2Cl_2	Carlo Erba
Dietilether	$CH_3CH_2OCH_2CH_3$	Sigma-Aldrich
n-Exane	C_6H_{14}	Carlo Erba
Etanol absolute	C_2H_5OH	Carlo Erba
Sodium Hydroxide	NaOH	Carlo Erba
Toluene	$C_6H_5CH_3$	Carlo Erba
Cytric Acid	$C_6H_8O_7$	Carlo Erba
Nitric Acid	HNO_3	Baker
Sulphuric Acid	H_2SO_4	Fluka
Chlorhydric Acid	HCl	Carlo Erba

2.1.2 Methods

CHAPTER 3

Carbon nanotubes oxidation

About 0.20 g of CNTs were soaked with 30 ml of a mixture of H_2SO_4 (Fluka, 95-97%) and HNO_3 (Baker, 69-70%) in a 3:1 ratio. The flask was connected to a bulb condenser and heated with an oil bath at 40 °C under magnetic stirring and sonification. Reaction times varied between 6 and 12 hour. The reaction mixture was then diluted with water (9 times in volume) and let overnight for precipitation. The supernatant was decanted, and the suspension was diluted with deionized water and filtered with a 1 μm filter membrane under vacuum. The shortened MWCNTs were washed on the filter with deionized water until the filtrate pH became neutral. The solid phases obtained was successfully washed with diluted NaOH

(Carlo Erba) water solution, then washed again with deionized water. The precipitate was collected from the filter (yield = 58%) and dried overnight in an oven at 50 °C.

Synthesis of thiol functionalized carbon nanotubes

The carboxyl-terminated nanotubes were thiol-functionalized by reacting with $NH_2(CH_2)_2SH$ (*Aldrich USA*) in ethanol suspension with the aid of DCC (dicyclohexylcarbodiimide, *Aldrich, USA*) condensation agent. In a typical procedure, functionalized carbon nanotubes were spread in ethanol 30 mg in 50ml and sonicated for 10 minutes. An excess (referred to the calculated amounts of carboxylic groups present on the CNT) of dicyclohexylcarbodiimide (0.26 g) was added and the relative solution was stirred for some minutes. Finally a 50mM solution of $NH_2(CH_2)_2SH$ (10 ml) was added and the solution was stirred again for 24 h at room temperature. The amount of $NH_2(CH_2)_2SH$ was chosen to be the double of the estimated carboxylic groups concentration. The thiol functionalized carbon nanotubes obtained are quite unstable and tend to precipitate slowly after the reaction. The precipitate obtained 24 hours after the reaction stop was separated by the solution by filtration, washed to remove the unreacted molecules and the by-products, then dispersed in ethanol by prolonged sonication (30 minutes).

Synthesis of carbon nanotubes/gold nanoparticles hybrids

The carbon nanotubes-gold nanoparticles composites are produced by dissolving a certain amount of thiol functionalized CNTs (0.3mg/ml) in ethanol with successive addiction of an excess of gold nanoparticles (5ml of concentred solution)) to ensure the binding of the Au NP to the carbon nanotubes. The solution was stirred for ten minutes and allowed to stand overnight. The CNTs were separated by filtration, washed and resuspended in ethanol.

Adsorption of thiol functionalized carbon nanotubes on gold substrate

Thin gold films (25nm) were deposited by thermal evaporation on 2.5 nm chromium covered Si/SiO_2 substrate. The gold plates were immersed in the thiol functionalized carbon nanotubes suspension (CNT-S) for 2 and 4 hours and cleaned by sonication in ethanol for 1 minute.

CHAPTER 4

Adsorption of cysteamine on platinum and gold substrate

The gold and platinum plates were immersed in the 50mM solution of $NH_2(CH_2)_2SH$ for 2 hours followed by sonification in ethanol for 3 minutes.

Deposition of the CNT films by the external electric field

The cysteamine-modified gold and platinum substrate were mounted in a planar geometry electrodes with a gold counter electrode. The distance between the two electrodes was fixed to 1 mm with a non-conductive spacer. The system was immersed in a 5 ml carbon nanotubes solution prepared mixing 4 ml of 3mg/ml of oxidized carbon nanotubes suspension with 1 ml of 2.5 mM dicyclohexylcarbodiimide solution.
A positive potential was applied to the cysteamine modified gold substrate, while a negative potential was applied to the counter electrode. 10V of potential vas applied to the system for 5 and 20 minutes. After the deposition the system was washed with ethanol and dried with nitrogen stream.

Adsorption of preformed gold nanoparticles on a Pt/CNT surface

The Pt/CNT samples were immersed in a 5 mM, cysteamine ethanolic solution for 12 h at ambient temperature. The sample were then rinsed with ethanol and dried with nitrogen stream. The sample was immersed into a concentrate gold nanoparticles solution for 4h then washed with water and ethanol and dried with nitrogen steam.

Synthesis of cysteamine functionalized gold nanoparticles

In a typical procedure 5ml of concentred gold nanoparticles solution were added to 1 ml of 5mM cysteamine solution in ethanol. The thiol functionalized gold nanoparticles obtained are quite unstable and tend to precipitate slowly after the reaction. The precipitate obtained 24 hours after the reaction stop was separated by the solution by filtration, washed to remove the unreacted molecules, then dispersed in dimethylformamide.

Adsorption of preformed cysteamine functionalized gold nanoparticles on a Pt/CNT surface

The Pt/CNT samples were immersed in the cysteamine functionalized gold nanoparticles solution for 12 h. The sample were then rinsed with ethanol and dried with nitrogen stream.

CHAPTER 5

Synthesis of the CNTS/Au sample

In a typical procedure one drop (sample CNTS/Au1) or 5 drops (sample CNTS7Au2) of concentred gold nanoparticles water solution was added to the 5 ml of 0.3 mg/ml thiol functionalized carbon nanotubes suspension followed by 5 min of stirring. The functionalized carbon nanotubes-gold nanoparticles composite (CNTS-Au) show low stability in the ethanolic solution and tend to completely precipitate after 24 hours.

CHAPTER 6

Synthesis of the a:C/Au films

a-C:Au nanocomposite films are deposited on silicon wafers by magnetron sputtering in Ar. The magnetron power is about 140 W. Silicon wafers are mounted on a substrate holder that rotates at a speed of 3.14 rpm. During deposition, the substrate temperature is maintained at 20–50 °C, while the working gas pressure in the vacuum chamber is 10^{-3} Torr. The target is graphite covered by Au plates. Depending on the target Au-to-graphite surface ratio, C films with different Au concentrations are obtained.

The growth rate is about 2 nm/min. Films with thickness of about 40 nm are deposited for X-ray photoelectron spectroscopy (XPS) measurements, whereas films with thickness 200 nm are produced for XRD measurements.

The Au concentration, as revealed by XPS, ranges from 8 to 38 at.%, depending on the Au-to graphite surface ratio at the target.

CHAPTER 7

Synthesis of gold nanoclusters on thiol functionalized carbon nanotubes film

Some drops of 0.3mg/ml suspension of thiol functionalized carbon nanotubes in ethanol were spreads on platinum substrates forming a black uniform film and then dried under pure nitrogen. The sample was dipped in a 1mM $HAuCl_4$ water solution for 4 hours. The samples were then irradiated with UV light in air using a Deuterium-UV lamp, 25W with λ_{irr} down to 160 nm for 1 minutes (CNTAu1) and 5 minutes (CNTAu5).

2.1.3 Description of the instruments used

X ray photoelectron spectroscopy

In this section the setup of the ESCA instrument used for this work will be presented. The ESCA200 was purchased from SCIENTA – Uppsala SW (see figure 2.1). Samples are introduced through the load-lock chamber and can be transferred via sample linear transfer stage, to measurement chamber.

The most important part in this instrument is the hemispherical analyzer (HMA). Combined with electrostatic lenses (located in the vertical stage) it is used for counting electrons as a function of their kinetic energy. An X-ray tube with a monochromator is attached to the chamber, allowing measurements with $h\nu$ =1486.6 eV (Al Kα). An electron flood gun ($E_{kin,max}$ < 10eV) are available to irradiate the sample for charge compensation. The HMA (figure 2.2) consists of two concentric hemispheres, an entry and an exit slit to allow the measurement of the electron kinetic energy. Finally a multichannel plate placed after the exit slit is used to detect the electron current. The ESCA 200 has the peculiarity to work in two different modes. In *transmission mode* the signal intensity and the energy resolution are optimized. In the *spatial mode* the set of electrostatic lenses are able to maintain the electron trajectories separated. This allows the acquisition of spectral maps of describing the sample composition. High voltages are applied to the hemispheres, allowing only electrons with a

chosen kinetic energy (the *pass energy*) to successfully reach the detection device and be counted. The analyzer can be driven in two different modes: constant analyzer energy (CAE) and constant retardation ratio (CRR). In CAE mode of operation the pass energy *Ep* is set to a fixed value (usually between 150 and 500 eV). This leads to a constant energy resolution ΔE, which is only a function of the selected slit width.

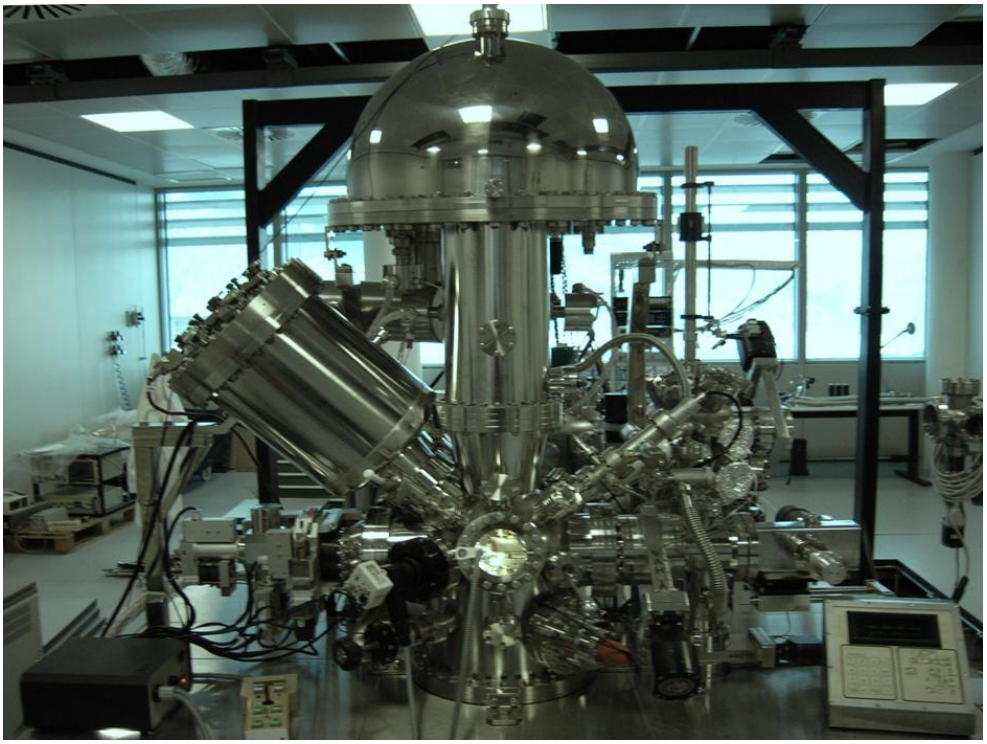

Figure 2.1. *ESCA 200 instruments used in our laboratory.*

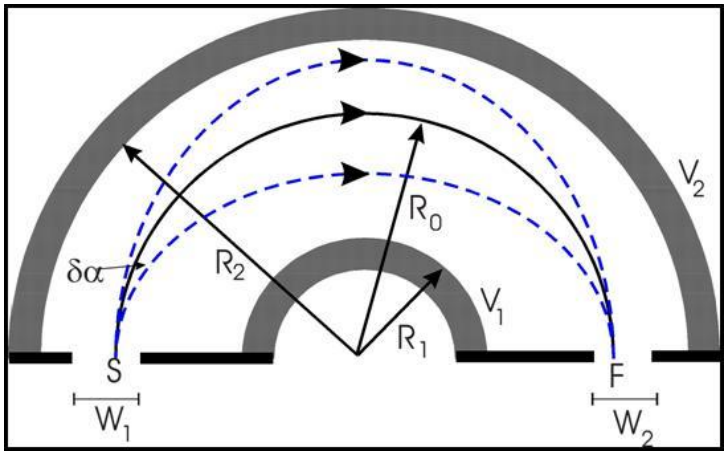

Figure 2.2*. Hemispherical Mirror Analyzer: the transfer lens system casts an image of the detection area on the sample in front of the analyzer aperture.*

This mode is used for XPS measurements, as a constant resolution over the whole kinetic energy range (typically 1200eV to 0 eV) is crucial for reliable evaluation of the spectra.
Monochromatisation of X-ray radiation dramatically decreases the line width in the energetic spectrum allowing only a small fraction of the total light to reach the sample. This strongly enhances the resolution of photoelectron spectra and eliminates satellite peaks stemming from the electronic substructure of the anode involved in the X-ray emission process. Monochromatisation is achieved by performing a Bragg diffraction using 7 quartz crystals. In agreement with the *Bragg's Law*: $n\lambda = 2d \sin\theta$, the λ selection is mate choosing the proper is the Bragg angle θ for the given crystal plane spacing *d*, *n* represents the order of reflection and λ the X-ray wavelength. To reach high photon intensities the 7 quartz crystals are bent to obtain an X-ray focusing (small spot XPS) on the sample. The bent crystal surface are placed on a circumference of a large circle, called *Rowland circle,* on which sample and anode have to be positioned to satisfy the Bragg Law. The radius of the Rowland circle is half the curvature radius of the crystal. (figure 2.3)

.

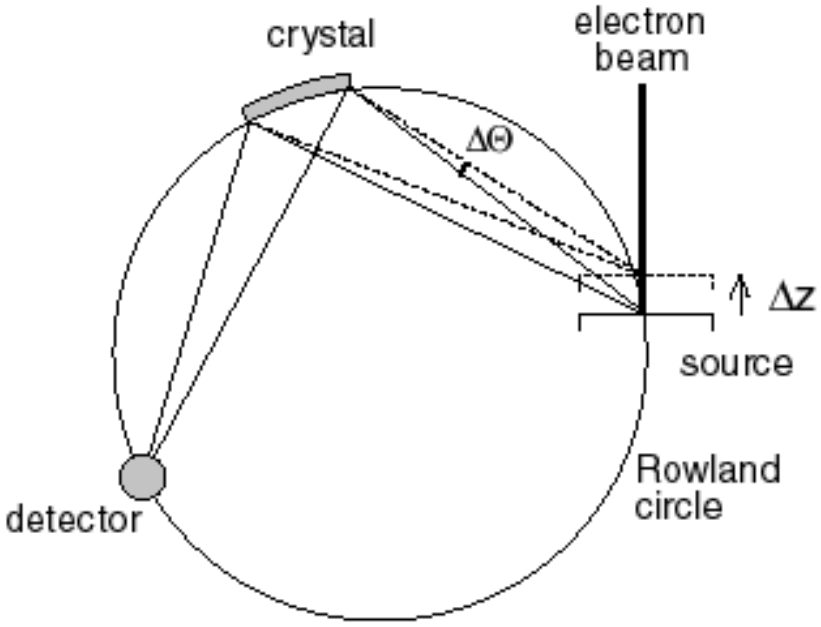

Figure 2.3*. Rowland circle: the anode X-ray spot and the sample suface have to be on the Rowland circle to assure proper monochromatization (correct Bragg angle) and focus.*

Scanning electron microscopy

Scanning Electron Microscopy Analysis was carried out in a JSM-7001F instrument equipped with a thermal field emission gun. Images were acquired with sample placed at 45° and 90° normal to the analyser direction.

Transmission electron microscopy

TEM observations were made with a Philips 400T microscope operated at 120 keV and equipped with an energy dispersive X-ray spectroscopy (EDXS) system. The CNT suspension was spread onto a copper grid covered with an amorphous carbon film.

Scanning probe microscopy

Atomic Force Microscopy (AFM) Measurements were acquired with a NT-MDT Solver Pro in semi contact mode, using conical shape tips (angle < 22 deg., typical curvature 10 nm, typical elastic constant 5.5 N/m).

Raman Spectroscopy

Raman scattering experiments were done using a standard experimental set-up Join Yvonne U1000 in a wide range of frequency (from −300 to 5000 cm^{-1}) with an excitation wavelength of 633nm.

Uv-Vis absorption spectroscopy

Visible Absorption measurements were performed using a Cary 5000 UV-Vis-NIR spectrophotometer in dual beam mode.

FTIR spectroscopy

Fourier-Transform Infra Red Spectroscopy (FTIR) measurements were performed on diluted ethanolic suspension of carbon nanotubes in a Biorad FTS 185 FTIR spectrometer equipped with DTGS detector.

X ray-diffraction

XRD pattern are obtained with an APD 2000 X-Ray Diffractometer with Cu Kα radiation source operated at 40 keV with 2-Theta step of 0.05° and acquisition time of 5 sec. XRD results were analyzed by modelling an analytical profile shape function. Pearson VII function was used for profile fitting after proper background subtraction and Rachinger alpha-2 correction. The distance between two peaks, assigned to the (111) and (200) reflections, was kept at $2\theta = 6.2^{o}$ as for bulk gold, stabilizing the fit. The instrumental dependent broadening was removed by Stokes deconvolution. The size distribution was calculated by Fourier analysis following the Warren–Averbach method. For spherical particles of diameter D, the size in the direction normal to the sample surface should be taken as the averaged height of the sphere, 2D/3. The Fourier coefficients are plotted versus the domain size. The second derivative of Fourier coefficients with the domain size gives the size distribution.

Photoluminescence spectroscopy

Photoluminescence (PL) measurements in the 500-800 nm region were obtained upon excitation wavelength of 531.5 nm. Great care was taken in these experiments to keep unmodified the experimental conditions when measuring the PL intensity from the nanotubes solution and from the corresponding reference one, in order to make it possible to quantitatively compare the PL intensities. Photo images are obtained in a dark room using a 530nm, 5mW green pointer and a Sapphire filter, which is placed in front of the camera lens.

CHAPTER 3

3.1 Functionalization of carbon nanotubes

3.1.1 Introduction

Since their discovery in 1991 by Iijima [1] carbon nanotubes (CNTs) are extensively studied because of their potential application in a large field of uses like emitter devices [2], nanoelectronics [3], chemical probes, [4] energy storage [5] and sensing [6,7,8]. However, the intrinsically difficult manipulation of CNTs causes serious difficulties to potential applications. In particular, from a chemical point of view, unmodified CNT is of scarce practical interest because of the lack of specific functionality.

Bio-sensors, for example require chemical attachment of biomolecules (proteins, DNA etc.) on the nanotubes [9]. In this respect unmodified CNTs cannot be directly used because of the lack of specific binding sites. For bio-sensing applications functional groups must be inserted into the CNTs in order to detect specific molecules. From the structural point of view, well controlled alignment of the CNTs on a substrate is required. Traditional methods to obtain vertical alignment of CNTs as catalytic CVD [10] suffer from some problems, like the need of sophisticated equipment. Finally these CNT forests show weak stability in presence of solvents with the tendency to collapse. Self-assembling is an alternative route to form vertically oriented CNTs arrays, which could also take advantage from the fast and easy manipulation of the functionalized nanotubes. Despite the very poor reactivity of the CNT, in fact, chemical functionality can be easily grafted in order to achieve better manipulation properties. A lot of paper in literature show different chemical pathways with the aim to obtain CNTs with different functional group for various applications [11-13]. In this respect the work of Liu et al [11] is a good example of surface engineering to obtain high density vertically aligned CNTs on gold using thiol functional groups. The advantage of this method is linked to the great chemical affinity between gold and thiol and the good stability of the Au-S bond. Recently other functionalization techniques have been successfully tested like metal assisted chelation [14] and layer-by-layer polyelectrolyte complexing [15]. The starting point of all these methods is the formation of carboxylic groups on the surface of the carbon nanotubes. These acid groups are usually introduced by oxidation using strong acids, and they occur predominantly at the more reactive (open) ends or at defect sites of single and multi-

walled carbon nanotubes. Exploiting the high chemical reactivity of these functional groups it is possible to covalently attach chemical species, biomolecules or metal nanoparticles obtaining a stable functional surface that could be particularly attractive for sensing applications. In this chapter we present a synthesis of vertical aligned CNTs on a gold substrate via the condensation reaction. The aim is to obtain a functional surface. The functionalization procedures were tested point by point by means of X-ray photoelectron spectroscopy, Scanning Electron Microscopy, Infrared Spectroscopy and Visible Absorption Spectroscopy.

3.1.2 Result and discussion

Oxidation of carbon nanotubes

In Figure 3.1 the reaction scheme for the production of the thiol functionalized Multi-Walled Carbon Nanotubes (CNT-S) and their assembling on a gold substrate is presented. The first step regards the cut and functionalization of MWCNTs accomplished by a HNO_3/H_2SO_4 mixture under ultrasonication. The effectiveness of this procedure was already tested by work presented in literature [11].

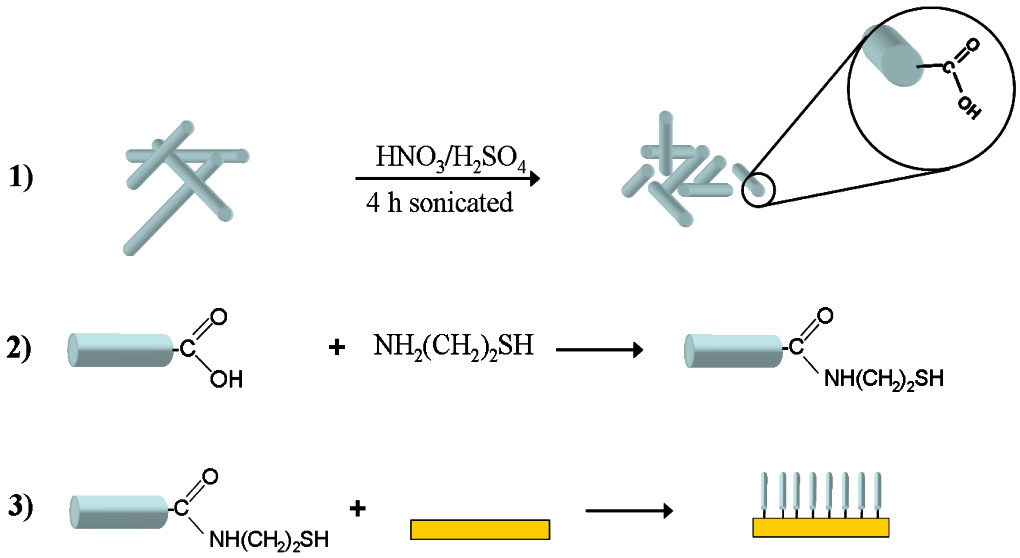

Figure 3.1. *Scheme of the functionalization processes and reactions 1) cutting of the MWCNT 2) condensation reaction between the thiol and the carbon nanotubes. 3) Self-assembling of the CNT on the gold plate.*

A Raman spectrum collected at excitation wavelength of 633 nm for the acid-treated carbon nanotubes is reported in figure 3.2. In the range between 1100 and 1800 cm^{-1}, spectrum exhibits several prominent resonances including D mode (1302– 1360 cm^{-1}), G mode (1469–1580 cm^{-1}), D' mode (1600–1614 cm^{-1}). The G-band represents the "in-plane" symmetry allowed E_2g mode whereas the D and D' bands are due to the first-order double resonance Raman scattering process and reflect the presence of structural disorder on the graphite plane of the nanotubes. In particular, the D and D' modes are related to the "inter-valley" and "intravalley" scatterings around the K point, respectively [16]. Structural defects induced by acid treatment can be clearly observed by the changes of vibrational response of altered graphitic morphology of the MWCNTs.

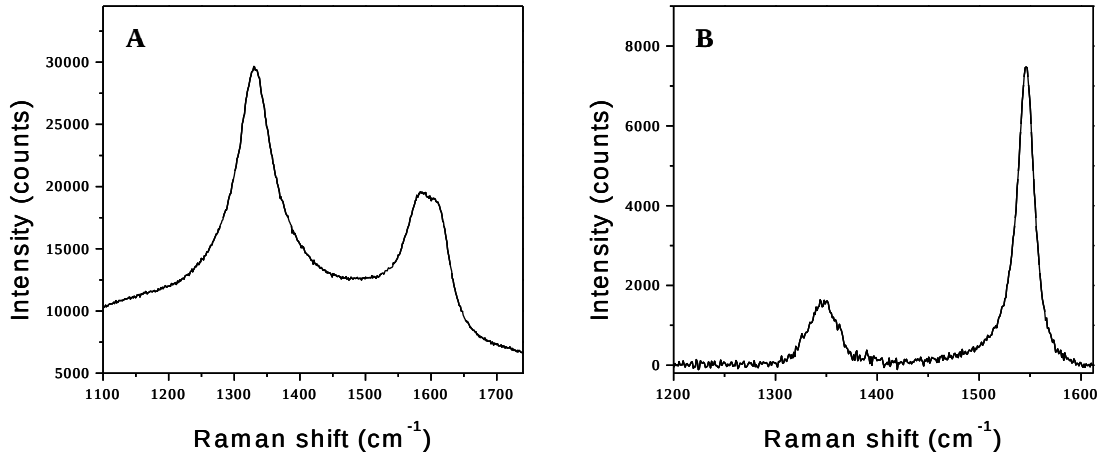

Figure 3.2 (A). *Snapshot of the D, D' and G bands region for acid treated carbon nanotubes (CNT-COOH)* ***(B):*** *snapshot of the D and G bands region for pristine carbon nanotubes (CNTs).*

For instance, the D mode is significantly enhanced as compared to the pristine carbon nanotubes. As shown in figure 3.2A and 3.2B acid-treated MWCNT samples intensity ratio (D/G) increased from 0.14 for the pristine MWCNTs to 1.62 for acid treated CNTs. The position of the D mode does not shift significantly (2–10 cm^{-1}) upon acid treatment. The spectral modifications can be attributed to the changes in the density of states (DOS), induced by the formation of defects, which resulted from acid treatment. Crepsi et al. have demonstrated by calculation that the introduction of bond rotation defects (the so-called Stone–Wales defects) can close the gap in large-gap carbon nanotubes, open the gap in small-gap carbon nanotubes and increase (DOS) at the Fermi level for the metallic carbon nanotubes

[17]. The presence of defect in high concentration is also confirmed by transmission electron microscopy analysis. Figure 3.3 shows a high resolution image of the acid treated carbon nanotubes. The dark spots present in the images are due to defects present in the crystalline structure of CNT that change the electron beam direction.

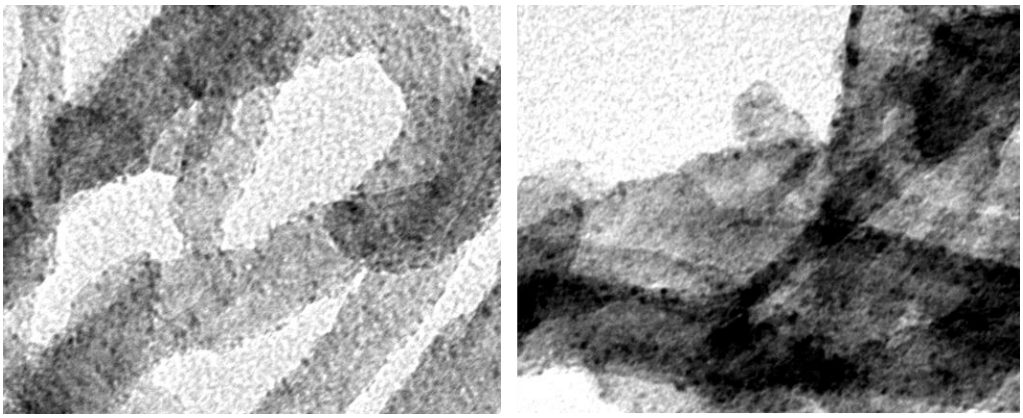

Figure 3.3: *Transmission electron microscopy of acid treated carbon nanotubes (CNT-COOH)*

The XPS survey spectra of the pristine commercial carbon nanotubes and acid-treated carbon nanotubes are reported in figure 3.4 as well as the identification of the C1s and O1s core lines. The oxygen atomic abundance in the pristine nanotubes is around 2%, probably due to contamination. After the acid treatment the total abundance of oxygen is 18.25% clearly indicating a strong oxidation of the carbon nanotubes.

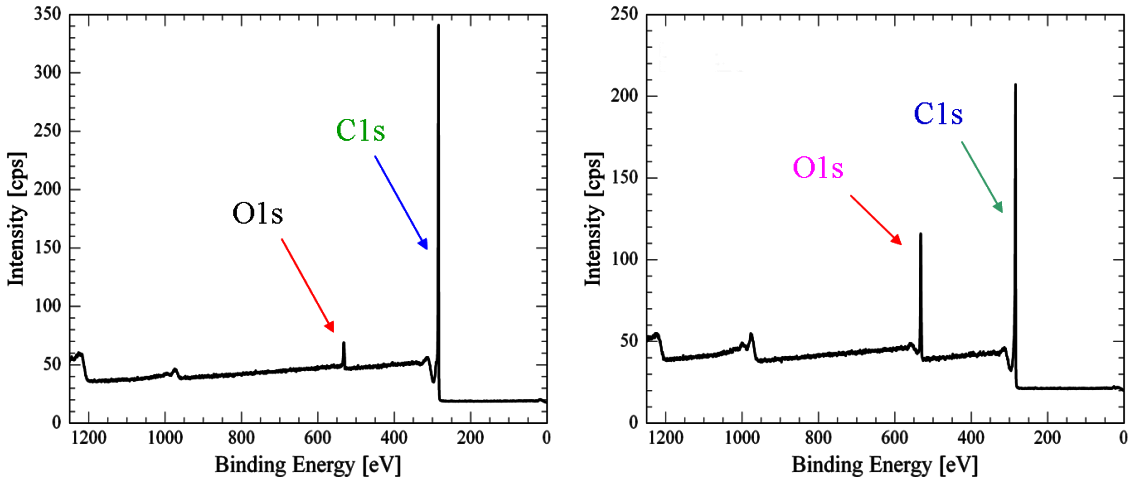

Figure 3.4. *Survey spectrum of pristine commercial carbon nanotubes (left) and acid-treated carbon nanotubes (right).*

The sonication treatment causes the formation of high temperature microscopic areas [18] leading to localized sonochemistry that attack the surface of the CNTs, creating an open hole on the CNT side. The hole is continuously etched by the acid mixture leading to the formation of C-O bonds (especially carboxylic and oxydrilic groups) until the nanotubes are cut. This chemical process produces shorter nanotubes terminated with carboxylic and oxydrilic groups. The resulting solid-shorted carbon nanotubes show high solubility in a plenty of solvents like water, ethanol, isopropyl alcohol etc. The suspension is stable in ethanol for some month without the need of successive sonication. This stability is another clear evidence of the presence of a great number of carboxylic groups on the carbon nanotubes. At neutral pH the acid-treated CNTs in ethanol are known to be negatively charged with a ξ-potential of around -12 mV.[19] The presence of these anionic groups on the surface stabilize the CNTs suspension through electrostatic repulsion.

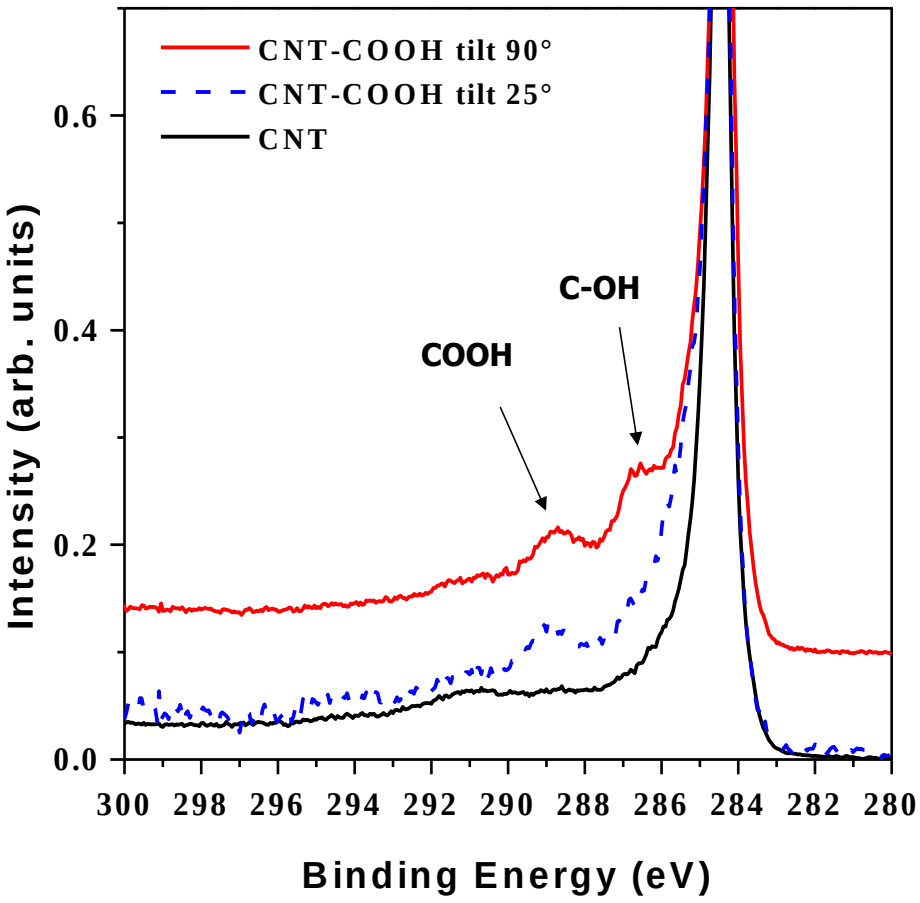

Figure 3.5. *C1s core line of pristine (CNT) and acid treated (CNT-COOH) carbon nanotubes at tilt =90 and 25°.*

The acquisition of high resolution XPS spectra enables a detailed analysis of the kind of bonds formed during the acid attack. An example is shown in figure 3.5 and 3.6. The C1s core-line of the pristine carbon nanotubes (CNTs) shows the main peak position at 284.4 eV with the typical asymmetry of the peak due to the plasmon losses similar to those of graphite. [20]. The acid treated carbon nanotubes (CNT-COOH) show the same feature at 284.4 eV but also a component at around 286 eV (assigned to C-OH bond) and a peak at 288.5 assigned to the carboxylic groups [21]. The O1s core lines analysis is fitted with three components, the peak at 532 eV is assigned to single C-O bonds, while the components 1 and 3 refer to the two different oxygen species of carboxylic group. The atomic abundance of COOH group respect to the total amount of carbon is C_{COOH}/ C_{Tot}= 9.89 at. %. The total amount of oxidized carbon (carboxylic + oxydrilic) is 15.11 at. % (see figure 3.6 and table 3.1).

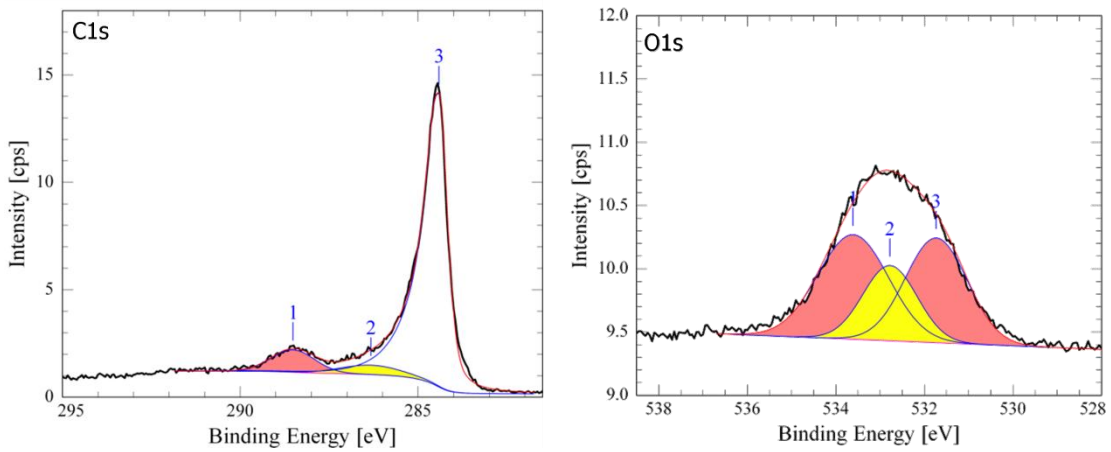

Figure 3.6*. C1s core line (left) and O1s (right) fitting of the acid treated carbon nanotubes tilt= 90°.*

Lines	BE	Conc.	Bonds
C1s1	288.45	7.6 %	-(C=O)-OH
C1s2	286.46	4.7 %	-C-OH
C1s3	284.40	69.5 %	-C-C
O1s1	533.65	7.3 %	-(C=O)-O*H
O1s2	532.78	4.50 %	-C-O*-H
O1s3	531.71	6.40 %	-(C=O*)-OH

Table 3.1. *Quantitative analysis obtained from the C1s and O1s core lines for acid treated carbon nanotubes.*

The high concentration of oxidized carbon readily explains the high solubility and stability of the CNT-COOH suspension in polar protic solvents. The survey spectrum of the pristine CNTs shows that no other elements are present demonstrating the high purity of the CNTs.
The C1s and O1s core line fitting and the table with the quantitative analysis for the same samples acquired at 25° tilt are presented in figure 3.7 and table 3.2.

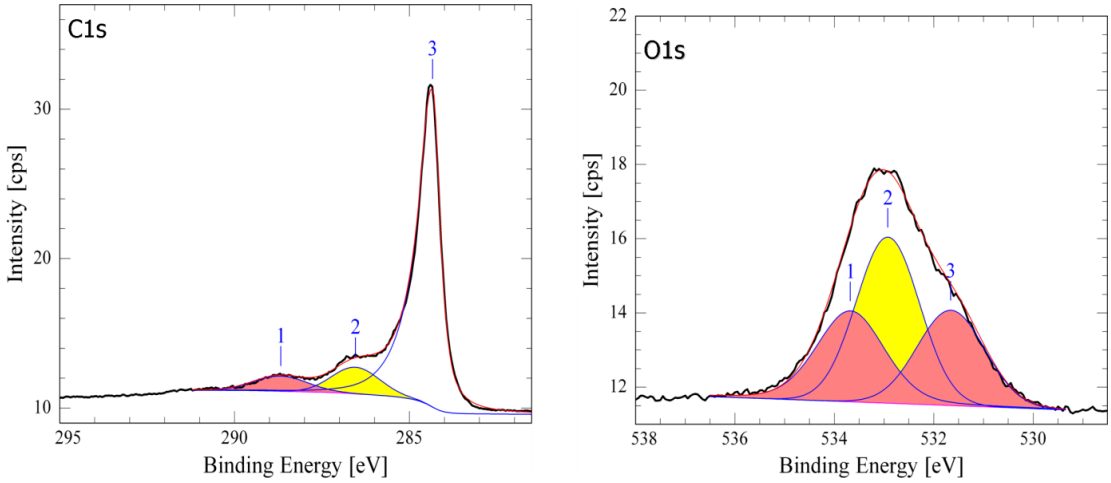

Figure 3.7*. C1s core line (left) and O1s (right) fitting of the acid treated carbon nanotubes: tilt= 25°.*

Lines	BE	Conc.	Bonds
C1s1	288.43	5.7 %	-(C=O)-OH
C1s2	286.37	8.9 %	-C-OH
C1s3	284.40	66.4 %	-C-C
O1s1	533.57	5.2 %	-(C=O)-O*H
O1s2	532.81	8.5 %	-C-O*-H
O1s3	531.75	5.4 %	-(C=O*)-OH

Table 3.2. *Quantitative analysis obtained from the C1s and O1s core lines for acid treated carbon nanotubes.*

Morphological characterization of the cut CNTs were performed by scanning electron microscopy analysis of a drop of acid treated CNTs spread on a gold substrate. Figure 3.8A

shows the SEM images of the CNT samples revealing a large distribution of the nanotubes length. In figure 3.8 B the histogram of the length distribution is reported.

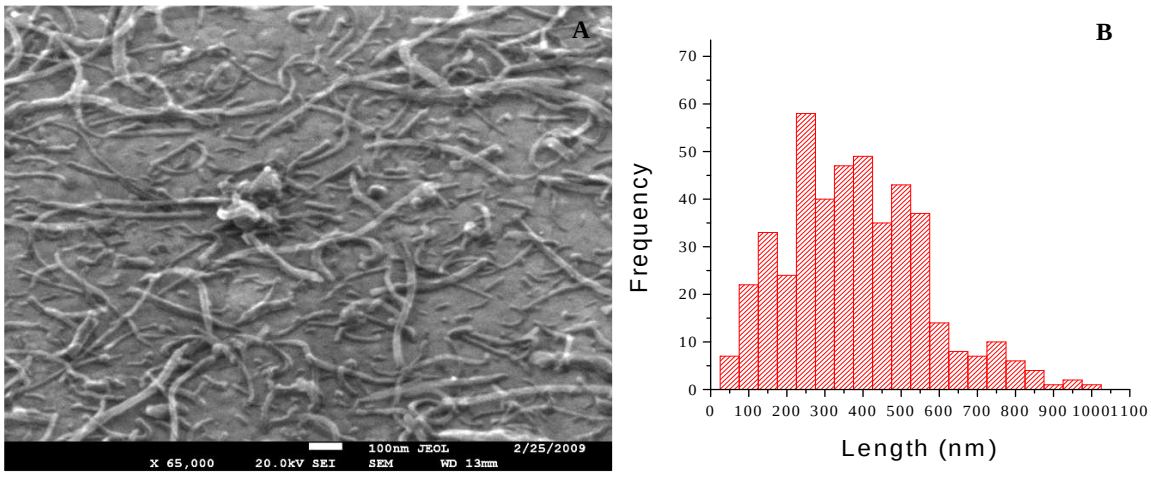

***Figure 3.8**:* **(A)** *SEM image of the acid treated carbon nanotubes deposited on gold substrate,* **(B)** *histogram of the length distribution.*

The length distribution shows the presence of CNTs with length between 0 and 180 nm, that were produced by the cutting procedure. The presence of these shortened CNTs confirms the efficiency of the procedure. On the other hand the fraction of carbon nanotubes with length lower than 200 nm is a minority part of the total length fraction.

Functionalization of the carbon nanotubes with thiol groups

Reaction 2 of Figure 3.1 was carried out in an ethanol suspension for 24 h under stirring with the aid of a condensation reagent DCC (dicyclohexylcarbodiimide). The product was analyzed by FTIR spectroscopy in order to check the effective reaction yield. In Figure 3.9 the FTIR spectrum of the thiol-functionalized carbon nanotubes (CNT-S) in the region 1500-1800 cm^{-1} corresponding to the amide band is presented.

As seen in figure 3.9 the peak position (1657 cm^{-1}) is compatible with the presence of amidic bond confirming the high yield of the reaction. In order to assess the presence of functional thiol groups on the surface of the nanotubes some milliliters of gold nanoparticles solution (D~10 nm *Aldrich*) were added at the nanotubes suspension. The obtained solution was stirred for 10 minutes, then analyzed by visible spectroscopy.

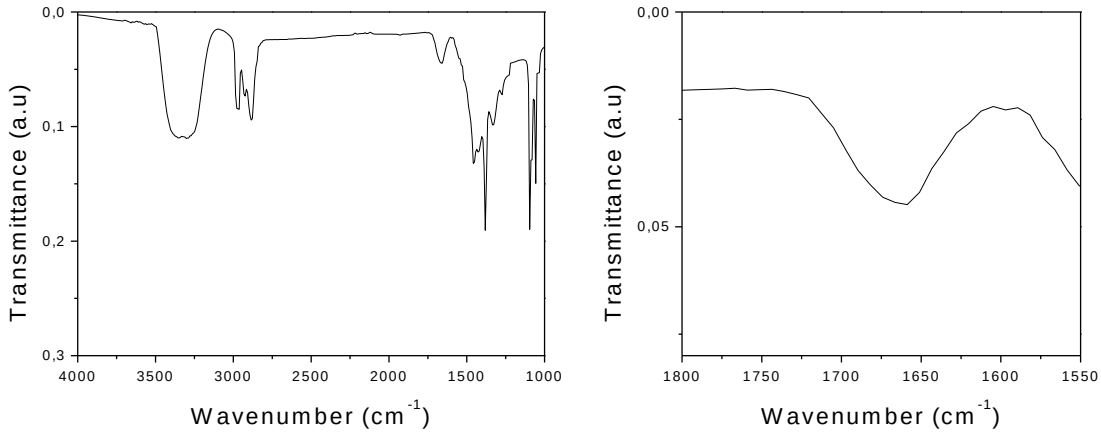

Figure 3.9. Left *FTIR of the CNTS suspension in ethanol.* ***Right*** *snapshot of the amidic bond region.*

In figure 3.10 the absorption spectrum of gold nanoparticles solution is shown.

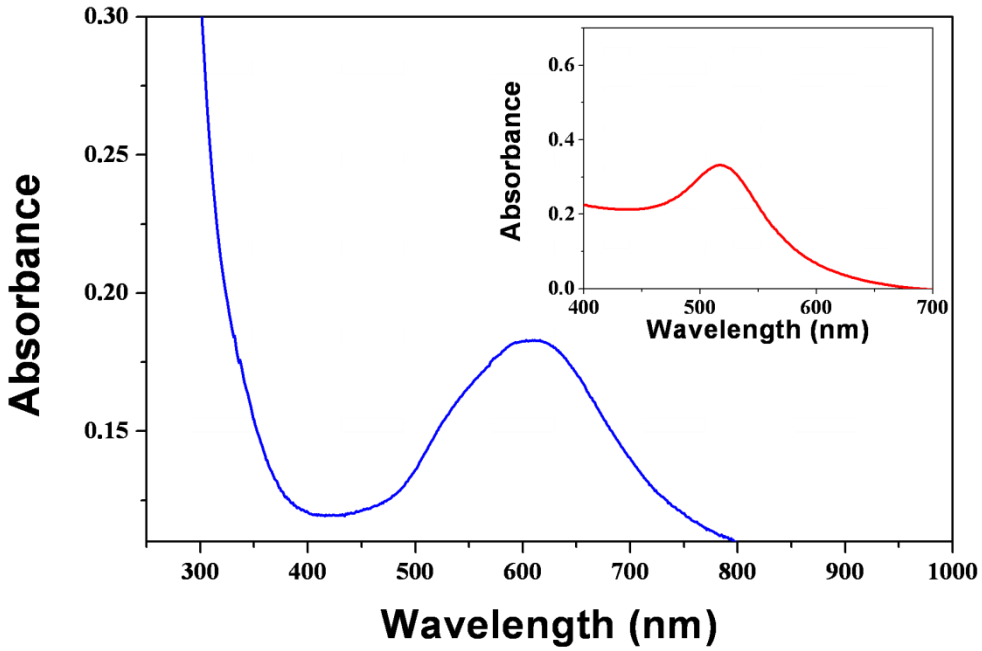

Figure 3.10. *UV-Visible absorption spectra of CNTS-AuNP and (insert) free gold nanoparticles.*

The typical absorption band due to the Surface Plasmon Resonance (SPR) of gold nanoparticles falls at 518 nm (see insert).

In presence of CNTs-AuNP a sensible broadening and red-shift of the plasmon resonance band is obtained. The spectral shoulder at around 520 nm is associated to isolated gold nanoparticles bonded to the CNTs. The main peak at ~ 600 nm could be assigned to gold nanoparticles aggregates adsorbed to the CNTs walls.

The scanning electron microscopy images of figure 3.11 confirm the presence of both isolated and AuNP aggregates bonded to the CNTs. The formation of nanoparticles aggregates could be due to the break of the electrostatic repulsion generated by the citrate ions around the gold nanoparticles with the carbon nanotubes surface.

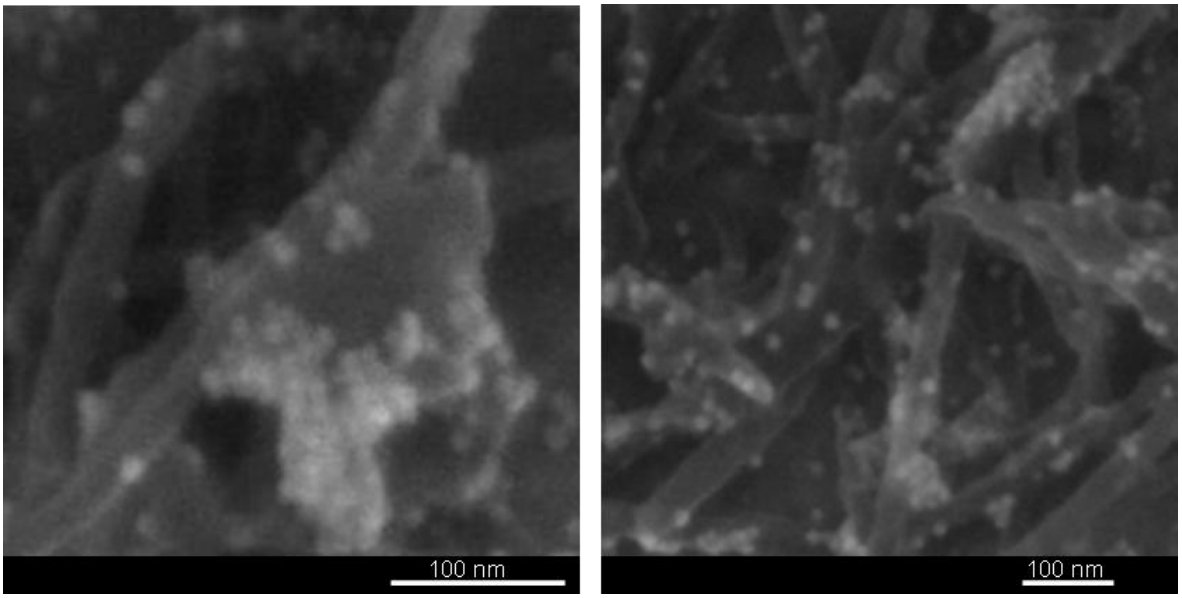

Figure 3.11. *Scanning electron microscopy of CNT-S functionalized with 10 nm gold nanoparticles.*

Thiol groups are known to form stable chemical bond with gold (ΔG ~ 40 kcal/mol) [22]. Increase of the bandwidth and red shift of the peak maximum was already described by Hu et al. [23] for thiol functionalized CNTs with 5 nm gold nanoparticles. Furthermore, according to Zhong's et al. [24], the position of surface plasmon band depends on the particles size distribution, the distance among the Au nanoparticles and the interaction of Au nanoparticles with the molecules on the surface. The effect of the nanoparticles size distribution can be excluded in our case because nanoparticles with narrow size distribution were used.

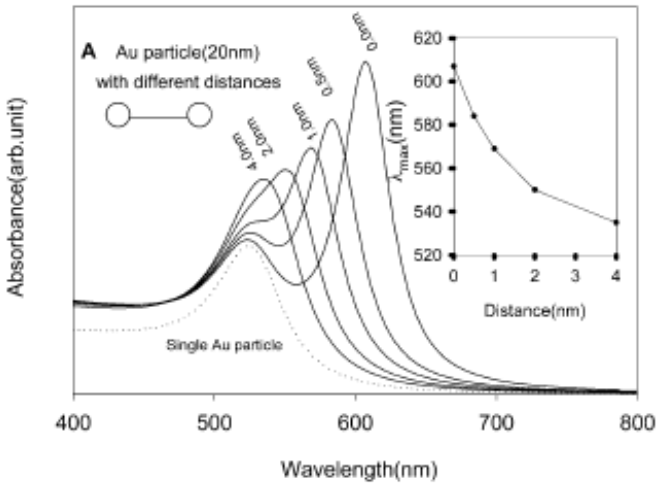

Figure 3.12. *Electrodynamic modelling calculations for Au nanoparticles. Change of extinction spectra for 20 nm diameter particles with interparticle distance. Inset is the peak shift vs interparticle distance* [24].

The bathochromic shift is likely to be produced by a change of the nanoparticles disposition and could be an indicator of the decrease of the interparticles spacing induced by the thiol linkage. As the distance decreases, the SPR peak shifts to longer wavelengths. The maximum peak shift is observed when the distance between the nanoparticles approaches zero. In this situation the electrodynamic interactions between the nanoparticles is maximum. At the other extreme, when the interparticle spacing increases, classical single particle Mie theory can be applied to describe the resultant spectra. Since a consistent percentage of thiol is expected to be present on the nanotubes tip more than one gold particle are expected to be adsorbed.

Adsorption of thiol functionalized CNT on gold substrate

The CNTs absorption on the gold substrate, as shown in step 3 of figure 3.1 was obtained by dipping the gold plate into a diluted suspension of CNT-S for 2 h (CNT-S/Au). The resulting sample was analyzed by XPS as shown in figure 3.13. The C1s core line is fitted with four components. Component 4 at 284.4 is assigned to the graphitic carbons in sp2 hybridization of the CNTs, component 3 at ~285 to hydrocarbons, while component 2 at ~ 286 eV is referred to –C-O bonds and finally component 1 at 288.6 is assigned to amidic carbon in agreement with literature [25]. The O1s core line shows four components assigned to

carboxylic bonds due to unreacted carboxylic groups (component 1), oxydrilic (component 2), amidic (component 3) and metal oxide bonds (component 4) due to contaminations.

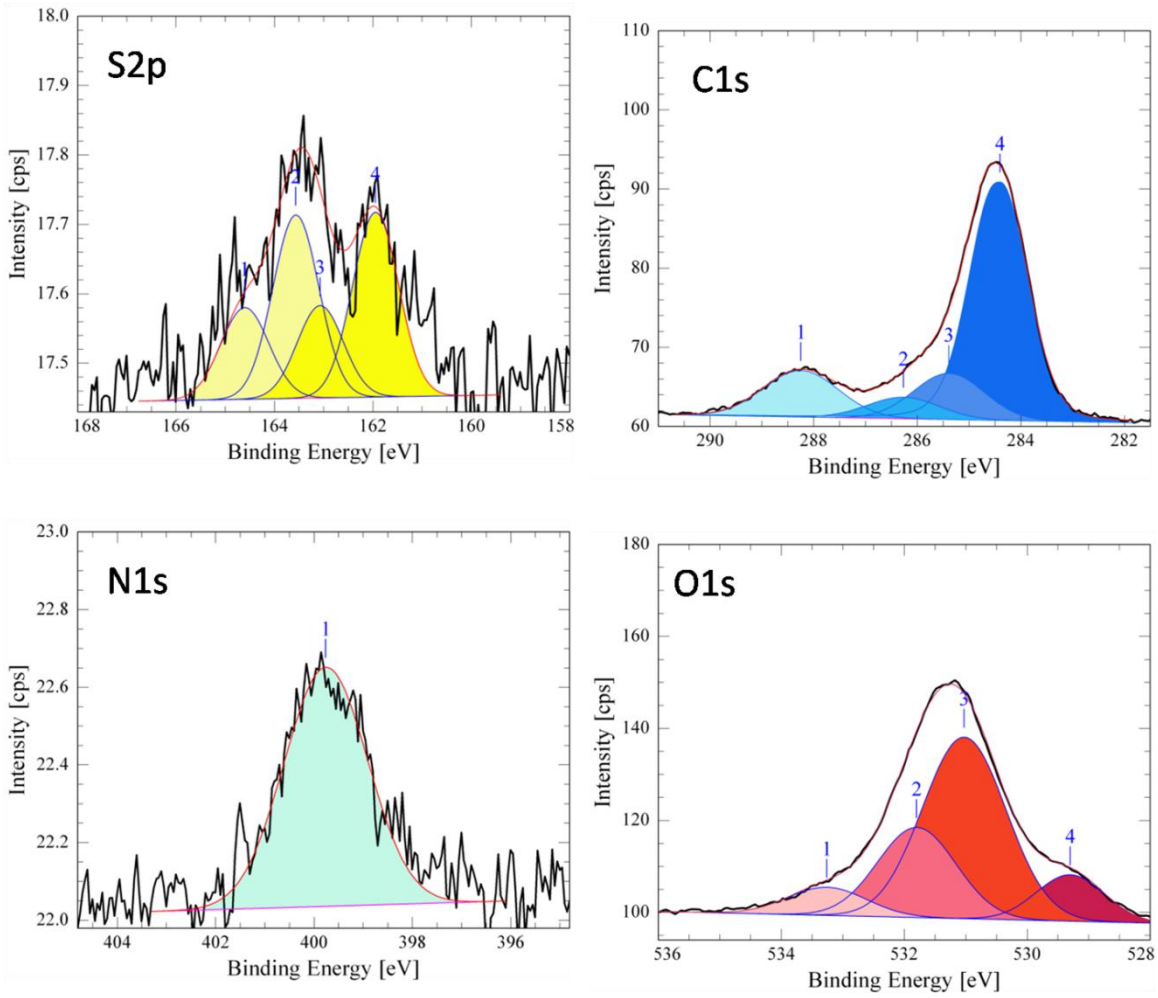

Figure 3.13. *XPS core lines of the CNTS/Au samples after 2 h of absorption time obtained at tilt of 30°. C1s, O1s, S2p and N1s core lines.*

The S2p core line is split into two spin-orbit doublets each assigned to different chemical bonds: doublet 1 (163.9 and 165 eV) refers to free thiol (S-H), while doublet 2 (162 and 163.1 eV) is assigned to S-Au bond. The integral intensities of these two doublets are pretty equal, and in agreement with pictures where vertically aligned CNT-S are sulphur bonded to the gold plate while the other is free on the surface. N1s core line shows a peak at 399.76 eV in agreement with the BE of nitrogen in amidic bonds [25]. In Table 3.3 the BE and atomic abundances of the component elements are summarized as well as the identification of the chemical species.

Lines	BE(eV)	Conc. (at. %)	Bond
C1s1	288.22	5.82	-(C=O)-NH
C1s2	286.31	6.48	-C-OH
C1s3	285.23	9.76	$-CH_2$-S, $-CH_2$-N
C1s4	284.41	33.09	-C-C
O1s1	533.50	2.19	-(C=O)-O*H
O1s2	532.01	6.70	-C-OH
O1s3	531.10	8.89	-(C=O*)-NH, (OH)
O1s4	529.53	3.00	MeO
S2p2	163.63	1.23	$-CH_2$-SH
S2p4	161.98	1.10	$-CH_2$-S-Au
N1s	399.76	3.80	-(C=O)-NH
Au4f	84 (87.67)	19.25	Au^0

Table 3.3. *XPS Binding energy and atomic abundances of the elements and chemical bonds for the CNTS/Au sample.*

Atomic force microscopy measurements were acquired in tapping mode on the sample with 2 h of absorption time. The figure 3.14 shows a 3D visualization of the sample surface as obtained by tapping mode atomic force microscopy. The image shows the presence of needle-like structures with high ranging from 50 to 200 nm. The 2D image (figure 3.15) shows that many of these features are probably composed of multiple CNTs close to each other. This can also explain the apparent giant width of some features present. For example, the section analysis of the three aligned spot is reported lower diagrams of figure 3.15. The peaks have a width of half maximum of around 100 nm. The width of these peaks are explained considering the diameter of a MWCNTs (10-30 nm), the tip curvature (r=10 nm) and the possibility of deflection of the CNT induced by the AFM tip or the non totally normal position of the CNT on the substrate.

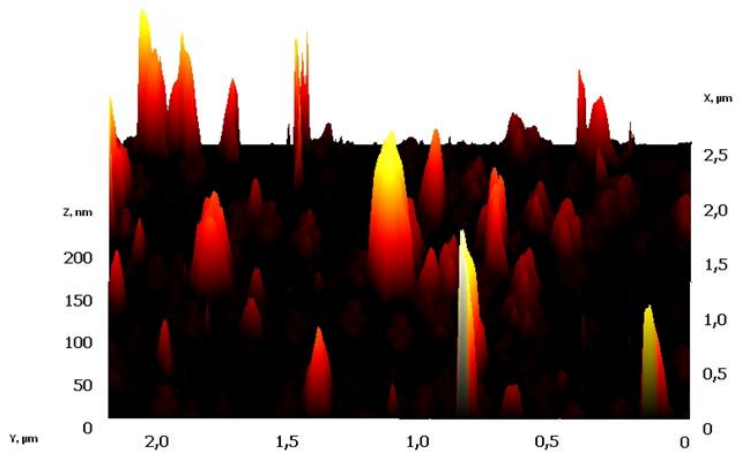

Figure 3.14. *Atomic force microscopy images of the samples obtained after 2 h of absorption.*

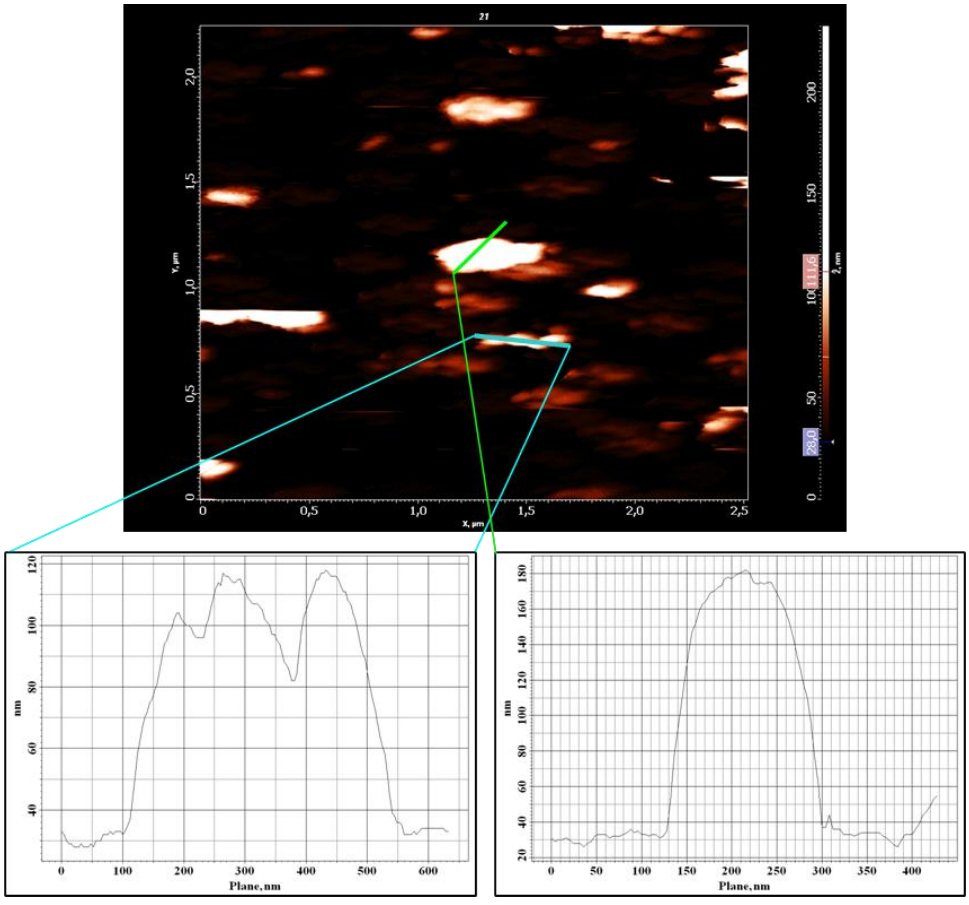

Figure 3.15. *2D atomic force microscopy images of the samples obtained after 2 h of adsorption time.*

The SEM analysis on the CNT-S/Au sample after 2h of dipping shows the presence of some CNTs placed parallel to the surface (Fig 3.16a). These are CNTs physically absorbed on the substrate and not removed by the cleaning procedure. On the other hand, the SEM images show also vertically aligned nanotubes (Figure 3.16 b, c, d). In particular, in the figure 3.16d a well resolved CNT tip image is presented. This confirms the efficiency of the cutting procedure that allows to total remove the caps at the end of the tubes creating a perfect cylindrical tip. The density of vertical aligned CNTs on the samples measured on AFM analysis is in agreement with literature experimental data on multi-walled carbon nanotubes [26] and slightly lower than that obtained with SWCNTs [11]. On the other hand, Lim et al. pointed out that flexible SWNT with many thiol groups at its ends likely bends on metal surface to form a "bow-type" structure [27].

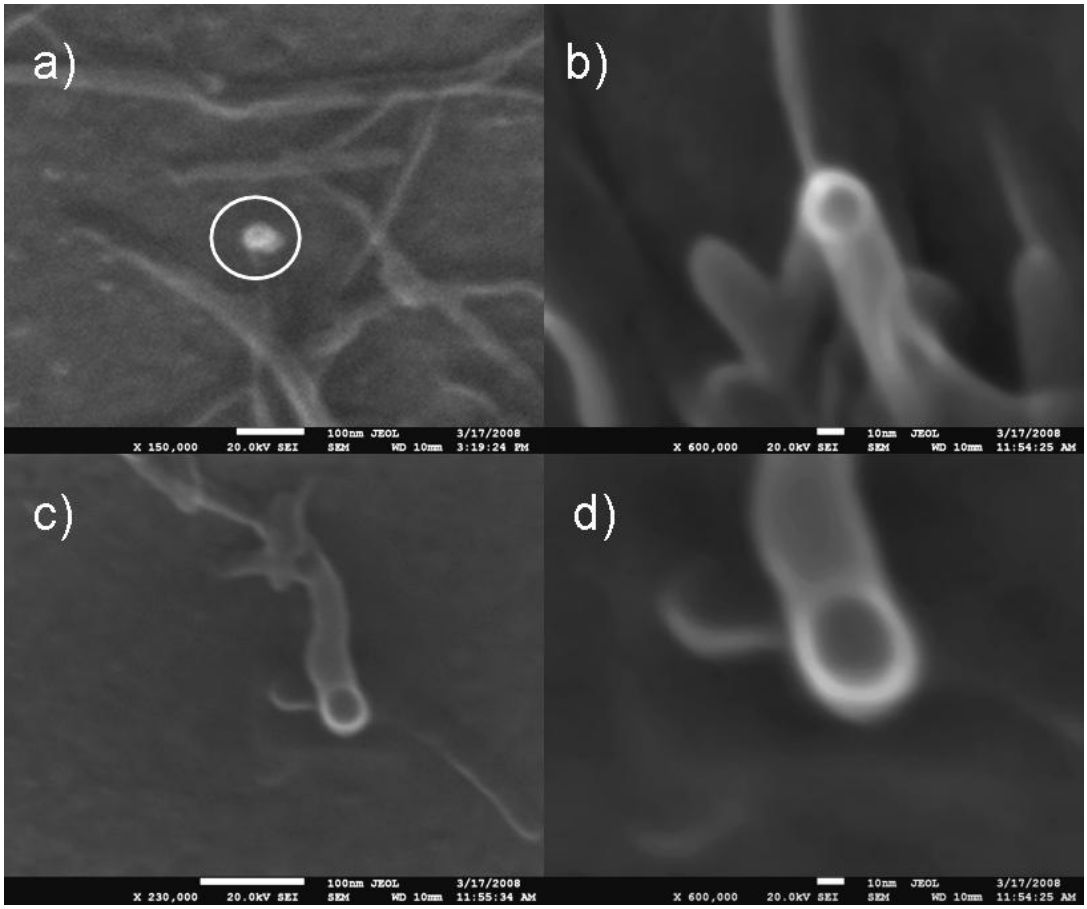

Figure 3.16. *Field emission gun-Scanning Electron Microscopy of CNTS/Au after 2 h of absorption in the CNT suspension.*

This would be induced by the energy gain obtained by the adsorption of both ends of the nanotubes to the metal, that compensates the energy required to bend the nanotubes. This also explains the incompatibility between AFM and electron microscopy results that appears in some works concerning SWCNTs [28, 29]. With multi-walled carbon nanotubes the energy required to bend the tube is considerably higher than the gain due to the Au-S bond formation. In this situation the CNT will probably stand upright on surface with only one end attached, forming a needle-like structure.

4.1.3 References

[1] S. Iijima, T. Ichihashi, *Nature* **363** (1993) 603.

[2] S. Fan, M.G. Chapline, N.R. Franklin, T.W. Tombler, A.M. Cassell, H. Dai *Science* **283** (1999) 512.

[3] P. G. Collins, A. Zettl, H. Bando, A. Thess, R. E. Smalley, *Science* **278** (1997) 100.

[4] S. S. Wong, E. Joselevich, A. T. Woolley, C. L. Cheung, C. M. Lieber *Nature* **394** (1998) 52.

[5] G. L. Che, B. B. Lakschmi, E. R. Fisher, C. R. Martin, *Nature* **393** (1998**)** 346.

[6] X. Yu, D. Chattopadhyay, I. Galeska, F. Papadimitrakopoulos, J. F. Rusling *Electrochem. Comm*. **5** (2003) 408.

[7] J. Okuno, K. Maehashi, K. Kerman, Y. Takamura, K. Matsumoto, E. Tamiya, *Biosens. Bioelectron.* **22** (2006) 2377.

[8] J. Li, H.T. Ng, A. Cassell, W. Fan, H. Chen, Q. Ye, J. Koehne, J. Han, M. Meyyappan, *Nano Lett*. **3** (2003) 597.

[9] J. V. Veetil, Y. Kaiming *Biotechnol. Prog*. **23** (2007) 517.

[10] M. Terrones, N. Grobert, J.P. Zhang, H. Terrones, J. Olivares, W.K. Hsu, J.P. Hare, A.K. Cheetham, *Chem. Phys. Lett.* **285** (1998) 299.

[11] Z.F. Liu, Z.Y. Shen, T. Zhu, S.F. Hou, L.Z. Ying, Z.-J.Shi, Z.-N. Gu, *Langmuir* **16** (2000) 3569.

[12] X.F. Yu, T. Mu, H.Z. Huang, Z.F. Liu, N.Z. Wu, *Surf. Sci.* **461** (2000) 199.

[13] X. Zhang, J.C. Shen, *Adv. Mater*. **11** (1999) 1139.

[14] H. Wei, S. Kim, S. N. Kim, B. D. Huey, F. Papadimitrakopoulos H. L. Marcus *J. Mater. Chem.* **17** (2007) 4577.

[15] D. Chattopadhyay, I. Galeska, F. Papadimitrakopoulos, *J. Am. Chem. Soc.* **123** (2001) 9451.

[16] P. Tan, L. An, L. Liu, Z. Guo, R. Czerw, D.L. Carroll, P.M. Ajayan, N. Zhang, H. Guo *Phys.Rev. B* **66** (2002) 245410.

[17] V.H. Crespi, M.L. Cohen, and A. Rubio *Phys. Rev. Lett.* **79** (1997) 2093.

[18] T. J. Mason and J. P. Lorimer, *Sonochemistry: Theory, Applications and Uses of Ultrasound in Chemistry* Halsted, New York, (1988).

[19] H. Hu, A.P. Yu, E. Kim, B. Zhao, M.E. Itkis, E. Bekyarova *J Phys Chem B* **109** (2005) 11520.

[20] P.M.Th.M. van Attekum, G.K. Wertheim, *Phys. Rev. Lett.* **43** (1979) 1896.

[21] D. Briggs, J. Grant *Surface Analysis by Auger and X-Ray Photoelectron Spectroscopy* IM Publication (2003).

[22] F. Schreiber *Prog. Surf. Sci.* **65** (2000**)** 151.

[23] J. Hu , J. Shi, S. Li, Y. Qin, Z.-X. Guo, Y. Song, D. Zhu *Chem. Phys. Lett*. **401** (2005) 352.

[24] Z. Zhong, S. Patskovskyy, P. Bouvrette, J.H.T. Luong, A. Gedanken, *J. Phys. Chem. B* **108** (2004) 4046.

[25] NIST X-ray Photoelectron Spectroscopy Database

[26] Y. Lan , E. Wang , Y. Song , Z. Kang , M. Jiang , L. Gao, S. Lian, D. Wu, L. Xu, Z. Li *J. Coll. Interf. Sci.* **284** (2005) 216.

[27] J. K. Lim, W. S. Yun, M. Yoon, S. K. Lee, C. H. Kim, K. Kim, S. K. Kim *Synth. Met.* **139** (2003) 521.

[28] B. Wu, J. Zhang, Z. Wei, S.M. Cai, Z.F. Liu, *J. Phys. Chem. B* **105** (2001) 5075.

[29] J.J. Gooding, R. Wibowo, J.Q. Liu, W.R. Yang, D. Losic, S. Orbons, F.J. Mearns, J.G. Shapter, D.B. Hibbert, *J. Am. Chem. Soc.* **125** (2003) 9006.

CHAPTER 4

4.1 Synthesis and characterization of carbon nanotubes films decorated with gold nanoparticles

4.1.1 Introduction to electrophoretic deposition

One of the most important challenges in carbon nanotubes science is to be able to manipulate CNTs, individually or collectively, to produce an ordered array for a given application. One most important technique developed for manipulating CNTs is the electrophoretic deposition (EPD). EPD is commonly employed in processing of coatings and composite materials [1, 2]. It is a very efficient process for production of films or coatings from colloidal suspensions. Electrophoretically deposited materials exhibit good microstructure homogeneity and high packing density. The technique allows the application of coatings, thin and thick films, the shaping of bulk objects, and the infiltration of porous substrates. The interest in the EPD technique is driven not only by its applicability to a great variety of materials but also by its simplicity and low cost. EPD is achieved via the motion of charged particles, dispersed in a suitable solvent, towards an electrode under an applied electric field. The method can be applied also to nanoparticles colloidal suspensions [1]. EPD is a two-step process. In the first step, particles suspended in the solvent are forced to move towards an electrode by applying an electric field (electrophoresis). In the second step, the particles collect at the electrode and form a coherent deposit (deposition). Deposition occurs only on conducting surfaces, however non-conductive substrates can be infiltrated by using EPD [3]. All these advantages can be also exploited for forming films and coatings of CNTs. The schematic diagram of an EPD cell for electrophoretic deposition of carbon nanotubes is shown in Fig. 4.1.

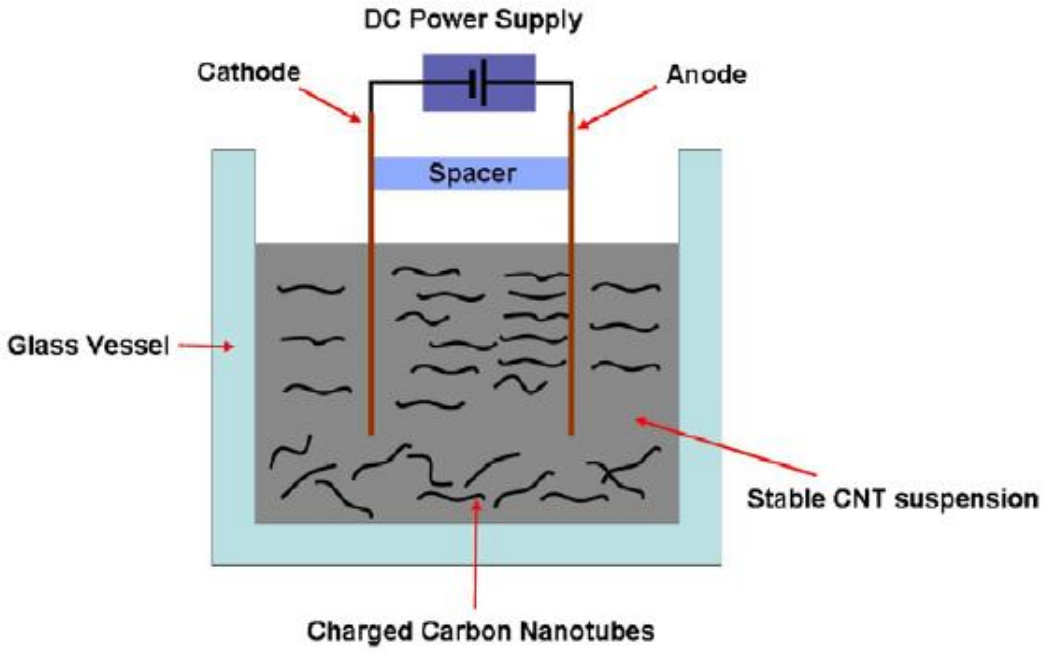

Figure 4.1. *Schematic diagram for the electrodeposition of CNTs on metallic substrates.*

Preparation of a stable dispersion of CNTs in a suitable solvent is a prerequisite for successful EPD. The most common strategy is the production of an electrostatically stabilised dispersion, which requires the solubilisation of the particles. The stability of CNT suspensions, determined by ξ-potential measurements, has been studied mainly in aqueous and ethanol based suspensions [4, 5]. As-produced CNTs have a small and positive ζ-potential in the acidic region with an isoelectric point in the pH range 5–8. After oxidation, the presence of surface acid groups dramatically shifts the isoelectric point to values often below pH 2. It has been shown that the presence of charger salts can play an important role in improving the adhesion of CNTs to substrates and in increasing the deposition rate in the EPD process [6]. The salts can also contribute to the stability of the suspensions by associating a charge with the CNT surface in suitable solvents. The migration direction of CNTs in suspension during EPD is controlled by the surface charge; for example, oxidised nanotubes are typically negatively charged and attracted to the positive electrode (anode) [7].

4.1.2 Synthesis of carbon nanotubes films using electrodeposition

In figure 4.2 the reaction scheme for the electrodeposition of CNTs on gold and platinum substrates is presented:

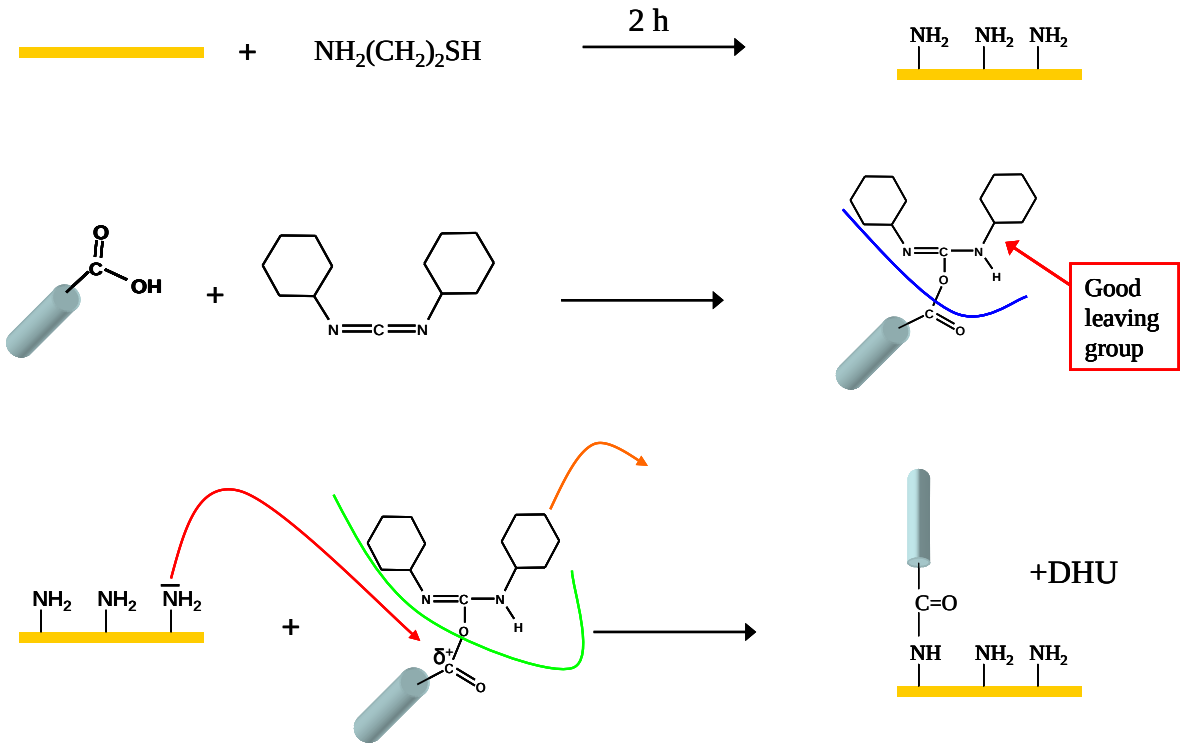

Figure 4.2. *Reaction scheme for the electrodeposition of CNTs on gold and platinum surfaces.*

The first step is the adsorption of cysteamine on the metallic surface (gold or platinum). The effectiveness of this reaction was checked in some papers presented in literature [8].

Following these works, an 80% of coverage is expected after 1 hour of adsorption on gold surface. The XPS S2p and N1s core lines obtained after dipping a gold plate in an ethanolic solution of cysteamine for 2 h is reported in figure 4.3.

The S2p core lines show three doublets, which have the principal components $S2p_{3/2}$ located at 163.7, 162.1 and 161.3 eV. Respectively these three components are assigned to S-H and S-Au bonds, while the component at around 161 eV, just observed in the work of Wirde, [8] is assigned to sulphur atoms with a higher degree of coordination to gold atoms.

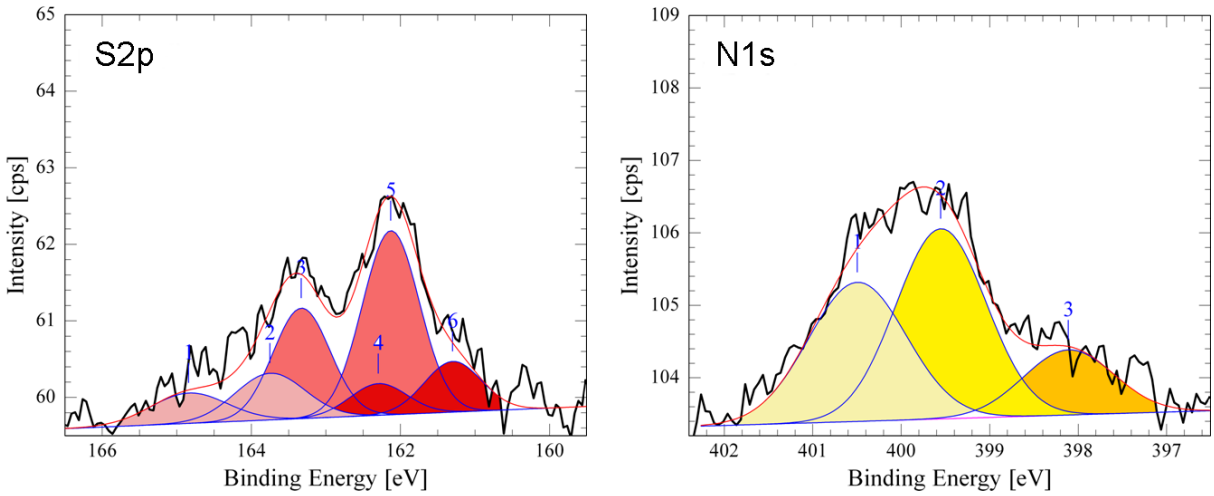

Figure 4.3. *S2p and N1s peak fitting of cysteamine layer absorbed on the gold plate for 2 hours.*

The N1s core line is composed by three different atomic species, at 400.7, 399.6 and 398.1 eV. The first two are associated to the aminic groups on the surface, in particular the peak at higher BE could reflect changes in the interactions between the nitrogen atoms and surrounding atoms because of a high surface coverage. The possibility of the cysteamine to be present in two conformations when absorbed on metal was just observed in literature by means of Raman spectroscopy [9].

In this work two conformer named trans and gauche were assumed to be present (see figure 4.4). In the gauche conformation, the aminic group can interact with the gold surface. Previous XPS studies on the absorption of cysteamine molecules on gold show the presence of a component at 398 eV that some authors associated to the NH_2—Au bond [10].

The second step reported in figure 4.2 is the reaction between the carboxylic groups of the carbon nanotubes and the dicyclohexylcarbodiimide (DCC) molecules. This reaction, described by some of works in literature, [11] shows a high efficiency also at ambient temperature. The last step is the reaction with the aminic groups of the cysteamine layer with the DCC-activated CNTs. This comes through a nucleophilic attack of the ammine on the carbonyl carbon atom in the activated ester with the resultant formation of the amidic bond. The deposition of the carbon nanotubes was obtained by using external electric field induced by a DC generator. In the figure 4.5 the scheme of the apparatus used as well as the scheme of the process is presented.

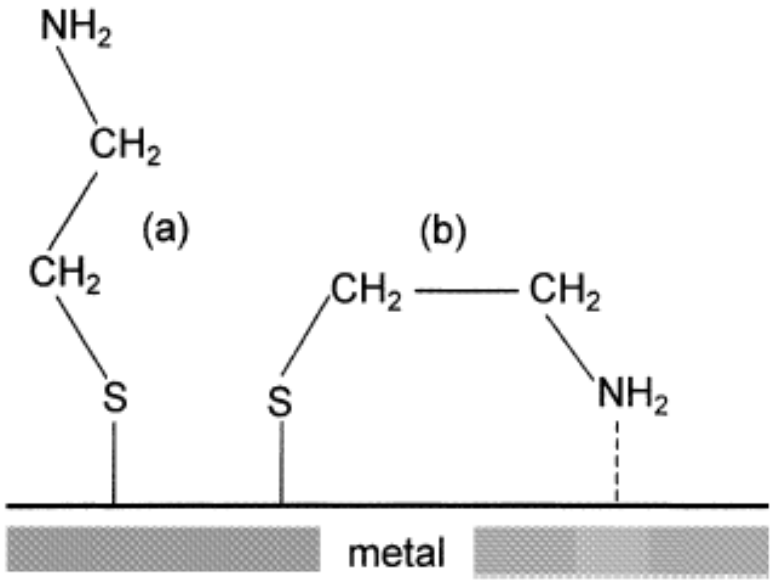

Figure. 4.4. *Possible structures of adsorbed cysteamine molecules: (a) trans conformer, (b) gauche conformer. The terms trans and gauche describe the conformation on the carbon next to the sulphur* [9].

Two gold electrodes were placed at around 1mm distance by an isolating spacer. One of the two electrodes (working) is modified by cysteamine layer as explained previously, while the other (counter) is a pure gold plate. The system was dipped into a diluted ethanolic solution of cut and functionalized CNTs (see chapter 3 for details). A positive potential was applied at the working electrode and a 10 V DC voltage was applied respect to the counter electrode.
The application of the external electric field leads to an orientation of the CNT principal axes in the direction of the electric field force lines. Because of the planar geometry, the field lines are perpendicular to the gold plates, and the negative charges present on the CNTs lead to a migration towards the positive electrode (anode) where the functional groups on the CNTs can react with the aminic groups present at the gold surface.

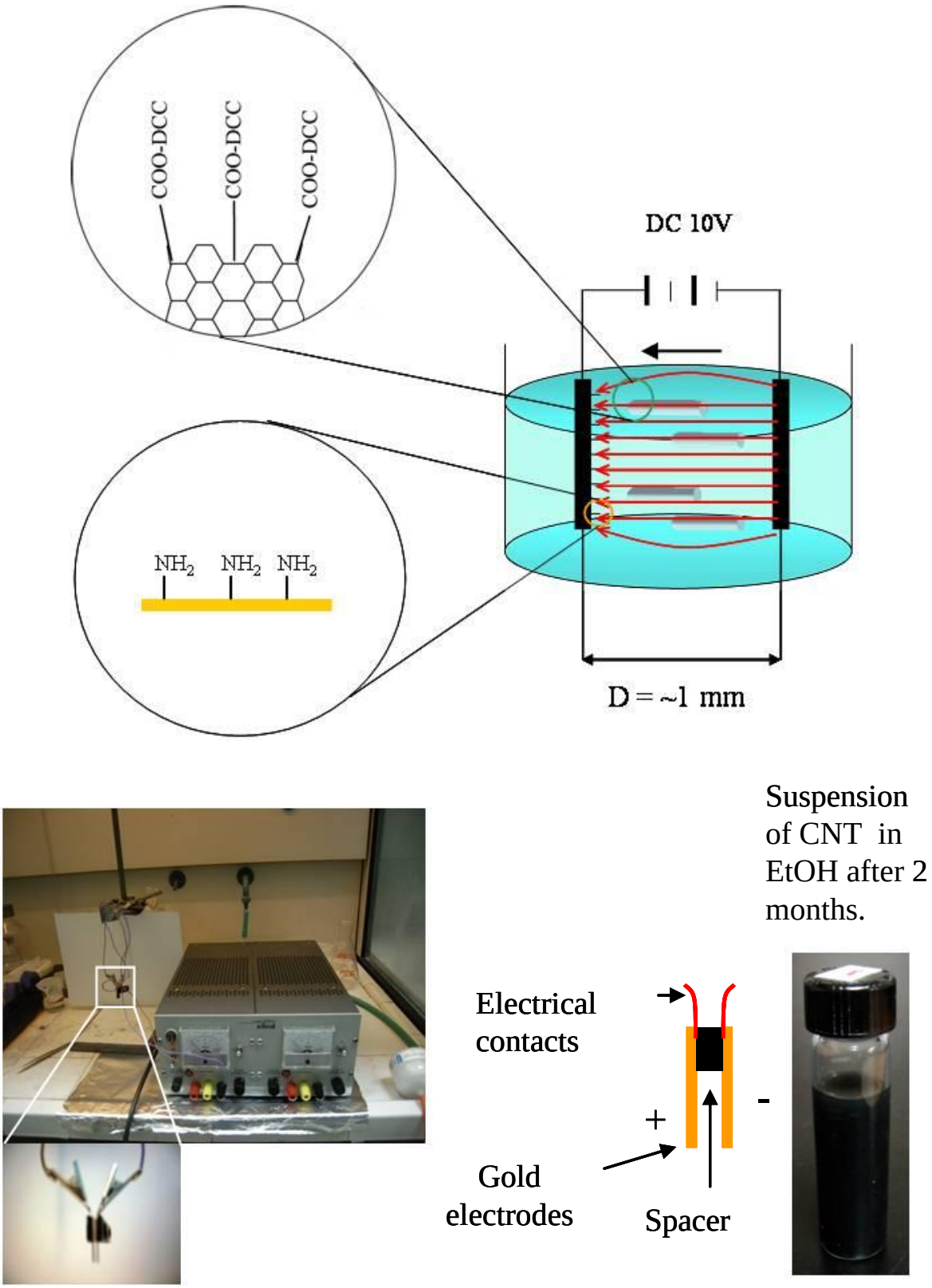

Figure 4.5. *Upper part: scheme of the deposition process. Low part: photo of the DC generator and the electrodes.*

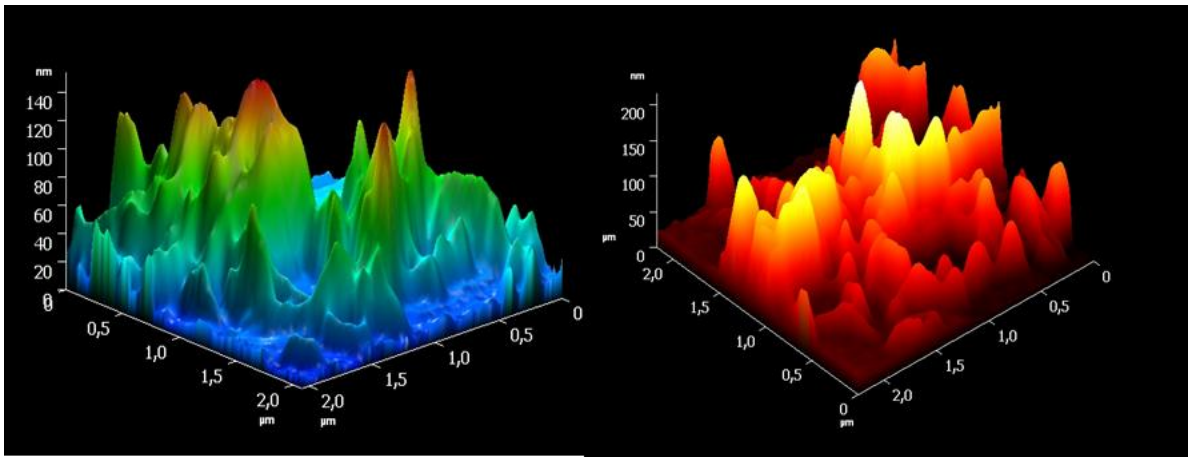

Figure 4.6. *Atomic force microscopy images obtained for 5 minutes of deposition of CNT.*

We exploited tapping mode atomic force microscopy to characterize the formed structures of the thiol-derivatized carbon nanotubes on gold. Figure 4.6 shows the atomic force microscopy images obtained after the deposition of the carbon nanotubes for 5 minutes. After the adsorption, needle-like protrusions appears on the gold surface. The carbon nanotubes immobilized on gold have different lengths and form aggregates. Figure 4.7 shows the histograms of the carbon nanotube lengths calculated from the AFM images. The tube length falls in a range of 30–250 nm .The mean width of the CNTs as revealed by AFM is 60-80 nm. Because of broadening effects induced by the non-negligible dimensions of the AFM tip, these data do not directly reflect the true lateral sizes of nanotubes. The AFM tip used in this work has a typical curvature radius of around 10 nm. Based on a simple geometric consideration, we can roughly estimate the true lateral tube sizes. For an individual nanotube having a true diameter of 10-20 nm, tip broadening will give a lateral value of ca. 30-40 nm in an AFM image. Therefore values of 60-80nm are an indication of aggregated nanotubes. Figure 4.8 is the section analysis of the AFM image. Almost all bundles have fine structures, suggesting the existence of different nanotubes lengths within the individual bundles. The fine structures observed in the section (figure 4.8) also suggest the standing-up orientation because otherwise we would observe a flat cross section for the stacked nanotubes along the long axis direction. This is reasonable because direct contact between the hydrophobic nanotubes sidewalls and the hydrophilic amino surface is energetically unfavourable. It should be pointed out that the nanotubes may tilt some degree from the surface normal, depending on

how many carboxylic groups at the tube end (typically more than one) are involved in the condensation reaction. The cutting angle of the nanotube at the open end formed during the oxidative shortening process may also affect its tilt angle on the surface.

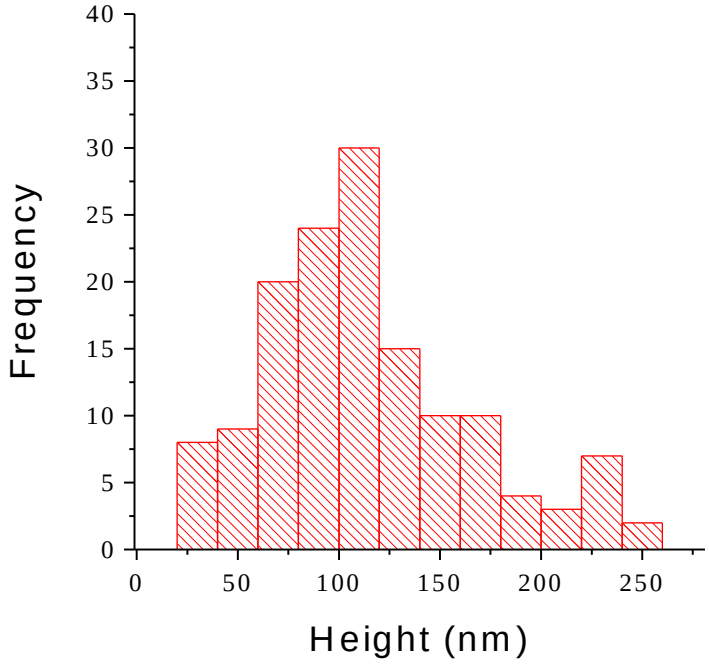

Figures 4.7. *Histograms of nanotubes lengths calculated from the AFM images.*

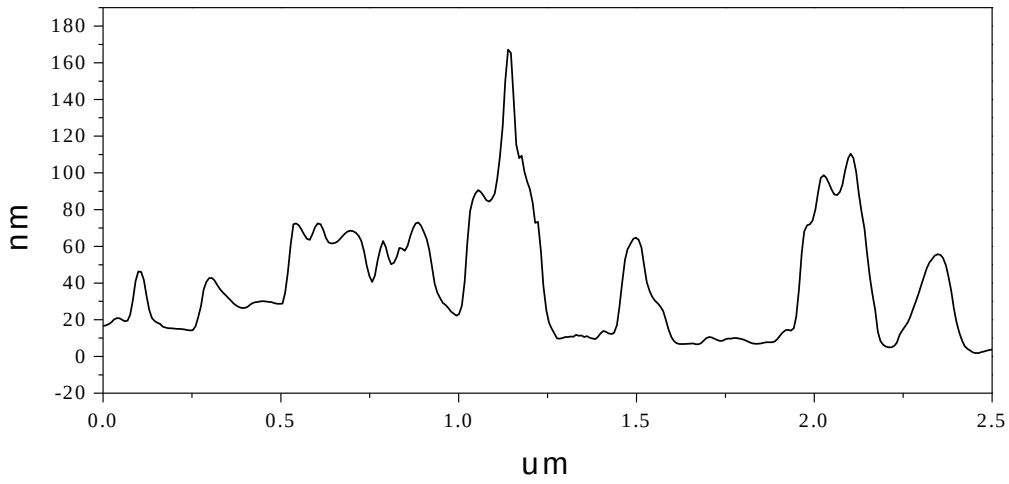

Figure 4.8. *Section of the AFM image of the immobilized nanotubes on the gold surface.*

The XPS analysis results are reported in figure 4.9. The C1s core line is fitted with four components, assigned to sp2 bond (284.45 eV), sp3 bonds (285 eV), C-O bonds (286.3 eV) and amidic and carboxylic bonds (288.4 eV). The O1s core line is fitted with four components assigned to carboxylic bonds due to unreacted carboxylic groups (533.5 eV), oxydrilic (532 eV), amidic (531.5 eV) and metal oxide bonds (530 eV) due to contaminations.

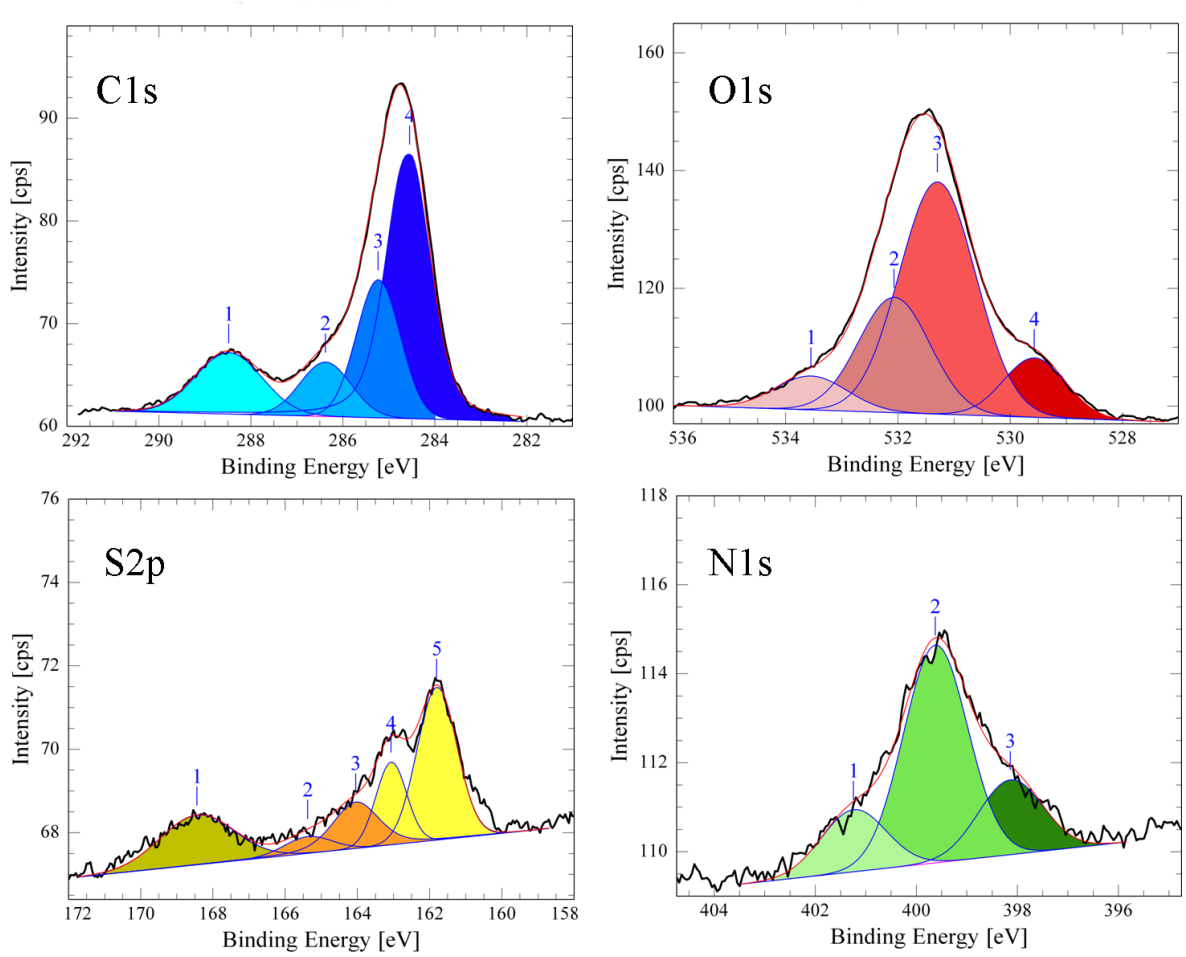

Figure 4.9. *XPS core lines of the CNTS/Au samples after 5 minutes of deposition with 10 V potential C1s, O1s, S2p and N1s core lines.*

The S2p core line is splitted into two spin-orbit doublets each assigned to different chemical bonds: doublet 1 (163.9 and 165 eV) refers to free thiol (S-H), while doublet 2 (162 and 163.1 eV) is assigned to S-Au bond, the component at 168.5 eV is associated to the presence of oxidized sulphurs. The integral intensity of the doublets referred to the Au-S bonds is predominant in this spectrum because of the absence of thiol groups on the surface of the CNTs.

N1s core line shows a peak at 401 eV assigned to NH^{3+} groups probably present as result of ionization of NH_2 group of cysteamine on the surface, the peak at 399.76 eV is assigned to amidic nitrogen, while the peak at 398 eV is assigned to aminic groups bonded to the gold surface.

Increasing of the deposition time to 20 minutes at the same previous conditions leads to a complete coverage of the metallic sample with the formation of a high-density CNT carpet on the surface of the anode.

The scanning electron microscopy images of figure 4.10, show the morphology of the sample after 20 minutes of deposition.

The 45° tilt images display a high-density disorder layer of CNTs with a preferential vertical orientation of the CNTs. The images show also the formation of some big bundles of CNTs probably due to the aggregation of the CNT during the electrophoretic deposition.

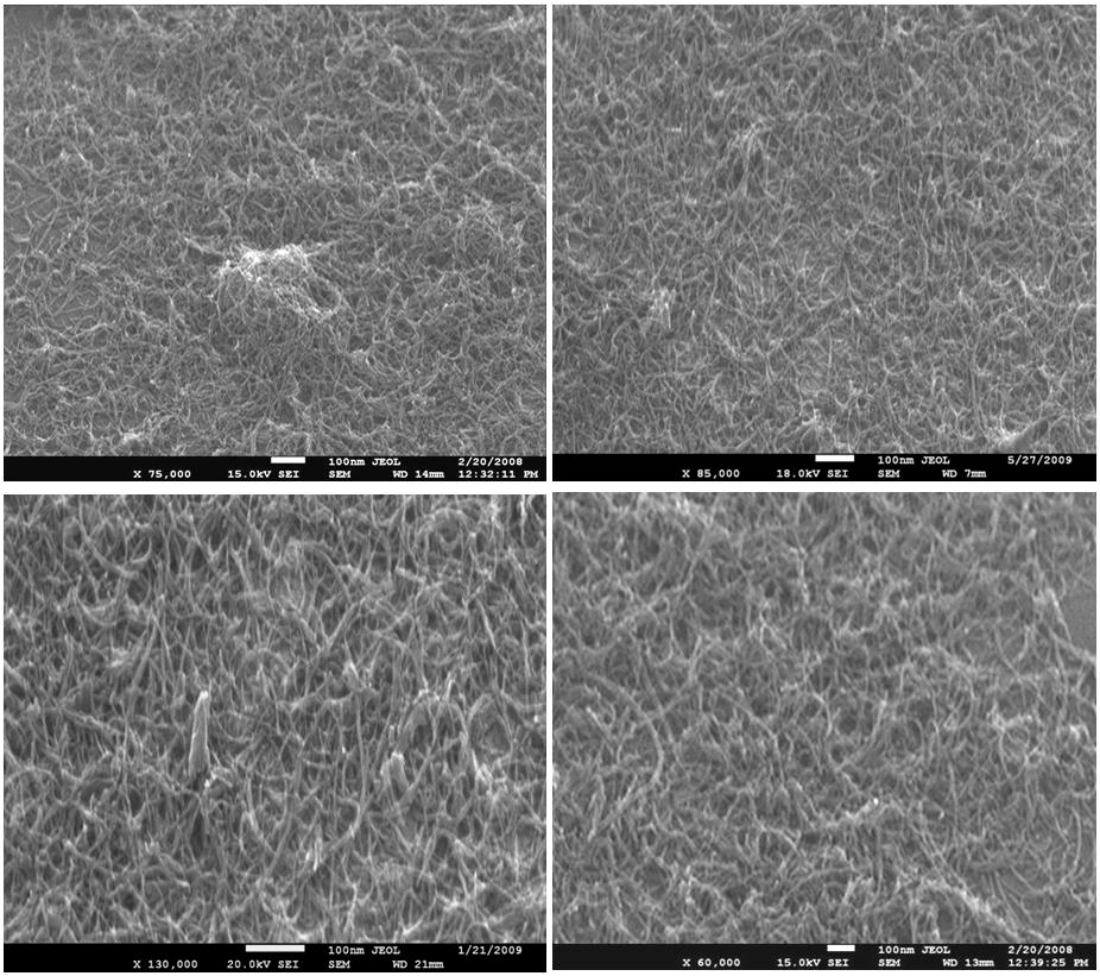

Figure 4.10. *45°tilt SEM images of the carbon nanotubes film.*

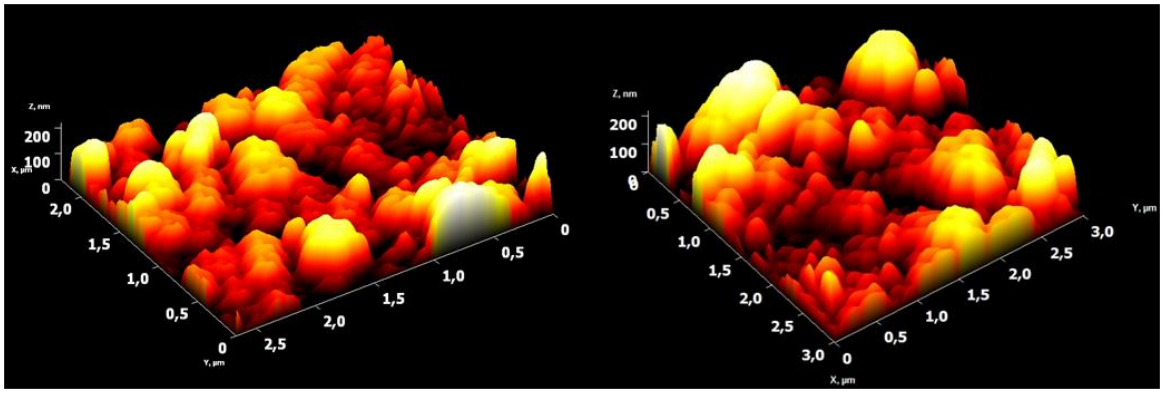

Figure 4.11. *AFM 3D imaging of carbon nanotubes deposited for 20 minutes***.**

In figure 4.11 the tapping mode AFM images of the sample are reported. The morphology of the surface appears to be very inhomogeneous and composed by peaks that are assigned to the CNTs tips exposed on the surface. The height values reported in the images does not correspond to the true thickness of the CNTs film. This is due to the impossibility of the AFM tip to reach the metallic sample because of the high density of the CNTs films.

4.1.3 Adsorption of preformed gold nanoparticles on a Pt/CNT surface

The adsorption of the gold nanoparticles was performed using a platinum substrate instead of gold to avoid interferences when analysing of the Au 4f XP spectrum. Two different chemical procedures were applied:

1. dipping of the Pt/CNT system in a 1 mM solution of cysteamine, to functionalize the exposed CNTs tip with thiol groups and successive immersion of the sample in the gold nanoparticles solution.

2. dipping of the Pt/CNTs system in a solution containing gold nanoparticles-modified by cysteamine layer.

1) ***Dipping of the Pt/CNT system in a 1 mM solution of cysteamine, to functionalize the exposed CNTs tip with thiol groups and successive immersion of the sample in the gold nanoparticles solution***

This procedure is composed by two steps: the first is the dipping of the Pt/CNTs samples in a 5mM solution of cysteamine for 12 h at ambient temperature in order to functionalize the CNTs tip with thiol groups (Pt/CNT-SH). The second step consists of the substrate dipping in a solution containing citrate stabilized gold nanoparticles for 4 h (Pt/CNTS-AuNP). The obtained sample was rinsed by ethanol, dried with nitrogen flow.

The absorption of gold nanoparticles occurs spontaneously by formation of Au-S bonds. Both the process steps were followed by XPS analysis in order to check the effectiveness of the reactions. The results are reported in figure 4.12.

The spectrum reveals the successful functionalization of the CNTs with gold nanoparticles.

The spectra reveal the presence of the Au 4f doublet at BE 84 and 87.6 assigned to Au^0.

The S2p core line on the other hand shows a predominant signal that refers to free thiol S-H bonds that indicates an incomplete functionalization of the CNTs with gold nanoparticles. This effect could be explained with an inaccessibility of some thiol groups to the gold nanoparticles. In fact, the thiol groups present on the free CNT tips are able to react with the gold nanoparticles, while S-H sites placed on the sidewalls could be masked by the high density of CNTs as shown by the SEM images.

The presence of gold nanoparticles on the CNT surface is confirmed also by contact angle measurement performed before and after the Au NP absorption (figure 4.13). Before dipping the sample in the NP solution, the static contact angle is around 85°. This value is lower than the literature data on CNTs films [12]. The reason of this could be the high concentration of thiol functional groups on the surface. The S-H group is slightly acid (pKa around 10-11), the presence of these groups and the high roughness of the surface can lead to a contact angle value lower respect to the unfunctionalized CNT (normally showing hydrophobic properties). The contact angle of the Pt/CNTS-AuNP sample shows a net decrease of the value to around 16° induced by the presence of the gold nanoparticles on the surface. It is well known that metal nanoparticles in general and gold NP in particular have a high surface energy.

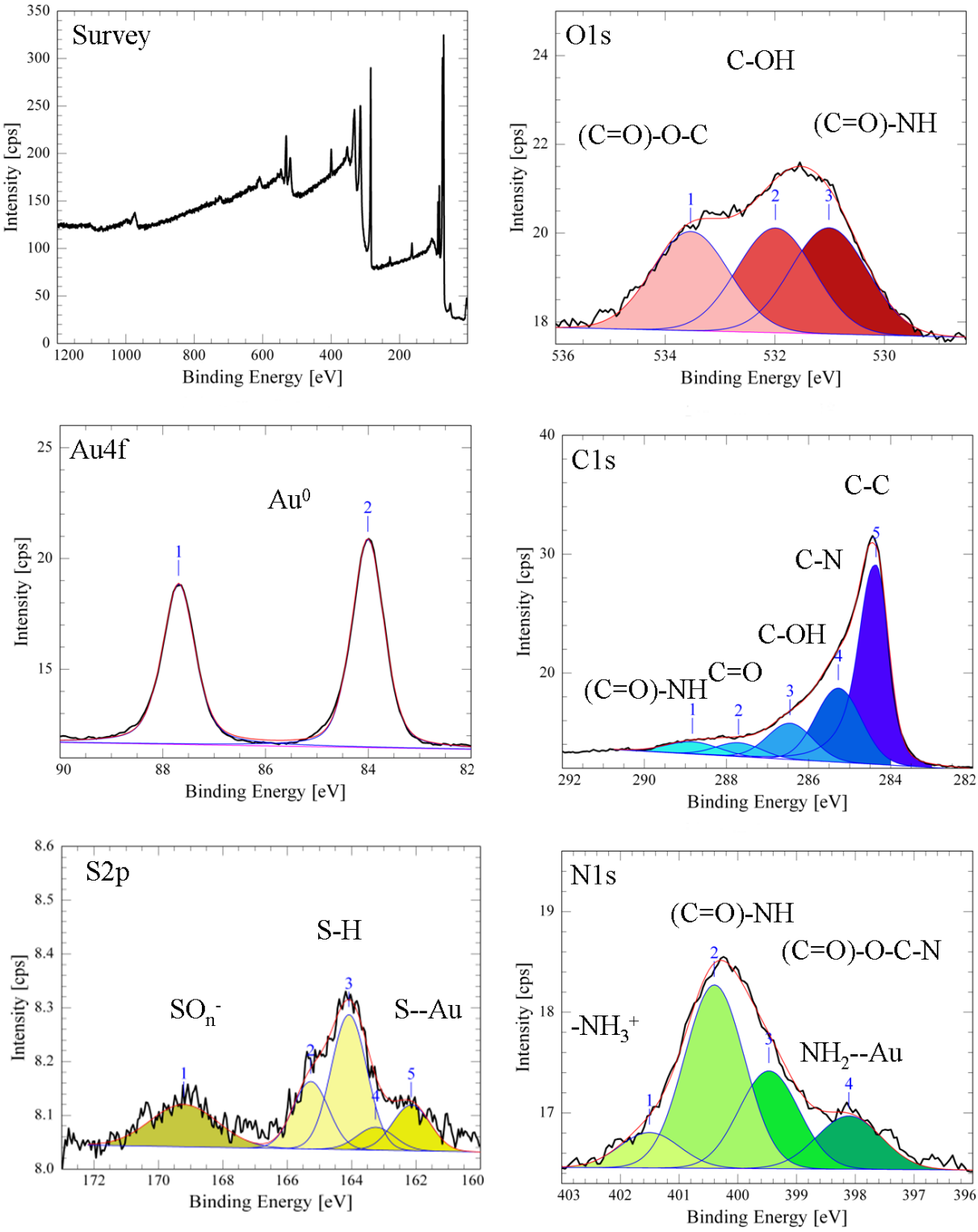

Figure 4.12 *XPS core lines of the Pt-CNTS-AuNP samples after 20 minutes of deposition with 10 V potential: survey, C1s, O1s, S2p, Au 4f and N1s core lines.*

This is attributed to the particular shape and at the unsatured gold atoms present on the cluster surface.

The work of Shultz [13] shows that also a low nanoparticles density on a sample surface can decrease drastically its static contact angle.

Line	BE (eV)	Conc. %	Bond
C1s1	288.63	3.43 %	(C=O)-NH
C1s2	287.64	3.63 %	C=O
C1s3	286.80	9.53 %	C-O-C
C1s4	285.35	19.45 %	C-N,C-S, C-H
C1s5	284.32	40.42 %	C-C
Au4f2	83.98	2.28 %	Au^0
O1s1	533.59	3.94 %	(C=O)-O-C
O1s2	532.34	3.57 %	C-O-C
O1s3	531.68	3.88 %	(C=O)-NH
S2p1	169.12	1.23 %	SO_n
S2p3	164.02	1.80 %	S-H
S2p5	162.14	0.76 %	S-Au
N1s1	401.50	0.68 %	NH_3^+
N1s2	400.40	3.53 %	(C=O)-NH
N1s3	399.47	1.88 %	(C=O)-O-C-N-
N1s4	398.11	1.11 %	NH_2--Au

Table 4.1. *XPS quantitative analysis of the Pt/CNTS-AuNP sample.*

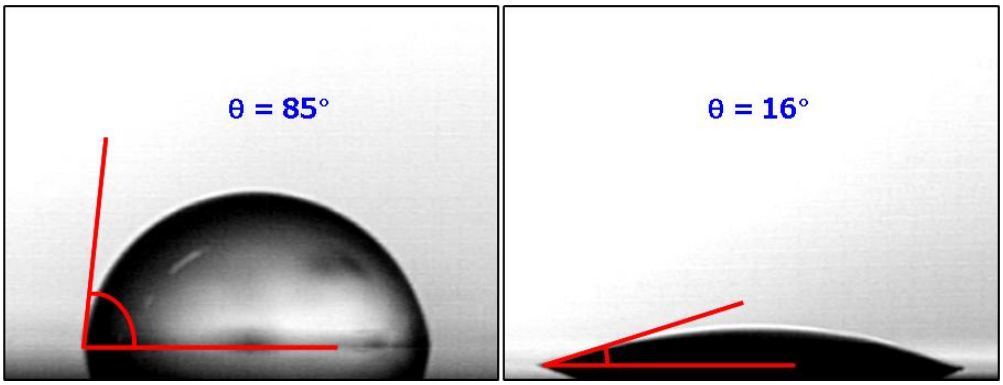

Figure 4.13. *Static contact angles obtained by the Pt/CNTSH (left) and the Pt/CNTS-AuNP (right).*

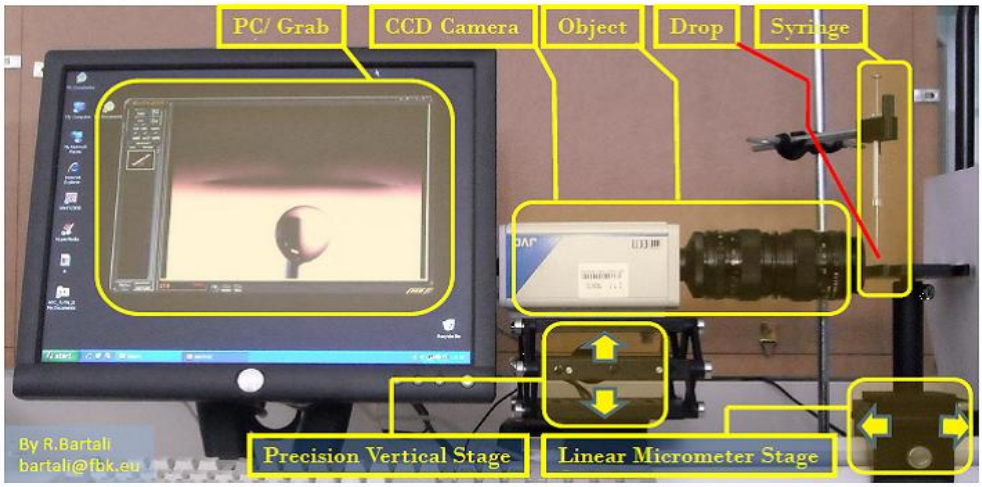

Figure 4.14. *Home-make static contact angle instrument.*

2) *Dipping of the Pt/CNTs system in a solution containing gold nanoparticles modified by cysteamine layer*

The second procedure described in this section is schematized in figure 4.15:

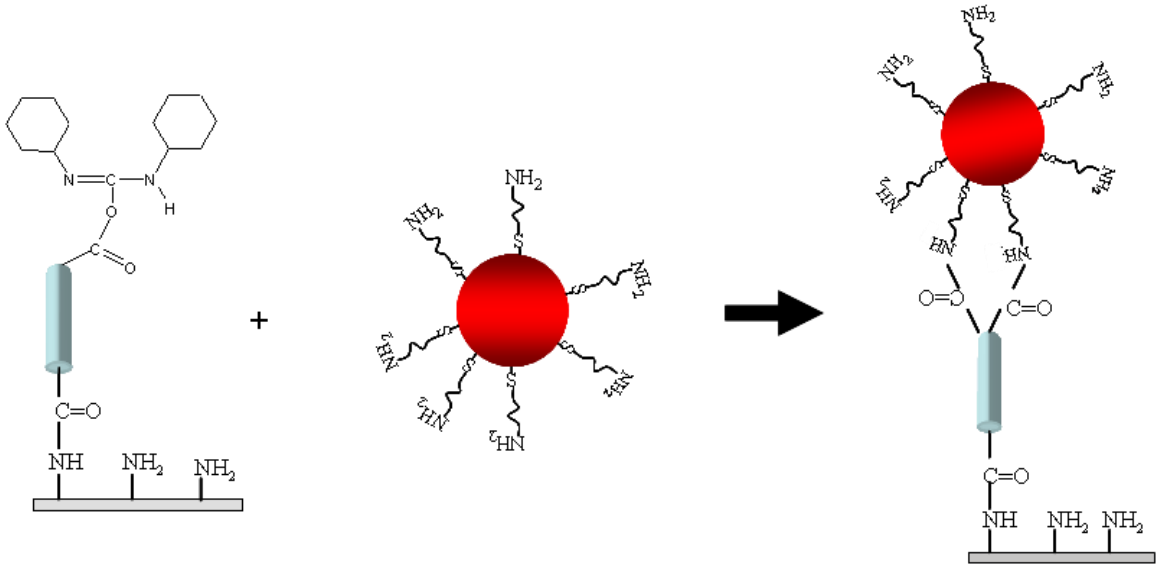

Figure 4.15. *Scheme of the reaction between Pt/CNT surface and the cysteamine-capped gold nanoparticles.*

In this procedure, the electrodeposited CNT films were immersed in a solution containing gold nanoparticles stabilized by cysteamine molecules in DMF.

In figure 4.16 the XPS spectrum of the Pt/CNTS-AuNP(cys) is reported as well as the quantitative analysis on Table 4.2. Each core line appears to be well structured and allows to unambiguously identify the chemical bonds present on the CNT surface. The C1s core line present a high intensity component at around 285.2 eV associated to the CH_2-S and CH_2-N bonds and to the contribution of the cysteamine molecules on the gold NP surface. Also the peaks at higher BE are characterized a high intensity probably due to the presence of oxidized compounds. The S2p core line is fitted with three doublets: that at higher BE is associated to the free thiol, the intermediate is associated to the S-Au bonds and the last is associated to a high degree of coordination gold as reported by Wired et al. (labelled S=Au) [8]. Because of the weakness of the platinum signal we can asses that the S2p core line refer only to the cysteamine layer on the gold nanoparticles that probably masks the signal coming from the carbon nanotube film. This is an indication of a high coverage of gold nanoparticles on the CNT film. This is confirmed by the scanning tunnel microscope analysis (STM) performed on the sample (figure 4.17).

Line	**BE(eV)**	**Conc. %**	**Bond**
C1s1	288.76	8.95 %	CONH
C1s2	286.80	11.74 %	C-O-C
C1s3	285.35	15.00 %	C-N,C-S,
C1s4	284.32	16.53 %	C-C
Au4f1-3	84.66	0.11 %	Au-S
Au4f2-4	83.90	3.32 %	Au^0
O1s1	536.13	5.75 %	H_2O
O1s2	533.59	7.94 %	(C=O)-OC
O1s3	532.34	9.57 %	C-O-C
O1s4	531.68	8.88 %	(C=O)-NH
S2p2	163.51	0.96 %	S-H
S2p5	162.18	1.30 %	S-Au
S2p6	161.14	1.16 %	S=Au
N1s1	400.87	1.69 %	NH_2
N1s2	399.61	2.84 %	(C=O)-NH
N1s2	399.61	2.84 %	NH_2--Au

Table 4.2. *XPS quantitative analysis of the Pt/CNTS-AuNP(cys) sample.*

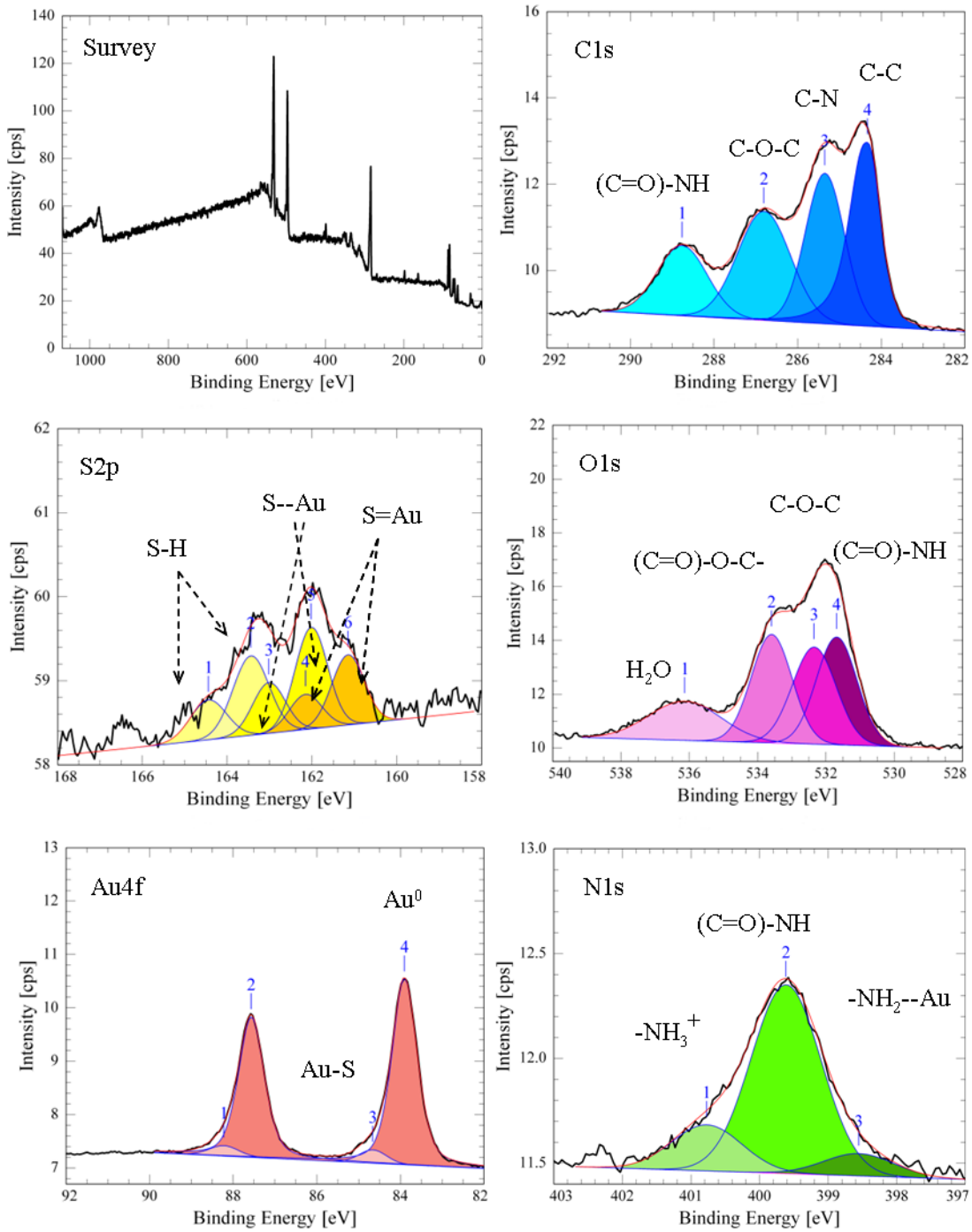

Figure 4.16. *XPS core lines of the Pt/CNTS-AuNP(cys) samples: survey, C1s, O1s , S2, Au 4f and N1s core lines.*

The STM images show that a dense film of gold nanoparticles is formed on the sample (figure 4.17). The nanoparticles appears aggregated but with single domains. In figure 4.18 the section analysis and the calculated size distribution obtained by the STM analysis are reported.

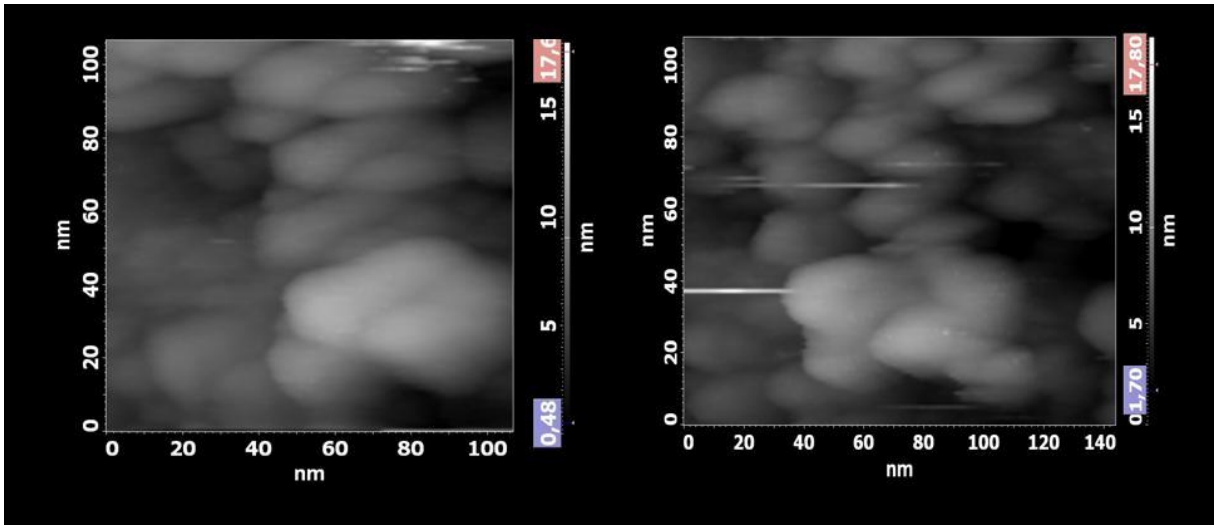

Figure 4.17. *Scanning tunnel microscopy analysis on Pt/CNTS-AuNP(cys) sample.*

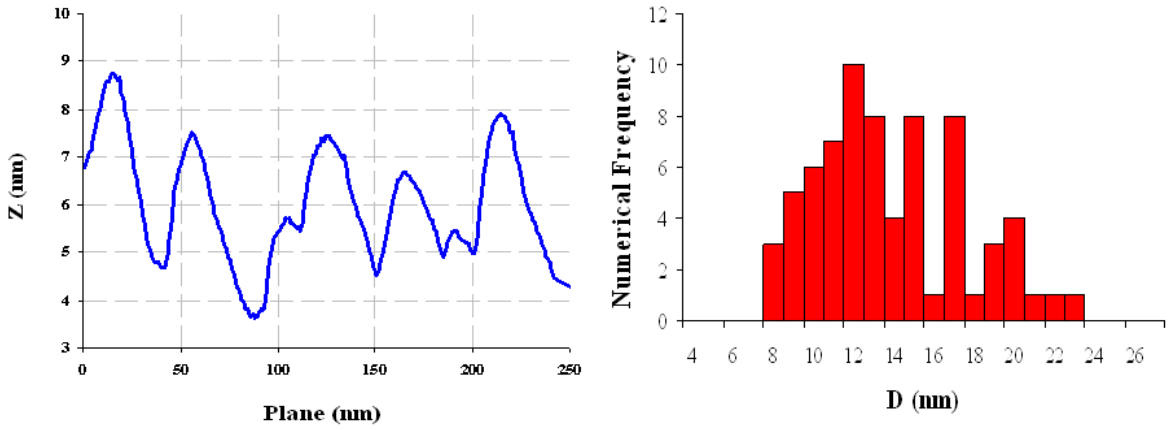

Figure 4.18. *Vertical section analysis* ***(left)*** *and size distribution calculation* ***(right)*** *obtained from the scanning tunnel microscopy analysis on Pt/CNTS-AuNP(cys) sample.*

The Pt/CNTS-AuNP(cys) sample was analyzed by means of static contact angle technique in order to investigate its hydrophilic/hydrophobic character. The results are presented in figure 4.19.

On the left the static contact angles images of the Pt/CNT sample (without the gold nanoparticles) are presented.

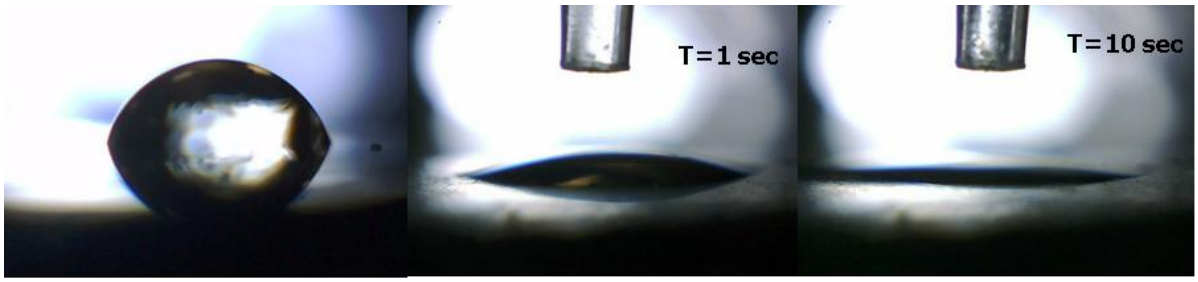

Figure 4.19. *Static contact angle acquired on the carbon nanotubes carpets* ***(left)*** *and on the Pt/CNTS-AuNP(cys) sample (****center and right****).*

Initially the value of the meniscus angle is 68.3°. The measurement performed on the Pt/CNTS-AuNP(cys) sample shows a drastic decrease of the contact angle. The angle measured 1 second after the drop is placed in the sample surface is around 10°, while after 10 seconds the meniscus angle lowers below 5°, confirming the extremely high hydrofilicity of the surface induced by the gold nanoparticles.

4.2 Raman analysis of low concentration ions solutions

Because of its particular morphology we test the performances of the Pt/CNTS-AuNP(cys) as substrates for Raman spectroscopy. Works presented in literature put in evidence that Ag and Au aggregates are excellent candidates as substrates for Surface Enhanced Raman Scattering (SERS) [14]. In particular, our samples are very stable during time, thanks to the chemical bonding of the gold nanoparticles on the CNTs. this allows the immobilization of the AuNP films on the substrate. Moreover the Au NPs functionalized with aminic groups can bind charged molecules allowing a close contact with the analytes. This is a favourable situation because close contact between gold nanoparticles and the molecules are required for SERS experiments. Another advantage of this system is the possibility to detach the analytes from the surface by changing the solution pH. This enables a recycling of the same support for next analyses.

4.2.1 Introduction to analysis of ions concentration using Raman spectroscopy

An important issue having great social impact is the definition of standards regarding the potable water quality. Almost all natural waters contain chloride and sulphate ions. Their concentrations vary considerably according to the local concentration of minerals of the earth. Low to moderate concentrations of both chloride and sulphate ions add palatability to water. In fact, they are desirable for this reason. Excessive concentrations of both, of course, can make water unpleasant to drink. Moreover, in high concentrations they can cause serious problems. Sulphates can be more unsafe because they generally are present in greater concentrations. Health concerns regarding sulphate in drinking water have been raised because it is reported that diarrhea may be associated with the ingestion of water containing high levels of sulphate.

Apart from natural source, one of the most important sources of sulphate ions is the human pollution. One of the main sources is the industry emission of solphorose anhydride from sulphur derivates combustion The principal cause of acid rain is sulphur and nitrogen compounds from human activities, such as electricity generation, factories, and motor vehicles. Apart from this also other toxics anions like chromate perchlorate cyanide etc can seriously damage the ecosystems being extremely dangerous for humans. Perchlorate has

been used as the oxidizer component and primary ingredient in solid propellant for rockets and missiles. A number of technologies, including ion chromatography [15], ion-selective electrodes [16], capillary electrophoresis [17], and IC–mass spectrometry [18], have been used to detect perchlorate and other toxic ions.

Currently, ion chromatography is the most commonly used technique for routine analysis and screening of ions in environmental samples because of its relatively low detection limit and its relatively low cost. For rapid and long term monitoring, however, it is desirable to detect perchlorate ions in situ to minimize sample volume, handling time, and costs. Surface-enhanced Raman scattering (SERS) analysis of ions may allow rapid, sensitive, in situ detection. Portable Raman spectrometer systems coupled with fiber-optic probes are now commercially available; are relatively inexpensive and robust and require only minimal sample preparation and handling.

4.2.3 Results and discussions

We use carbon nanotube carpets grafted with gold nanoparticles covered by cysteamine (sample Pt/CNTS-AuNP(cys)) as active SERS substrates for the detection of sulphate ions at very low concentrations. The particular morphology of the sample composed by gold NP aggregated and the presence of a cysteamine coating allows is of particularly interest for ion detections by SERS.

Cysteamine is widely used to form a self-assembled monolayer on gold and silver surfaces [19]. Protonation of cysteamine terminal amine groups by pH adjustment allows tuning of the surface charge on the cysteamine-modified gold nanoparticles. Previous studies suggest that the p*K*a of the adsorbed cysteamine monolayer should be significantly higher than 7 [20]. In other words, at pH 2, the cysteamine-modified gold nanoparticles should be positively charged due to protonated amine groups.

On the other hand, at a basic pH, these amine groups are expected to be deprotonated. Strong electrostatic attraction between ions and positively charged gold nanoparticle enables close contact with negatively charged ions. In this case, the enhanced Raman scattering (see figure 4.20) is intensified. Sulphate, as well as perchlorate, chromate, and nitrate, are polyatomic and exhibit Raman active vibrational modes.

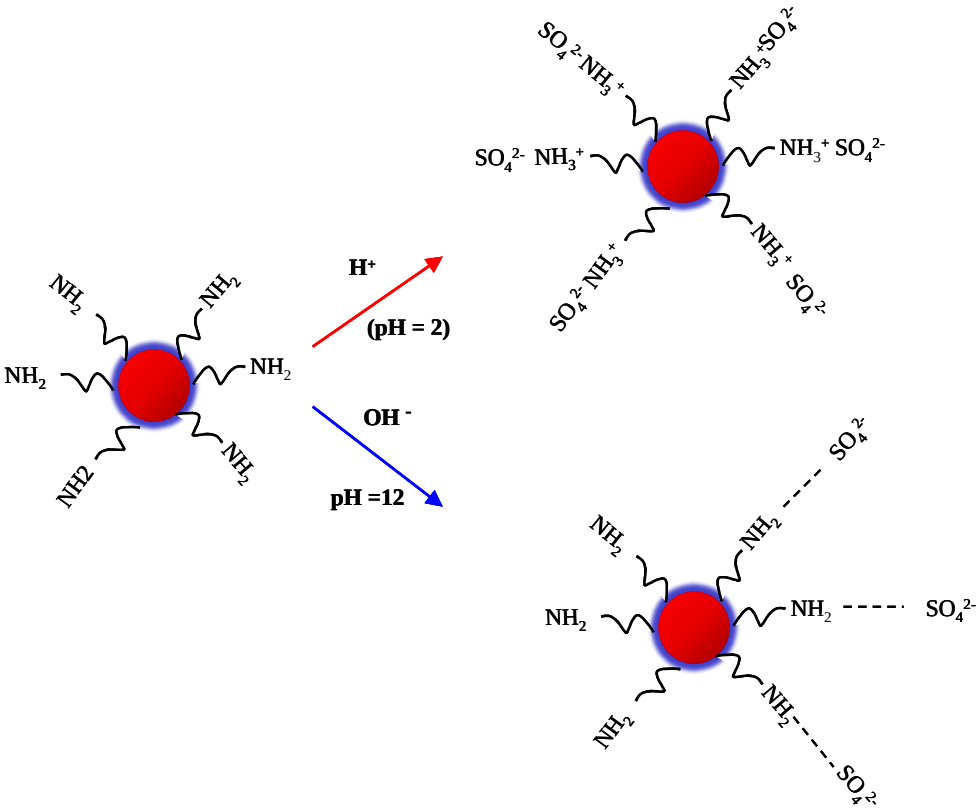

***Figure 4.20**. Sulphate ions adsorption scheme at different pH.*

The most intense mode in these ions is due to the total symmetric stretching vibrations (v1) which are summarized in Table 4.3. Consequently, each of these toxic anions exhibits characteristic Raman emission, which can be used for identification purposes.

Anion	Chemical formula	Raman *v*1 mode (cm^{-1})
Sulphate	SO_4^{2-}	985
Nitrate	NO_3^-	1036
Perchlorate	ClO_4^-	934
Chromate	CrO_4^-	847

***Table 4.3.** Principal v1 stretching mode for sulphate, nitrate, perchlorate and chromate ions.*

In a typical procedure, samples are immersed in a in a HCL water solution (pH=2) with different Na_2SO_4 concentrations for 30 min. After the adsorption, the samples are cleaned with fresh water, and then analyzed by Raman spectroscopy. In figure 4.21 Raman analysis in

the region 400-1400 cm^{-1} for sulphate ion adsorbed on pure gold and on the Pt/CNTS-AuNP(cys) sample with two different ions concentration are reported.

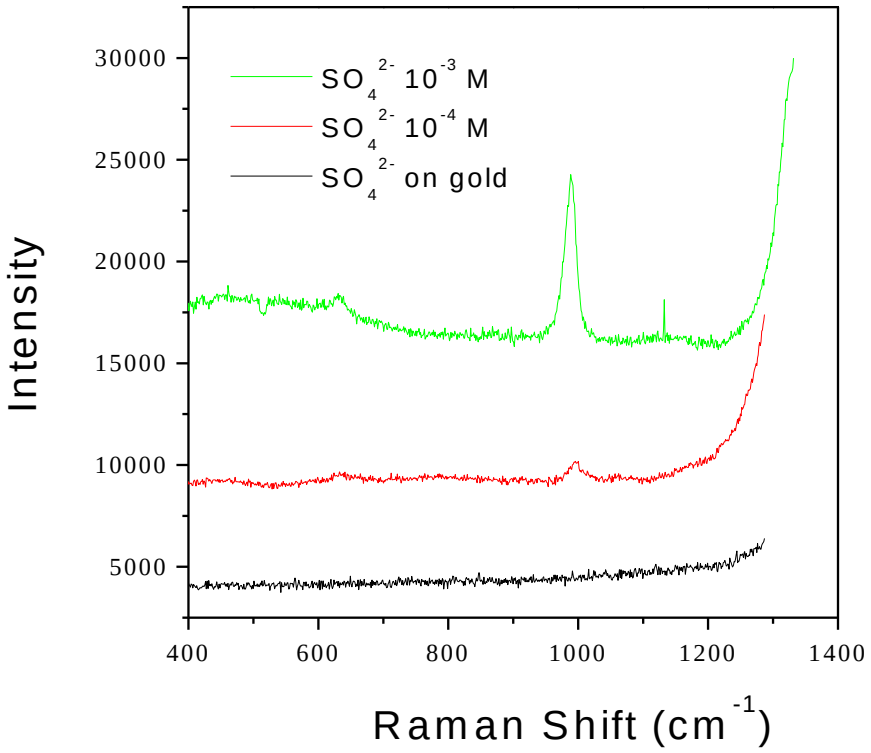

Figure 4.21. *Micro-raman analysis of the v1 stretching mode of SO_4^{2-} ions adsorbed on the cysteamine layer.*

The gold-coated SO_4^{2-} ions does not show any peak as expected. In fact, the lack of cationic functional groups able to capture the sulphate anions inactivates the relative Raman scattering. The Pt/CNTS-AuNP(cys) sample instead shows the presence of a peak at around 931 cm^{-1} assigned to the *v1* stretching mode of the sulphate anion. As shown in the figure 4.21 the 10^{-4} M concentration of SO_4^{2-} are detected by the SERS analysis. Lower concentrations do not lead to significant peaks, while for concentrations higher than 10^{-3} M the 931 cm^{-1} feature dominates the spectra. The high intensity around 1300 cm^{-1} on the right side of the spectra of Pt/CNTS-AuNP(cys) derives from the D component of the CNTs support. In figure 4.22 the Raman spectra of SO_4^{-2} anions absorbed on the Pt/CNTS-AuNP(cys) sample at pH 2 and 12 are reported.

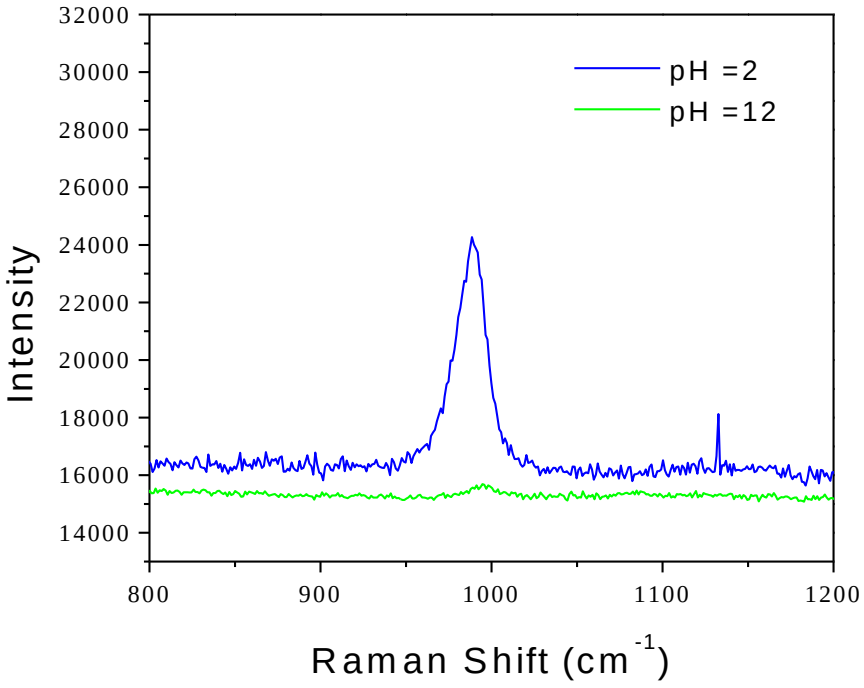

Figure 4.22. *Raman spectra of SO_4^{2-} anions adsorbed at pH 2 and 12.*

As can be seen drastic difference of the 931 cm^{-1} Raman peak intensity is present. This confirms the active role of the protonated amine in attracting the anions near the gold nanoparticles surface as observed also by [21] for perchlorate anions on cysteamine-modified gold nanoparticles. The advantage of this system is related to the possibility to perform multiple analyses using the same substrate by simply washing the sample with a pH 12 water solution after the analysis. Thanks to the high mechanical and chemical stability of the Pt/CNTS-AuNP(cys) sample, derived from the strong chemical bonds between CNT, gold NP and substrate the sensor can be used several times without loosening sensitivity. This open a new way for the synthesis of long reusable SERS sensors to monitor pollutants and toxic ions in water.

4.2.4 References

[1] O. Van der Biest, L.J. Vandeperre *Ann. Rev. Mater. Sci.* **29** (1999) 327.

[2] P. Sarkar, P.S. Nicholson *J. Am. Ceram. Soc.* **79** (1996) 1987.

[3] A. R. Boccaccini, I. Zhitomirsky *Cur. Op. Solid State Mater. Sci.* **6** (2002) 251.

[4] Y.H Li, S.G. Wang, Z.K. Luan, J. Ding, C. L. Xu, D. H. Wu *Carbon* **41** (2003) 1057.

[5] L. P. Zhao, L.Gao *Coll. Surf. A Physicochem. Eng. Asp.* **224** (2003) 127.

[6] D. Kurnosov, A. S. Bugaev, K.N. Nikolski, R. Tchesov, E.Sheshin *Appl. Surf. Sci.* **215** (2003) 232.

[7] B. J. C. Thomas, A. R. Boccaccini, M. S. P Shaffer. *J. Am. Ceram. Soc.* **88** (2005) 980.

[8] M. Wirde, U. Gelius *Langmuir* **15** (1999) 6370.

[9] A. Michota, A. Kudelski, J. Bukowska *Surf. Sci.* **502–503** (2002) 214.

[10] C.M. Pradier, M. Salmain, L. Zheng, G. Jaouen *Surf. Sci.* **502–503** (2002) 193.

[11] X. Nan, Z.Gu, and Z. Iu *J. Coll. Interf. Sci.* **245** (2002) 311.

[12] K. K. S. Lau, J.Bico, K. B. K Teo, M. Chhowalla, G. A. J. Amaratunga. *Nan. Lett.* **3** (2003)1701.

[13] F. Shultz, S. Franzka, G. Smith *Adv. Funct. Mat* **12** (2002) 532.

[14] T. Wadayama, M. Oishi *Surf. Sci.* **600** (2006) 4352.

[15] A. J. Krynitsky, R. A. Niemann, D. A. Nortrup, *Anal. Chem.* **76** (2004) 5518.

[16] M. Shamsipur, A. Soleymanpour, M. Akhond, H. Sharghi, A.R. Hasaninejad, *Sens. Act. B* **89** (2003) 9.

[17] A.V. Pirogov, A.V. Yur'ev, O.A. Shpigun, *J. Anal. Chem.* **58** (2003) 781.

[18] J. Mathew, J. Gandhi, J. Hedrick, *J. Chromatogr. A* **54** (2005) 1085.

[19] M. Tsen, L. Sun, *Anal. Chim. Acta* **307** (1995) 333.

[20] M.A. Bryant, R.M. Crooks, *Langmuir* **3** (1997) 385.

[21] C. Ruan, W. Wang, B. Gu. *Anal. Chim. Act.* **567** (2006) 114.

CHAPTER 5

5.1 Optical properties of carbon nanotubes

5.1.1 Introduction

The interest of the scientific community about carbon nanotubes/nanoparticles hybrid materials in the last years has been increasing [1, 2, 3, 4]. The possibility of exploit the synergetic effect between the constitutive elements properties in a same final product has triggered intensive study toward this field. In particular, fluorescent carbon nanotubes based composite have recently attracted much attention for applications in biological field like hypodermic in vivo imaging for cancer diagnosis [5, 6].

Moreover, CNTs are becoming serious candidate as drug carriers thanks to the possibility to fill the hollow part with cancer treatment drugs [7]. The design of such materials requires complex nanostructures that have an intense emissions, appropriate storage geometries and appropriate functionality. Recently, much attention has been paid to the fabrication of nano-hybrids of Au nanoparticles and carbon nanotubes (CNT) in order to enhance the performance as building blocks, and to explore the exceptional properties of hybrids based on CNT for potential applications in catalysts, biosensors, optics etc [8, 9, 10].

Although CNT are known to be luminescent in the visible the intensities are generally too weak for *in vivo* imaging or other photonic applications, moreover the investigation of the mechanism underling this effect is still nowadays incomplete. On the other hand, increase of the fluorescence was observed to be induced by proper functionalization [11]. There are experimental evidences that visible luminescence in carbon nanotubes arise from the presence of defective-sites acting as excitation trap sites [12]. These defects can be introduced on the surface of CNTs by acid treatment and appropriate passivation with the aid of appropriates functional groups. In this chapter CNT/gold nanoparticles hybrids were obtained by covalent functionalization of CNTs with thiol groups with successive adsorption of gold nanoparticles on the CNTs surface. The CNTS/Au composite shows a very strong luminescence in the yellow range of the visible region. The drastic increase of the CNT luminescence in our CNTS/Au hybrids is explained with an electromagnetic enhanced emission stimulated by the gold nanoparticles. This hybrid material could be a promising candidate for *in vivo* imaging

system thanks to its high luminescence yield, easy synthesis route and lower toxicity respect to the semiconductor quantum dots based counterparts. Due to their intense luminescence, functionalized CNT-based systems can be of significant interest also for applications in photonics such as the production of lasers, colour display and waveguides in the visible. The optical efficiency of the hybrid materials is comparable with that of semiconductor nanocrystals

5.1.2 Results and discussions

In figure 5.1A and 5.1B are reported the photoluminescence (PL) spectra of acid treated carbon nanotubes (CNT-COOH), thiol-functionalized CNTs (CNTS), thiol functionalized carbon nanotubes/Gold nanoparticles composite (CNTS/Au1 and 2) samples and the ethanol sample reference, obtained with 531.5 nm excitation.

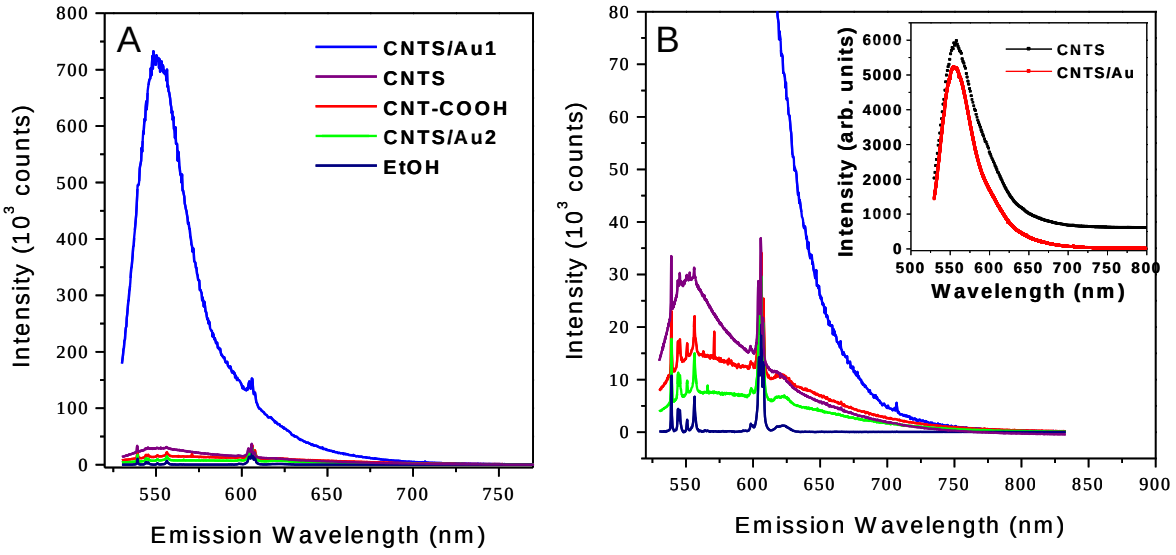

Figure 5.1 (A). *Photoluminescence spectra of thiol functionalized carbon nanotubes (CNTS) and thiol functionalized carbon nanotubes/gold nanoparticles (CNTS/Au) composite. The spectra were obtained with 531.5 nm Ar excitation laser.* ***(B)*** *High magnification showing the CNTs luminescence signals.* ***Insert:*** *PL signal for the CNTS and CNTS/Au samples normalized to the same height: the ethanol Raman contribution is subtracted.*

The spectra of CNTS/Au1 sample show a luminescence emission of about 35 times higher with respect to the virgin and functionalized CNTS samples. The CNTS/Au2 sample (with

higher concentration of gold nanoparticles) shows a little decrease of the emission with respect to the thiol functionalized carbon nanotubes and the acid treated. The PL lineshapes, of the CNTS/Au1 and CNTS samples, normalized to the same height and subtracted by the Raman ethanol contribution are shown in the insert of figure 5.1B. The two spectra appear very similar between them. In addition, the lineshapes and positions mirror those of the PL spectra of functionalized CNT reported in literature [13] as well as those of the carbon dots produced by Sun et al. [14]. In these recent works visible luminescence emission was observed by polymer passivated carbon nanotubes and nanoparticles treated in acid conditions. The oxidative acid treatment seems to be the key process in the production of fluorescent carbon materials. The oxidative treatment effects are: a) decrease of the carbon nanotube length; b) functionalization with carboxylic and oxydrilic bonds that allows solubilisation of the carbon nanotubes; c) creation of defective states in the electronic structure of the CNT. This last point plays a fundamental role in the visible luminescence properties. One of the principal characteristic of the defect luminescence is the excitation wavelength dependence of the luminescence indicating a wide distribution of emitters [12]. On the contrary, the excitation spectrum of the CNTS/Au1 sample reported in figure 5.2A shows a maximum of the luminescence emission at around 530 nm.

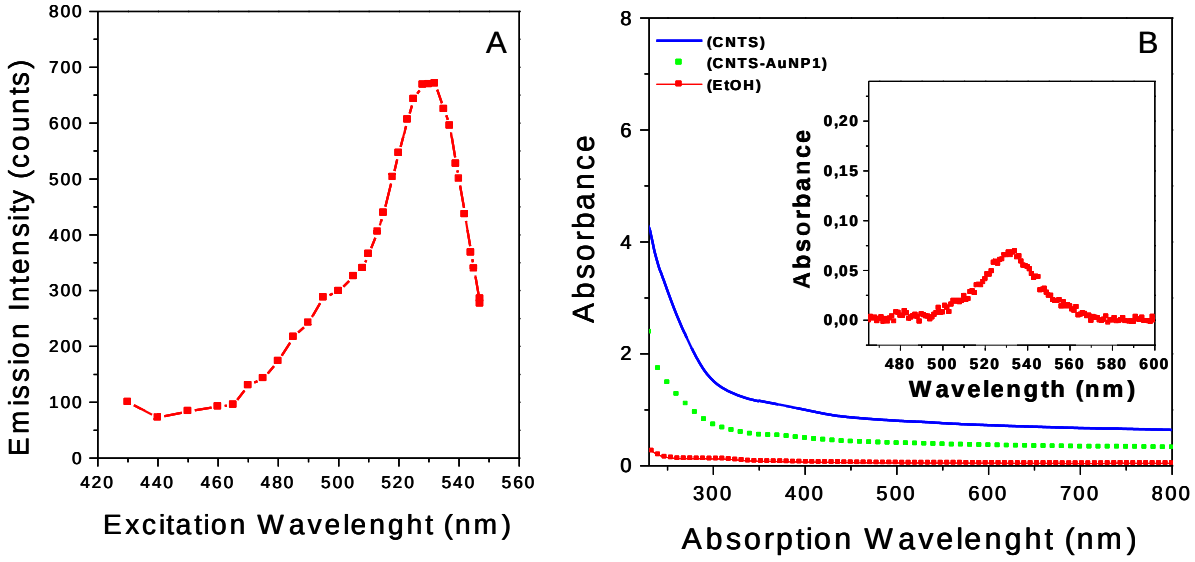

Figure 5.2(A). *Excitation spectra of CNTS/Au suspension. The luminescence emission was keep fixed at 551nm.* ***(B)*** *Absorption spectra of diluted CNTS/Au, CNTS and ethanol.* ***Insert:*** *high magnification of the region between 460-620 nm of the CNTS/Au1 sample spectrum showing the surface plasmon resonance of the gold nanoparticles.*

The visible absorption spectrum of the CNTS/Au1 sample shows the presence of a very weak absorption peak at around 530 nm (figure 5.2B insert) that is assigned to the Surface Plasmon Resonance (SPR) of gold nanoparticles. The position and line width of the peak are similar to the diluted solution of gold nanoparticles, indicating the presence of isolated nanoparticles linked to the CNTs.

The transmission electron microscopy images presented in figure 5.3A and B confirm the presence of short carbon nanotubes (100-200 nm length) with gold nanoparticles placed near the tip (5.3A and 5.3B).

The energy dispersive X-ray spectroscopy (figure 5.3C) reveals the presence of carbon oxygen and gold as expected. High magnification images of CNT (figure 5.3D) show the presence of black spots that are assigned to defects induced by the acid treatments.

In figure 5.4 images of the CNTS and CNTS/Au luminescence are reported. Figure 5.4A shows the CNT suspension after the precipitation of the CNTs. The precipitate is clearly visible on the bottom of the bottle, while the solution appears colorless.

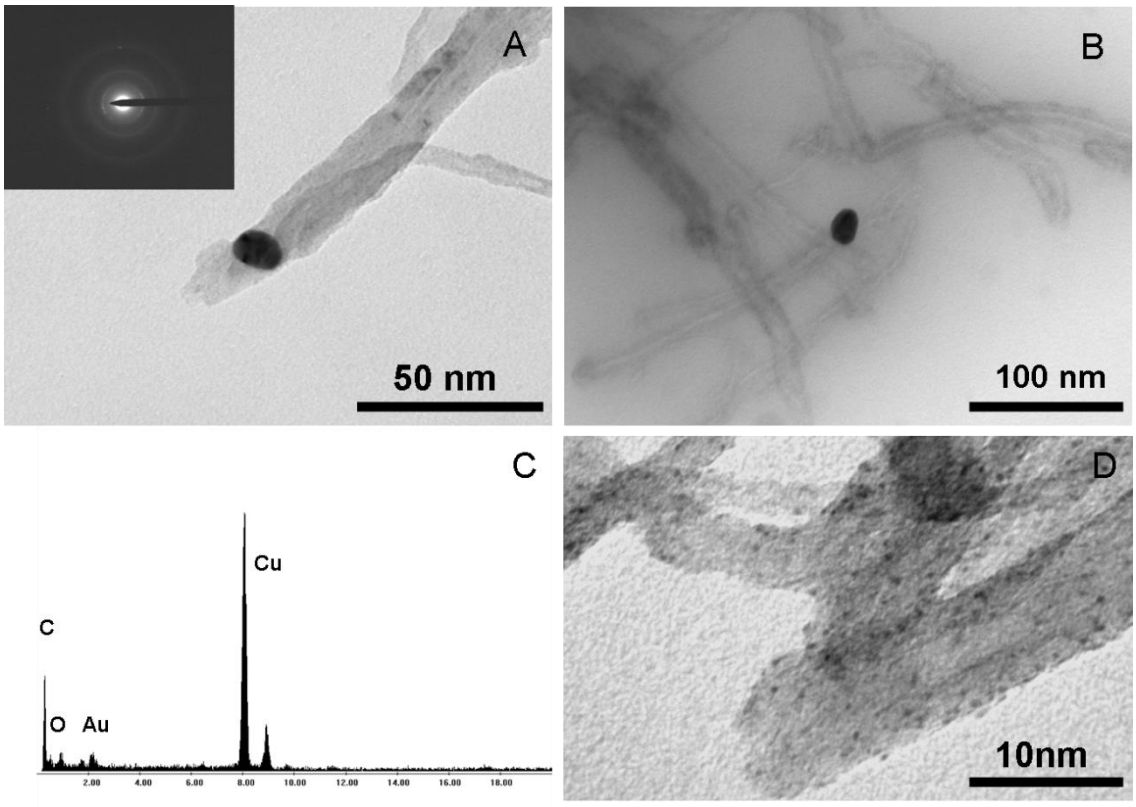

Figure 5.3. *Transmission electron microscopy images of CNTS/Au sample deposited on copper grid.* ***A*** *and* ***B:*** *carbon nanotubes with gold nanoparticles on the tip.* ***C:*** *EDXS analysis of the region A.* ***D:*** *high magnification image showing the CNT defects.*

The luminescence of this CNTS suspension is shown in figure 5.4B. Figure 5.4C and 5.4D show the intense yellow emission from the CNTS/Au1 sample. It appears to be very strong and uniform around all the solution. The presence of the black precipitate on the bottom of the sample does not interfere with the emission process. The experimental results may be explained with an energy transfer process occurring between the gold nanoparticles to the carbon nanotubes. This effect was observed in literature for metal nanoparticles/dye molecules [15,16]. In brief, the resonance between the conduction electrons of the metal nanoparticles and the incident light leads to the formation of a high frequency electromagnetic field around the nanoparticles.

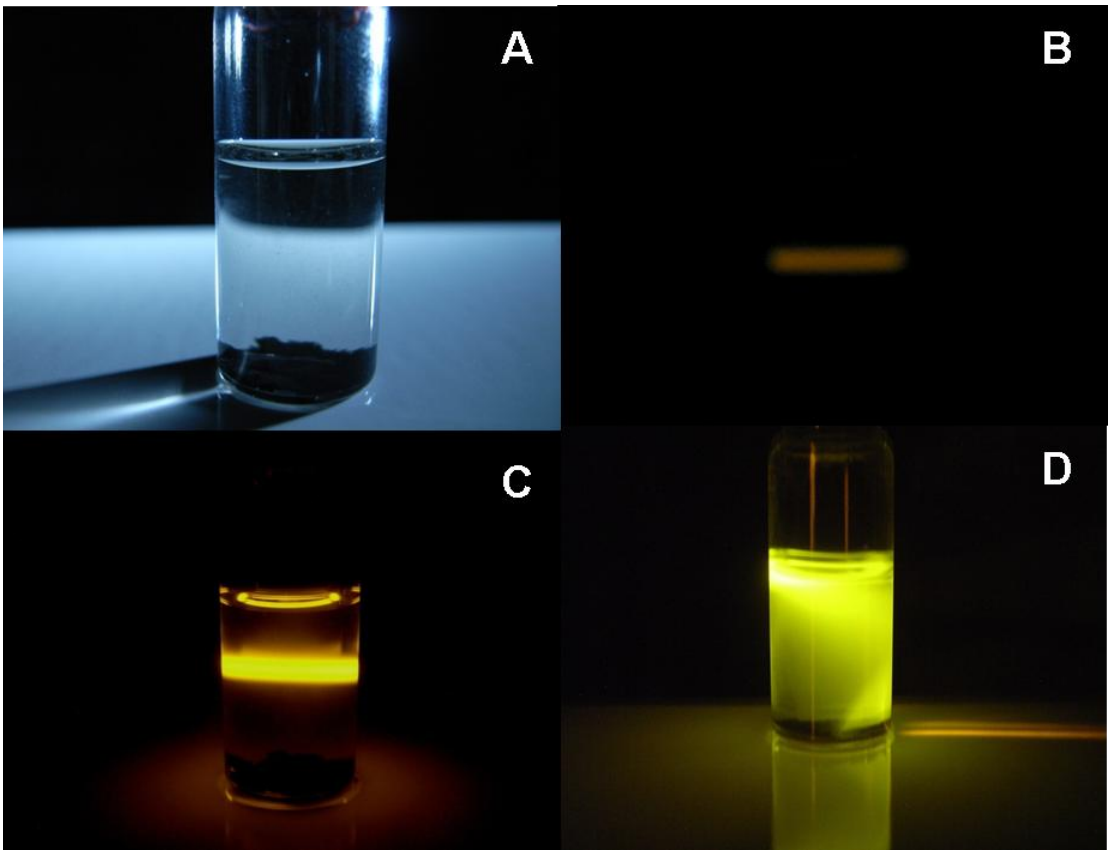

Figure 5.4. *Images of the CNTs luminescence:* ***A:*** *CNTS/Au solution: the precipitate is clearly visible on the bottom of the flask.* ***B:*** *image obtained on the CNTS sample with a 5 mW green (532 nm) pointer.* ***C****: image obtained on the CNTS/Au sample with a 5 mW green (532 nm) pointer.* ***D:*** *image obtained on the CNTS/Au sample with a uniform green light at 532 nm.*

The presence of nearby electromagnetic field arising from the surface plasmon resonance of the metal nanoparticles influences the oscillating dipole strength modifying the rate of

emission and the spatial distribution of the radiated energy. When a fluorophore is placed in the vicinity of the nanoparticles surface an increase of the excitation and emission rate of the emitting centre [17] can be obtained.

Works published in literature put in evidences the effect of the distance between the metal surface and the fluorescent centres [18, 19]. Contrary to Surface Enhanced Raman Scattering that requires close contact of the studied molecules with the metallic surface, at distance below 2 nm, there is reasonable agreement that, for the surface enhanced fluorescence the maximal enhancements occur about at distances of some nm from the metal surface. For lower distances, the fluorescence of molecules is significantly quenched, primarily by energy transfer to the metal surface.

In our situation the defects are homogenously dispersed on the CNT surface, allowing the energy transfer from the gold nanoparticles to the emitting centre.

In conclusion, the carbon nanotubes/gold nanoparticle composite shows a high luminescence in the visible region. This effect is explained with an electromagnetic energy transfer mediated by the surface plasmon resonance of the gold nanoparticles.

These materials are excellent candidate as drugs carriers in cancer therapy, thanks to the intrinsic high luminescence that enables to detect the CNT diffusion in the tumour vascular system. In addition, they are highly water-soluble, biocompatible, and do not suffer from photobleaching nor blinking. The excitation wavelength of 530 nm are less energetic and much less dangerous respect to the usually UV-exciting light normally used for the quantum dots based imaging. Finally, these systems are expected to present lower toxicity with respect to the quantum dots-based systems and higher stability in the human body with respect to the organic dyes based counterparts.

5.1.3 References

[1] T. Sainsbury, J. Stolarczyk, D. Fitzmaurica, *J. Phys Chem B* **109** (2005) 16310.

[2] B. Xue, P. Chen, Q. Hong, J. Lin and K.L. Tan *J. Mater. Chem*. **11** (2001) 2378.

[3] B. M. Quinn, C. Dekker, S. G. Lemay, *J. Am. Chem. Soc*. **127** (2005) 6146.

[4] J. Qu, Y. Shen, X. Qu, S. Dong, *Chem. Comm*. **34** (2004) 13.

[5] D. L. Shi, Y. Guo, Z. Y.Dong, J. Lian, W. Wang, G. K. Liu, L. M. Wang, R. C. Ewing, *Adv. Mater.* **19 (**2007) 4033.

[6] Z. Liu, W. Cai, L. He, N. Nakayama, K. Chen, X. Sun, X. Chen, H. Dai *Nat. Nanotech.* **2** (2007) 47.

[7] Y. Guo, D. Shi, H. Cho, Z. Dong, A. Kulkarni, G. M. Pauletti, W. Wang, Jie L., W. Liu, L. Ren, Q. Zhang, G. Liu, C. Huth, L. Wang, R. C. Ew . *Adv. Funct. Mater.* **18** (2008) 1.

[8] S. H. Lim, J. Wei J. Lin, *Chem. Phys. Lett.* **400** (2004) 578.

[9] N.Alexeyeva, T. Laaksonen, K. Kontturi, F. Mirkhalaf, D.J. Schiffrin, K. Tammeveski, *Electrochem. Comm.* **8** (2006) 1475.

[10] R. Zhou, M. Shi, X. Chen, M. Wang, Y. Yang, X. Zhang, H. Chen, *Nanotech.* **18** (2007) 485603.

[11] Y. Lin, B. Zhou, R.B. Martin, K. B. Henbest, B. A. Harruff, J. E. Riggs, Z. X. Guo, L. F. Allard, Y. P. Sun *J. Phys Chem B.* **109** (2005) 14779.

[12] J. E. Riggs, Z. Guo, D. L. Carroll, Y.P. Sun, *J. Am. Chem. Soc.* **122** (2000) 5879.

[13] Y. Lin, B. Zhou, R. B. Martin, K. B. Henbest, B. A. Harruff, J. E. Riggs, Z.-X. Guo, L. F. Allard, and Y.-P. Sun *J. Phys. Chem. B* **109** (2005) 14779.

[14] S. T. Yang, L. Cao, P. G. Luo, F. Lu, X. Wang, H. Wang, M. J. Meziani, Y.Liu, G. Qi Y.-P. Sun *J. Am. Chem. Soc.* **131** (2009) 11308.

[15] A. M Glass, P. F. Liao, J. G. Bergman, D. H. Olson *Opt. Letts.* **5** (1980) 368.

[16] A. Campion, A. R. Gallo, C. B. Harris, H. J. Robota, P. M. Whitmore, *Chem. Phys. Letts.* **73** (1980) 447.

[17].J. R. Lakowich *Anal. Biochem.* **298** (2001) 1.

[18] W. L. Barnes, *J. Mod. Opt.* **45** (1998) 661.

[19] R. M. Amos, W. L. Barnes, *Phys. Rev. B* **55** (1997) 7249.

CHAPTER 6

6.1 X-ray photoelectron spectroscopy studies on gold metal nanoclusters/amorphous carbon composite

In this chapter, the characterizations results on gold nanoclusters embedded in a carbon matrix are presented. These systems are of particular importance as standards for the characterizations of the gold nanoparticles because of the interactions between the carbon matrix and the gold nanoparticles are negligible. Among the analytical techniques X-ray photoelectron spectroscopy (XPS) is one of the more effective for the study of metal nanoclusters because it can provide both chemical and structural information. In this respect, for small metal nanoparticles (lower than 5 nm diameter) an estimation of the mean dimension is gained analysing the core line binding energy (BE) shift and the valence band narrowing with respect to their bulk counterpart. The advantage of this approach is related to the high sensitivity of the photoelectron spectroscopy to very small clusters.

6.1.1 Introduction

The ever-growing interest in the investigation of noble metal nanoclusters is due to the importance of such systems with respect to the theory of nanomaterials and with respect to several promising applications as well. In particular, the enhanced catalytic activity of supported Au nanoparticles has recently attracted particular attention by scientists in various disciplines, such as surface chemistry, heterogeneous catalysis and fundamental cluster physics [1–4]. It was shown that nanoscale gold particles with a size less than 5 nm display highly selective low temperature catalytic activity. The presence of enhanced catalytic property is linked to the rearrangement of electrons of gold atoms occurring when the long order distribution of the electronic charge in bulk metals approach the nanometric dimensions in clusters. This change in the electronic configuration influences also the X-ray photoemission process.

However, prospects for using systems consisting of supported clusters are restricted in practical applications, because of complex production methods, possible long time instability

and catalytic efficiency based on a single monolayer of clusters. As an alternative to systems made of supported clusters, we have deposited and investigated the catalytic properties of systems made of clusters embedded in a matrix. a-C:Au films are investigated in the present work by core level and valence band (VB) photoemission, and by X-ray diffraction (XRD). We will show how the two techniques complement each other at describing the decrease in Au cluster diameter with decreasing Au concentration in the films. Cluster sizes in the nm range, with just several tens of atoms involved in a single cluster, can definitely be obtained. This is the critical size range, where many analytical techniques loose sensitivity and clusters themselves become highly unstable.

6.1.2 X-ray photoelectron spectroscopy

It is well known that, as the size of metallic clusters is reduced to the nanometre range, their electronic structure changes with respect to bulk and a metal–semiconductor transition eventually occurs. These modifications, extensively described in the literature, can be revealed by probing the material electronic structure via core level and VB photoemission. The resulting spectral changes, well documented not only for Au, but for metal clusters in general [5–8], are illustrated in figure 6.1 and 6.2, where we show the Au 4f and VB photoemission spectra from three a-C:Au samples, identified on the plot by their Au concentration. The spectrum from bulk Au is also given for reference on each figure. Figure 6.1 reveals that the Au 4f lines shift to higher binding energy (BE) and broaden, developing a high BE tail, on moving from bulk Au to a-C:Au films. While this kind of observations could in principle be due to chemical effects, no indication for Au–O or Au–C interaction is found in the O 1s and C 1s spectra, respectively. (In this regard, one should remember that the Au solubility in C is very low, $8.2* 10^{-6}$ at. % [9]). The observed effects must therefore be ‘‘size-induced’’. In such a case, the Au 4f high BE shift, as well as the appearance of the asymmetric tail, is understood as dominantly due to so-called ‘‘final state’’ effects in the photoemission process [5].

In other words, the photohole left behind after photoionization is long lived in small clusters, where screening efficiency is low, so that the associated Coulomb field acts on the outgoing photoelectron by reducing its kinetic energy.

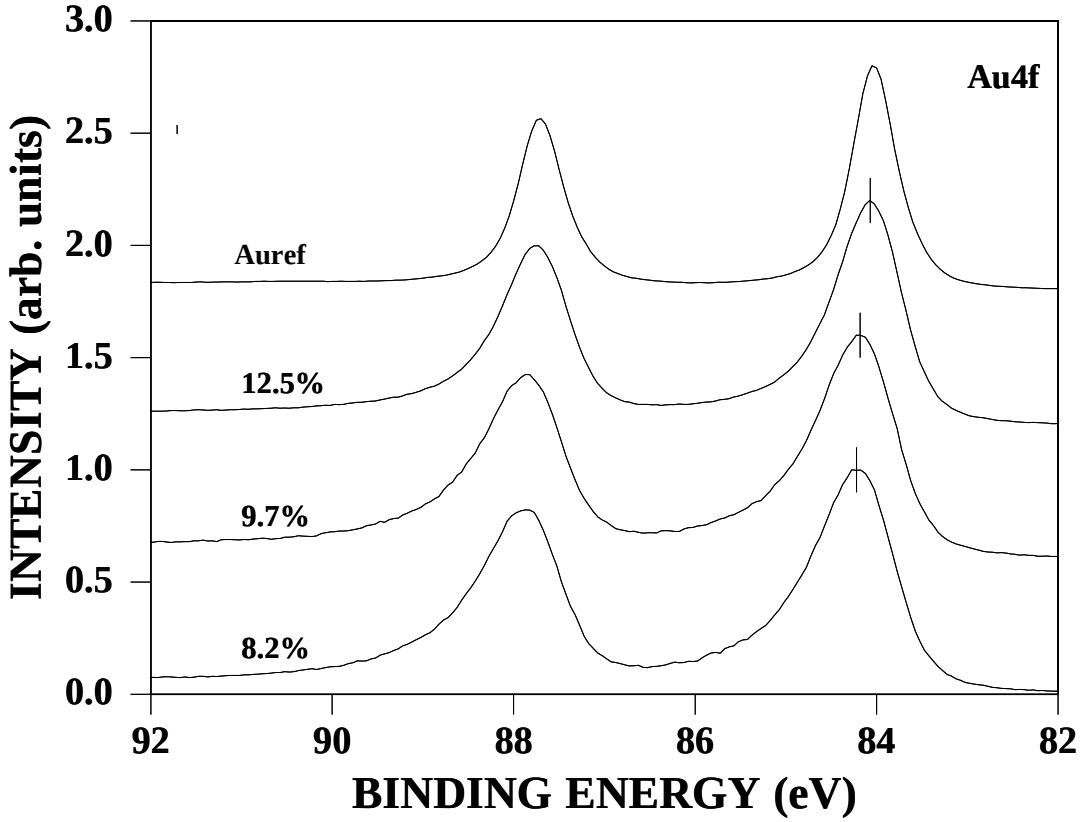

Figure 6.1. *Au 4f photoemission spectra for bulk Au and three a-C:Au samples with Au concentration 12.5 at. %, 9.7 at. %, 8.2 at. %. Energies are referred to the Fermi level.*

The associated BE shift would correspond in this case to the energy required to remove (add) an electron from (on) a spherical capacitor of radius d/2:

$$\Delta E = \frac{1}{4\pi\varepsilon_0\varepsilon}\frac{e^2}{d} \qquad (1)$$

where *e* is the electron charge, ε_0 is the vacuum dielectric function and ε is the dielectric function of the medium surrounding the clusters. The development of a high binding energy tail is understood along the same line, by admitting the existence of a cluster size distribution within the samples, whereby smaller clusters contribute to the high BE tail whereas bigger clusters contribute to the region around the peak maximum. In fact, since XPS intensity is proportional to the number of atoms within its probing depth (and not to the number of clusters), we would expect the highest XPS intensity be associated with big clusters and less intensity (in the high BE tail) to be associated with clusters of smaller size.

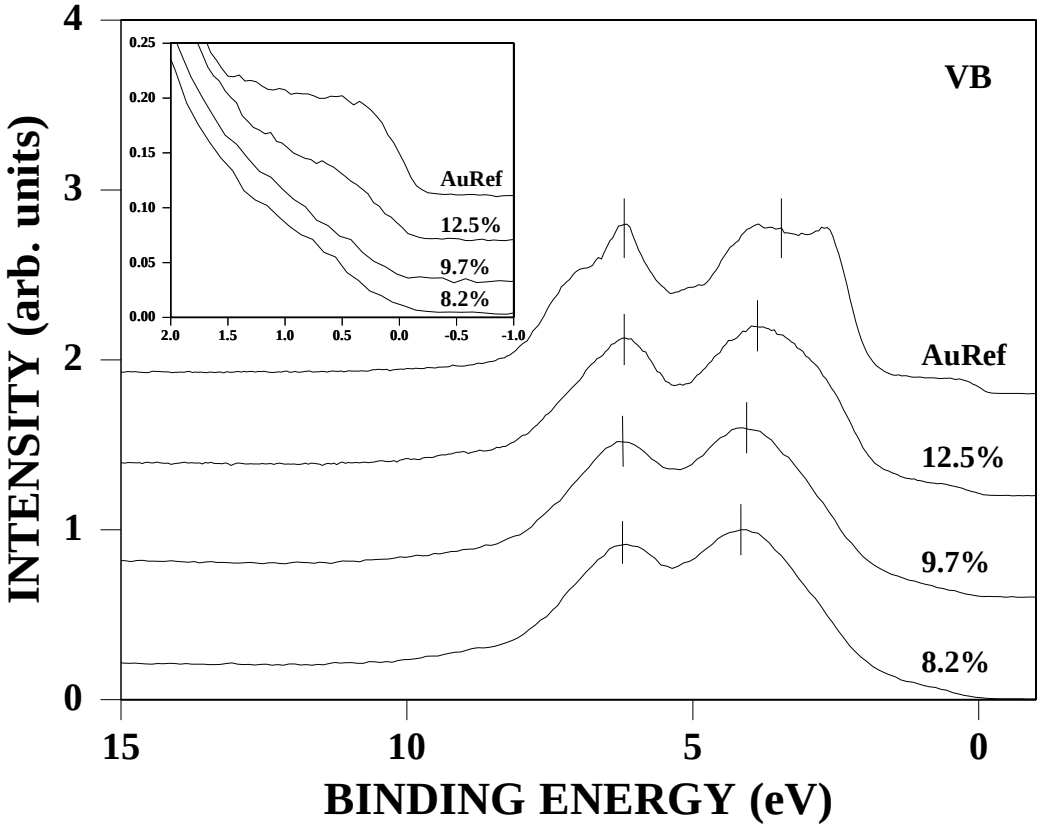

Figure 6.2. *VB photoemission spectra for bulk Au and three a-C:Au samples with Au concentration 12.5 at. %, 9.7 at. %, 8.2 at. %. Energies are referred to the Fermi level. The region near the Fermi level is enlarged in the inset.*

Figure 6.3 shows the evolution of all the above mentioned spectral features (Au $4f_{7/2}$ BE and FWHM, 5d splitting and slope α of the spectrum leading edge at E_F) as a function of the relative Au concentration in the films. At an Au concentration of 38 at.%, all parameters, except possibly α, are still at the level of bulk Au, while they all deviate for Au concentrations lower than 15 at.%, which should be around the percolation threshold (for example, ≈19 at.% is reported to be the percolation limit in an ideal fcc lattice [10]).

The deviation increases with decreasing Au concentration. Since spectral changes are observed in XPS only for clusters in the nanometer range, we conclude that, provided the Au concentration does not exceed 15 at.%, nanosized Au clusters are formed within the films, their maximum size decreasing with decreasing Au content.

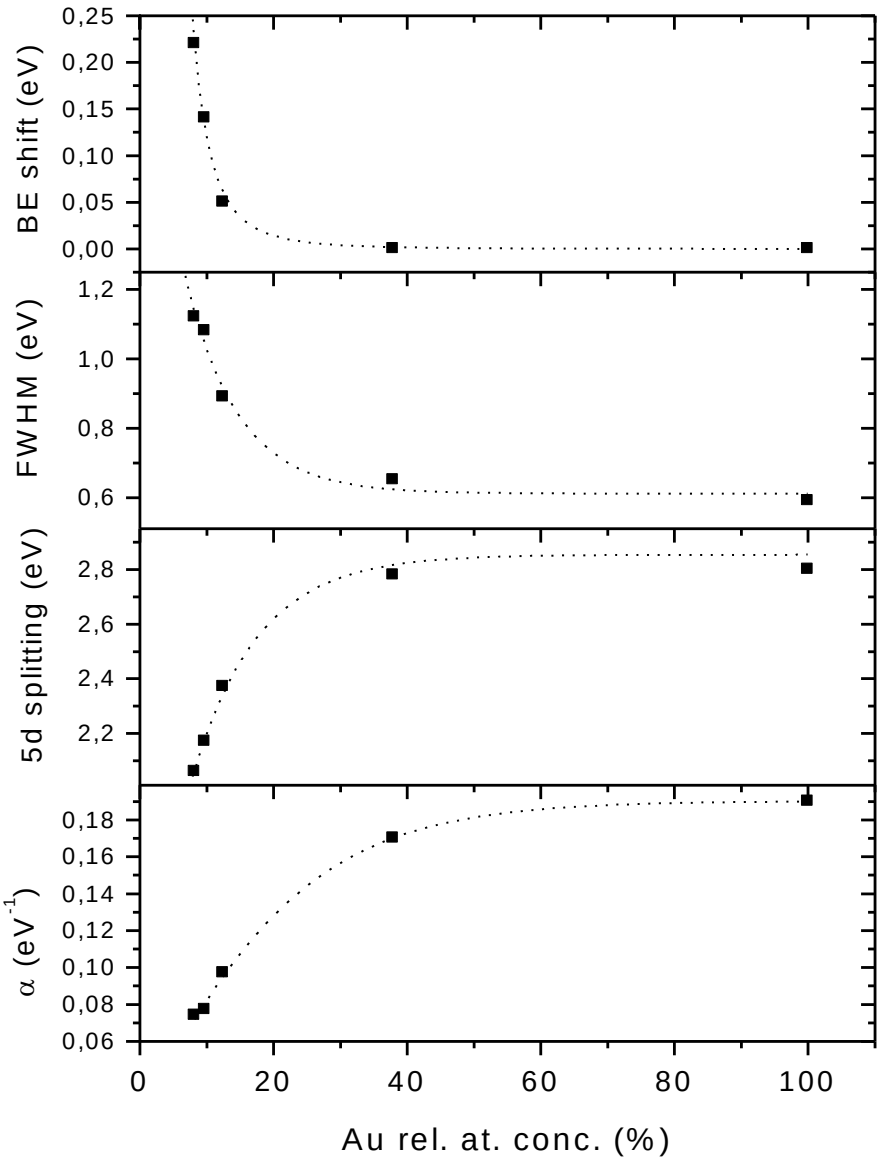

Figure 6.3. *Au $4f_{7/2}$ BE, Au $4f_{7/2}$ FWHM, 5d splitting and spectrum slope at the Fermi edge, α, as a function of the relative Au concentration in a-C:Au films. Lines are drawn to guide the eyes.*

6.1.3. XRD results

Au nanoclusters in a carbon matrix have random orientations and could be treated, from the X-ray point of view, as a nanopowder sample for which the total scattering intensity is an incoherent sum of intensities from individual nanoclusters. In this case the total scattering intensity per nanocluster is given by the Debye equation [11]:

$$I(q) = \sum_j \sum_i f_j f_i \frac{\sin qr_{ij}}{qr_{ij}} \qquad (2)$$

where the sums are taken over all atoms in the nanocluster, q is the momentum transfer, f_i is the form factor of the i-th atom, and r_{ij} is the interatomic distance.

XRD θ-2θ measurements at grazing incidence geometry are shown on figure 6.4, panel A for two a-C:Au films, with 8 at. % and 38 at. % Au concentration respectively. For the lower concentration film, we see a wide Au halo, but no individual diffraction peaks. The asymmetry of the background is associated with unadjusted silicon (111) peak from the Si substrate. The absence of (111) and (200) Au reflexes indicates a very small size of the nanoclusters, as will be shown below. No diffraction peak is seen from carbon, mainly due to the small carbon scattering intensity compared to the Au one. The relative intensity is in fact the square of the ratio of C and Au atomic numbers: $\left(\frac{6}{79}\right)^2 = 0.006$.

In contrast, Au related diffraction peaks are observed for the higher concentration film where, from the Scherrer equation, a cluster diameter around 6-7 nm is estimated.

Figure 6.4, panel B, shows simulated X-Ray Diffraction curves, calculated, according to equation (1), for 4 Au cubic clusters containing, respectively, 1, 2^3, 3^3 and 4^3 FCC unit cells (the Au form factors were taken from the Lawrence Livermore National Laboratory X-ray data base)[12]. The structure and spacing (a=4.08Å) of bulk gold was assumed for the calculation. These four clusters contain 14, 63, 172 and 365 atoms, respectively, and their size, taken as the cube diagonal, is 0.7, 1.4, 2.1 and 2.8 nm respectively.

While for clusters containing 1 and 8 unit cells, no individual diffraction peaks are observed, (111) and (200) reflexes are resolved for clusters of 64 and even of 27 unit cells. Experimental data thus indicate that, for the lower concentration film, Au clusters consist of

only several unit cells but not of several tens of them, and that the cluster size has to be less than 2 nm, in agreement with XPS results.

One should note however that the above estimations are qualitative, because stable nanoclusters with magic numbers 13, 55, 147 and 309 have a different crystal structure from Au metal. Our estimates are confirmed nonetheless by experimental data showing that, for nanoclusters of several tens of unit cells (>1.6 nm), the (111) and (200) reflexes are resolved [13].

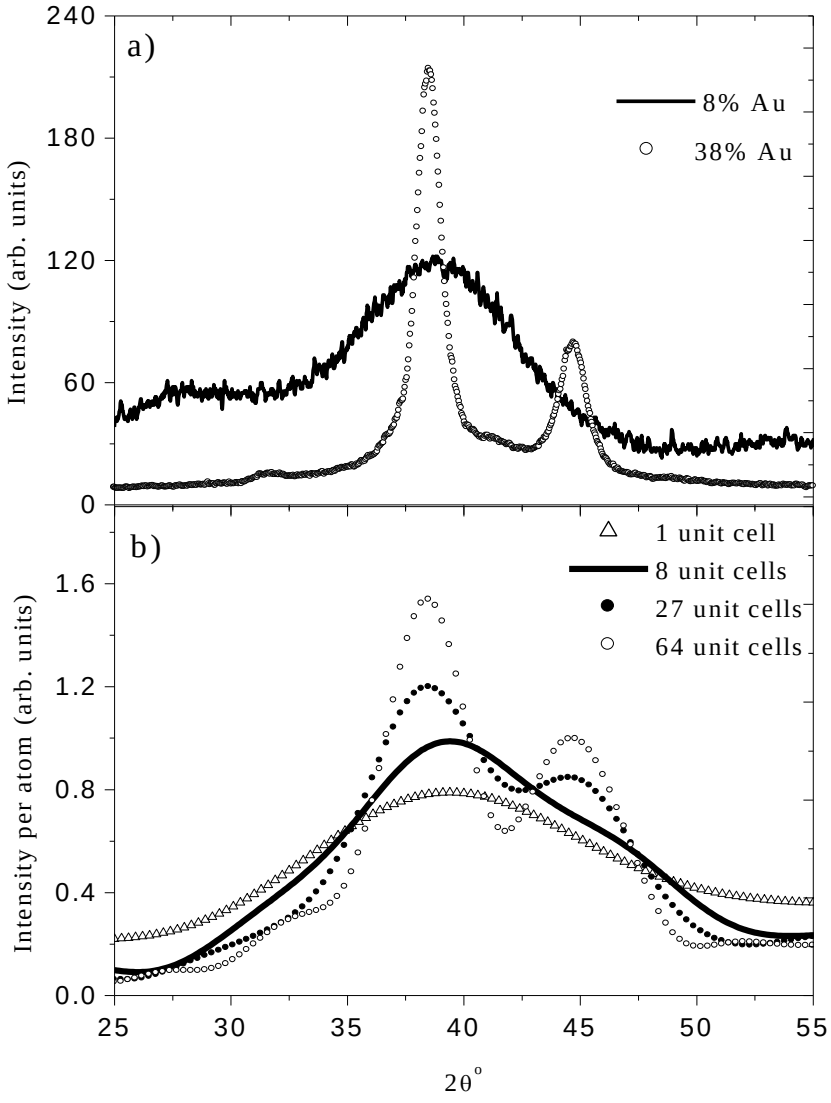

Figure 6.4. *θ-2θ XRD curves:* ***(A)*** *experimental curves for the a-C:Au samples with the lowest and highest Au concentration.* ***(B)*** *simulated curves for 1, 8, 27 and 64 Au unit cells.*

6.1.4 Discussion

According to XRD, Au nanoclusters with diameter around 6-7 nm are formed within films whose Au atomic concentration is 38 %, whereas Au nanoclusters of size less than 2 nm are formed when the Au concentration is below ≈15%, i.e. below the percolation threshold. No difference is observed however in XRD patterns among the three films in such low concentration range. According to XPS on the contrary, clusters formed in films with a gold content of 38 at. % are seen as bulk material and no information is derived about their size. However, as the Au concentration decreases below the percolation limit, photoemission spectra reveal the formation of nanosized Au clusters and they also single out differences among different films.

By measuring different features on photoemission spectra, we see that they deviate from Au bulk values at different Au concentrations (figure 6.3). One reason for this could be in the above mentioned complex interplay between initial and final state effects in different spectral regions.

Strictly speaking, the spectrum slope α at the Fermi edge can only reveal the metal-to-insulator transition, known to occur between 1.4 and 1.2 nm for Au clusters [6]. Other parameters (5d splitting and $4f_{7/2}$ BE shift) are best suited to follow the cluster size evolution as a function of Au content over a wide range. The cluster size derived from 5d splitting is below 2 nm for the three "low concentration" films, in agreement with XRD results. On the contrary, from the Au $4f_{7/2}$ BE shift a cluster size of 7.8 nm is obtained for the 12 % Au film, which clearly contradicts XRD data. In fact, a well-defined XRD pattern should be observed for such a cluster size.

There are several reasons one could consider to explain why core level BE shifts apparently fail at measuring cluster dimensions in this case. Determining the cluster size from core level BE shifts requires knowing the dielectric constant of the medium surrounding the clusters. The "average graphite dielectric constant" we have assumed could not properly describe the a-C matrix: a higher than assumed dielectric constant would lead to a smaller cluster diameter. In addition, the measured BE shift is quite small. The highest shift (film with 8% Au) is 0.22 eV. For comparison, the highest deviation from bulk value in the 5d splitting is 0.74 eV for the same film. Clearly, the uncertainty in cluster diameter associated with very small BE shifts is very high.

What we can state from the above is that XRD and XPS are complementary techniques with respect to cluster size characterization. The former is best suited for measuring cluster sizes above ≈2 nm, while the second is effective for clusters sizes below ≈2 nm. For XPS, core level and VB spectra have both been considered in this respect. For the smallest cluster size, all measurements are consistent. However, as the cluster size increases, measurements based on core level shifts progressively diverge, possibly because of the interplay among a large number of factors in determining BE shifts.

6.2 Calculation of the gold nanoparticles size distribution by XPS: a new tool for nanomaterial characterization

In this section a different approach in the characterization of small metal nanoclusters in amorphous carbon network is presented. From an accurate analysis of the Au 4f core line and valence band, combined with a simple mathematic relation between the binding energy shift and the mean dimensions of the nanoparticles information about the size distribution of the metal nanoparticles were obtained. This new approach could be useful to understand the difference in the calculated mean nanoparticles sizes from VB and core line analysis as well as that obtained from different analytic techniques.

6.2.1 XPS analysis

In figure 6.5 we report the Au 4f core line of the gold reference and of the CAu 1 (8.2 Au at. %) and CAu 2 (9.7 Au at. %) samples. As seen in figure 6.1 there are marked differences among the Au 4f doublets relative to the three samples. In particular the peaks of the two a-C/Au samples are characterized by a higher full width at half maximum (FWHM) and a pronounced asymmetry.

These differences reflect the presence of a population of NP with certain size dispersion. As introduced in the previous paragraph, the relation between peak BE and cluster dimensions depends on various factors like the nature of the metal and of supports as well as the shape and dimensions of the particles [14]. Supported metal nanoparticles can be considered as small spherical capacitors, which are charged by photoelectron emission [12]. From this viewpoint, the BE shift follows the $e^2/\varepsilon_r\varepsilon_0 D$ law, where ε_r is the dielectric constant of the

surrounding medium [15]. However this is a too raw simplification because it does not account for the initial state effect leading to a bad portrayal of the experimental data and of the BE shifts. We solved this problem collecting from literature a set of BE values correspondent to populations of monodispersed NP with known dimensions [6, 7, 16].

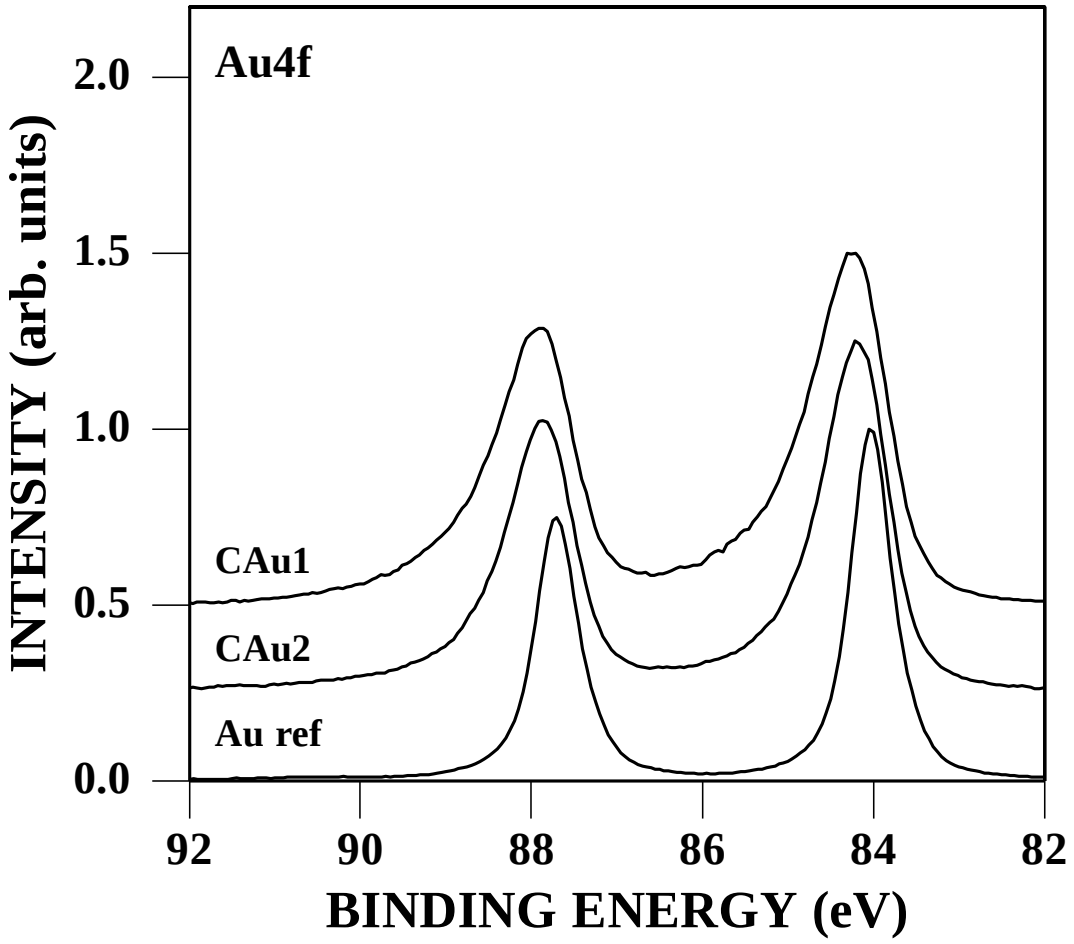

Figure 6.5. *Au 4f spectra of the bulk Au sample as well as the CAu 2 and CAu 1 samples after Shirley background subtraction. The intensity of the lines is normalized to a common value.*

This is a crucial point since it determinates the accuracy in estimating the BE as a function of the NP size. The set of data were fitted using the following function:

$$BE(D) = BE_b + k_1 * e^{(k_2 * (D)^{k_3})} \qquad (3)$$

where D represents the NP diameter. We note that equation 3 was not derived on the basis of physical assumptions but was selected among those that better represent the experimental data.

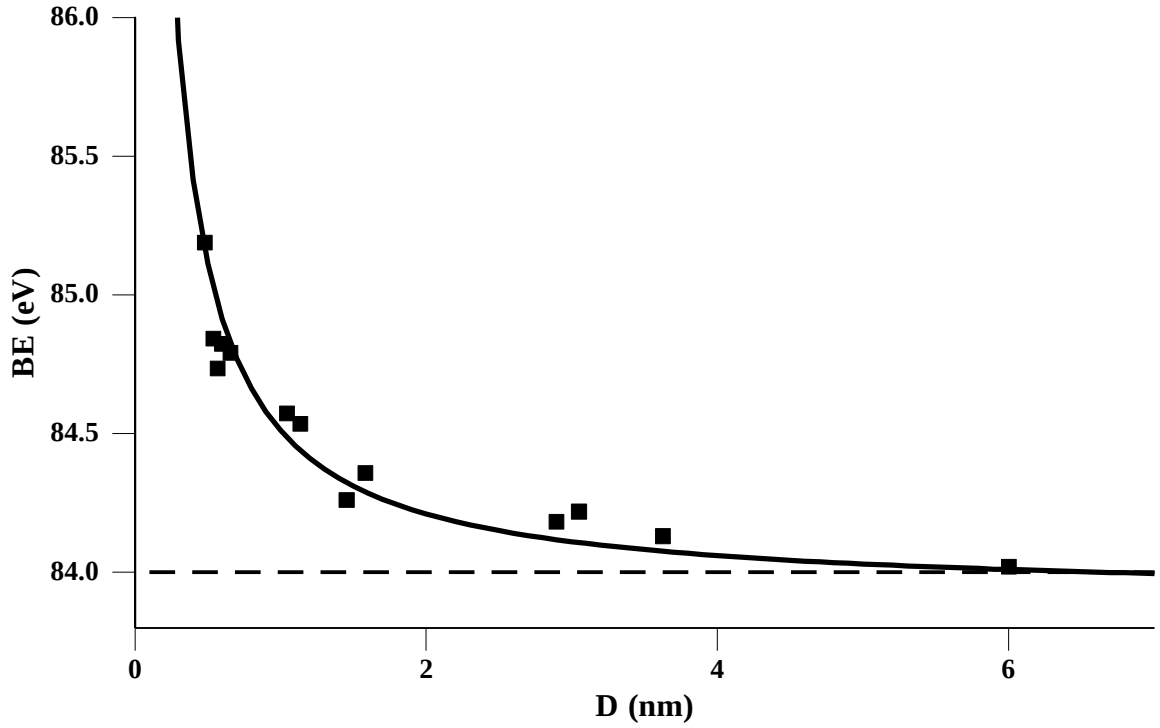

Figure 6.6. *Plot of the Au 4f BE as a function the nanoparticles diameter. Full square: gold clusters deposited on substrate obtained from reference. Continuous line represents the fit function described by the relation (3). The dashed line represents the BE value of the bulk gold sample.*

The quality of the results is shown in figure 6.6 where the BE (D) obtained from eq. (3) is plotted together with the set of data from literature, correspondent to populations of monodispersed NP with known dimensions.

We observe that for $D \geq 6$nm where the effects of confinement disappear, the BE (D) correctly flattens around the position of the Au 4f relative to bulk gold (BE_b) as observed in the XP spectra allowing us to use this function to estimate the NP distributions. Such a kind of gold NP population can be described by a lognormal distribution of sizes which was already used to successfully describe TEM results [17]. In the case of XPS, the spectral intensity is proportional to the number of irradiated atoms i.e. to the diameter D. To account for this effect, we introduce the term $\xi(D)$ that describes the instrumental response as a function of the

nanoparticles dimension. To work out an expression for ξ(D), we consider first the contribution of a single NP section parallel to the sample surface which is proportional to the section area. We then integrate this contribution over all the NP sections along z, the direction orthogonal to the sample surface.

If the NP is embedded in a supporting matrix, we have to consider the exponential decay of the spectral intensity caused by the scattering of the photoelectrons moving toward the surface. This is why XPS is a surface sensitive technique [18]. The resultant expression for ξ(D) is:

$$\xi(D) = K * \int_{0}^{180} \pi (D/2 \sin\theta)^2 e^{[(D/2*(1-\cos\theta)/\lambda]} d\theta \qquad (4)$$

which depends on the mean free path λ of the metals, the K constant encloses all the parameter that influenced the XPS intensity as the photoelectric cross section, the detector efficiency etc. Considering a lognormal distribution of NP sizes we may write the XPS intensity as I(D;μ,σ):

$$I(D;\mu,\sigma) = \frac{e^{-(\ln(D)-\mu)^2/(2\sigma^2)}}{\sigma D\sqrt{2\pi}} * \xi(D) \qquad (5)$$

where μ and σ are the lognormal distribution mean and the variance respectively. Finally using eq. (3) we may obtain the intensity I as a function of the BE. I(BE;μ,σ) shows a great asymmetry due to the spread of the clusters dimensions. To describe the experimental data we must add the spectral broadening due to the natural line width of the core line and the instrumental resolution. This was performed convoluting I(BE;μ,σ) with a Voigt function. This lineshape was selected because it correctly reproduces the Au 4f core line of the bulk gold reference. Then the fitting function used to reproduce the experimental spectra is:

$$g(BE;\mu,\sigma) = I(BE;\mu,\sigma) \otimes V(BE;\max,W,M,\alpha) \qquad (6)$$

M, which represents the Lorenzian-Gaussian fraction and the peak width W, as well as μ and σ were let free to change in the fitting program. Despite what found for many metals, the pure gold Au 4f shows a very low asymmetry α. Because the asymmetry depends on both the DOS at the Fermi level and the core hole potential screening [19] which decrease with the scaling of the particle size, the α value was initially set to zero in the iterative process. The results of the calculation for the a-C/Au samples are shown in Figure 6.7A and 6.8A. The dashed line represents the photoelectron yield I(BE; μ, σ) while the solid lines corresponding to the function g(BE; μ, σ), points out the effect of the Voigt broadening. Comparing g(BE; μ, σ) with the dotted line, which is the experimental spectrum, it is possible to appreciate the fit goodness. The figure 6.7B and 6.8B, show the lognormal distribution corresponding to the two samples both peaked at NP size < 2 nm.

These distributions may explain the pronounced asymmetry of the Au 4f core lines of samples CAu 1 and CAu 2. In fact, a high number of clusters of small dimensions are present in these samples. The smaller their size the lower is their photoelectron yield but higher is the BE shift of their spectral contribution respect to the bulk gold Au 4f. On the contrary, the lognormal distribution indicates that there is a small number of big (> 4nm) NPs which is heavily compensated by the higher number of atoms composing the NPs. The correspondent BE shift of their spectral contribution respect to the bulk gold Au 4f goes to zero with increasing the NP dimension. The average particle size corresponding to the two samples are 1.65nm and 2.29 nm for the two samples CAu 1 (8.2% Au) and CAu 2 sample (9.7 % Au) respectively.

These results are in agreement with that obtained by Gampp et al. concerning plasma-assisted chemical vapour deposition of a-C:H /Au [20]. Those authors measured by TEM a mean NP size of ≈ 2nm in a sample containing 11.5% of gold. In this work we demonstrate the possibility to recover information concerning the size distribution of gold NPs in plasma deposited a-C/Au samples using XPS. This technique is particularly suitable for the characterization of NP with dimensions lower than 5nm. Because the effects of quantum confinement increase with decreasing the NP size, XPS is particularly suitable for the characterization of NP with dimensions lower than 1nm. This is of particular interest because in this region other analytical techniques such as TEM lose their sensitivity. Moreover, analysing a macroscopic area, XPS provides reliable information concerning a wide population of NP and their size distribution.

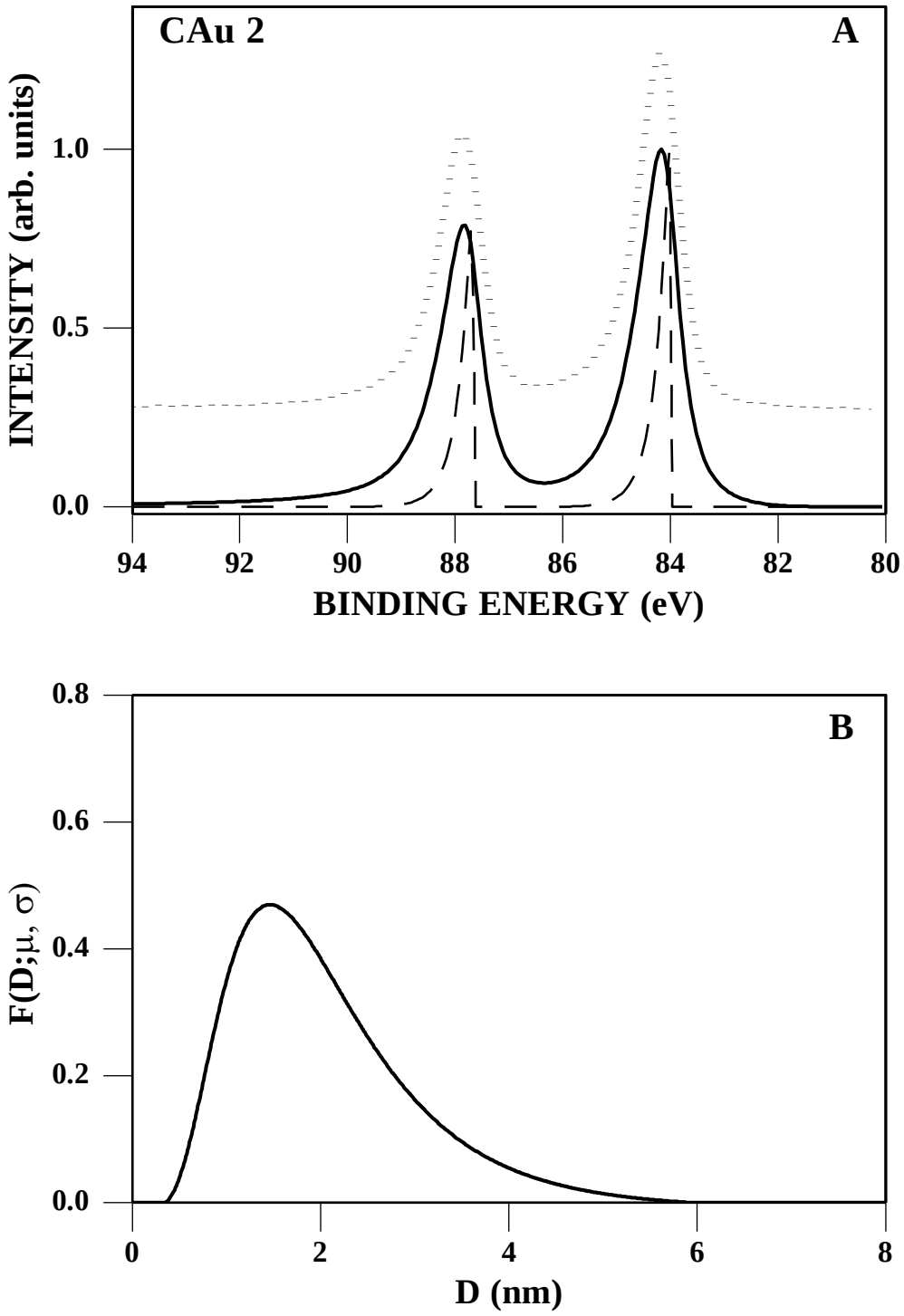

Figure 6.7. *Panel* ***(A)****. Fit of the Au 4f core line of sample CAu 2 after background subtraction. Dashed line: representation of I(BE; μ, σ) function. Solid line: convolution with Voigt broadening. Dotted line: Au 4f of the CAu 2 sample. Panel* ***(B).*** *Size distribution function obtained from the iterative process.*

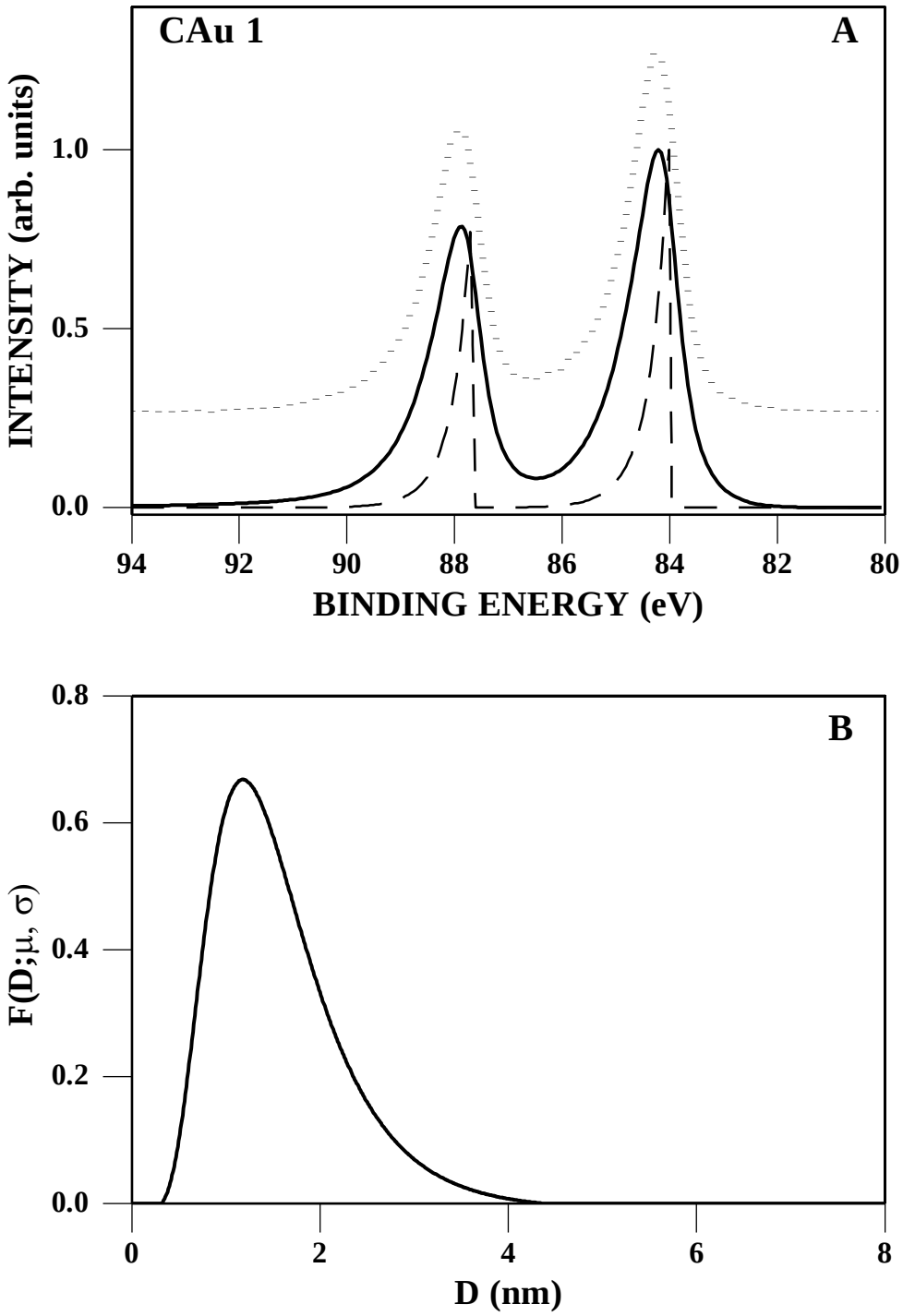

Figure 6.8. *Panel* ***(A):*** *fit of the Au 4f core line of sample CAu 1 after background subtraction. Dashed line: representation of I (BE; μ, σ) function. Solid line: convolution with Voigt broadening eq. (5) Dotted line: Au 4f of the CAu 1 sample. Panel* ***(B):*** *size distribution function obtained from the iterative process.*

6.2.2 XRD Analysis

In order to check the goodness of the proposed model we compared our size distribution with that obtained by XRD analysis. In Figure 6.9 we present the XRD spectra obtained for CAu 2 sample. The spectra of the CAu 1 sample (not reported) do not show any spectral features assigned to the crystalline gold nanoparticles, so we cannot extrapolate information about the size distribution for this sample. On the contrary the CAu 2 spectra show a weak broader peak at around 2θ = 40° that is assigned to the Au (111) and Au (200) peaks. The pronounced broadening of the XRD peak is a clear indication of the small dimensions of the nanoparticles in the samples. [21,22] The XRD size distribution was obtained by using the Warren-Averbach analysis of the Au (111) and Au (200) peaks, after proper deconvolution [23]. The result was expressed as numerical-weighted distribution and it was normalized in order to be comparable with that calculated with our methods.

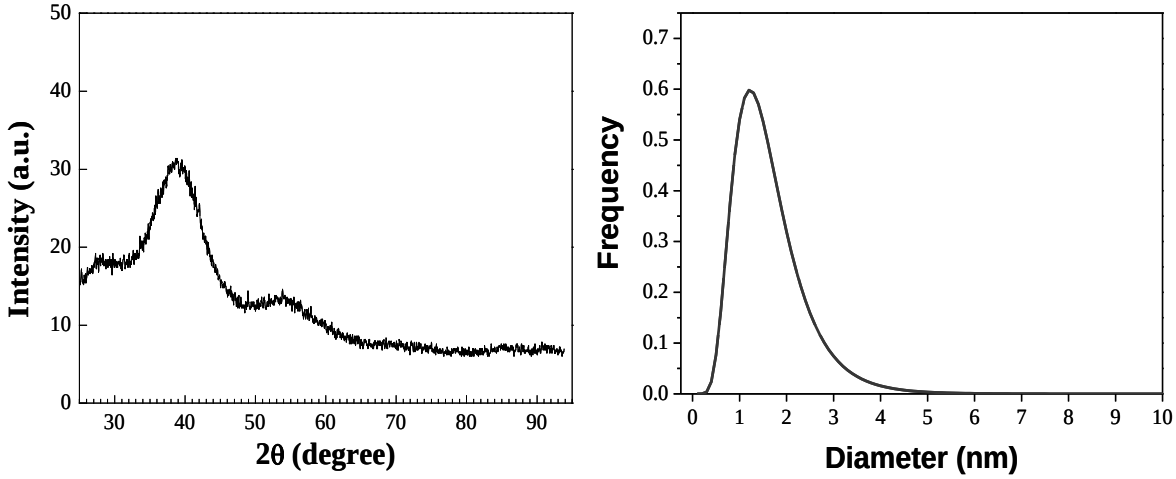

Figure 6.9. *XRD pattern (left) and calculated size distributions (right) of the CAu2sample.*

6.2.3 TEM analysis

Transmission electron microscopy analysis on CAu2 samples reveal some black spots assigned to the gold nanoclusters embedded in the amorphous carbon matrix.

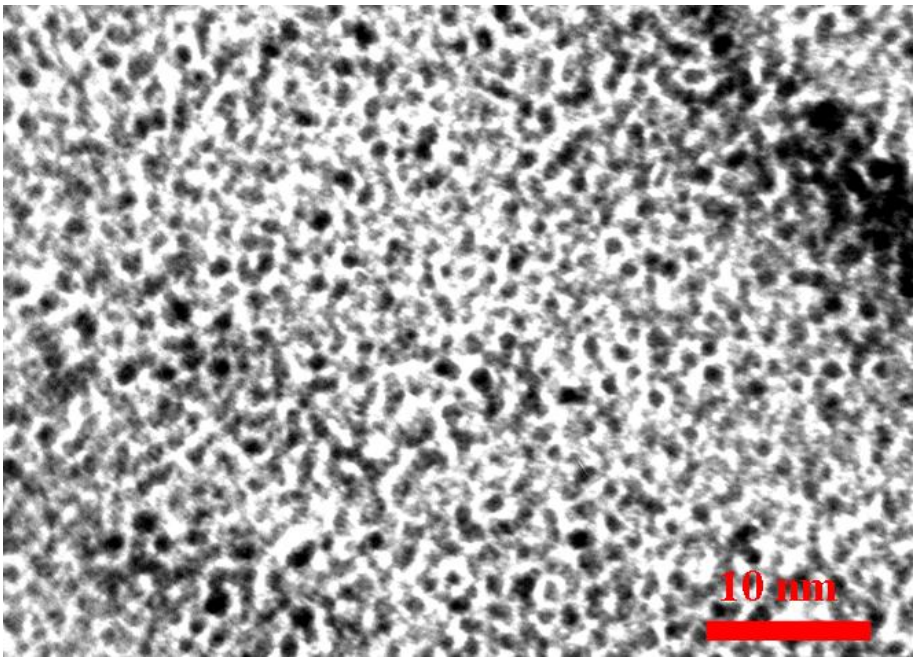

Figure 6.10. *TEM image of the CAu2 sample.*

The nanoparticles size distribution was obtained using the IMageTool software. The results are present in Figure 6.11.

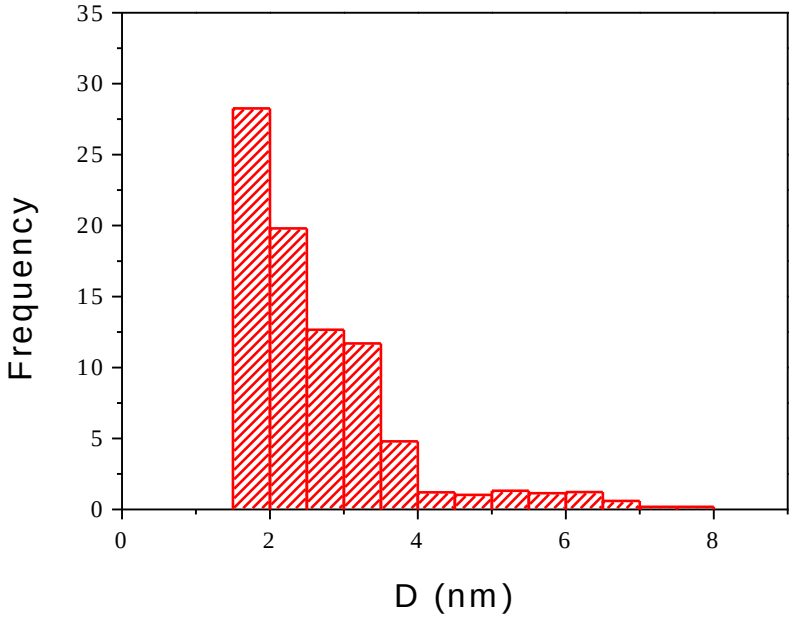

Figure 6.11. *Calculated TEM size distribution of the CAu 2sample.*

As explained in the first section TEM cannot unambiguously detect nanoclusters with dimensions lower than 1.5 nm.

6.2.4 Comparative analysis

The comparative analysis shows a very good match between the size distributions calculated with the three techniques. Differences can be induced by the surface sensitive behaviour of the XPS technique. The outcomes are presented in Figure 6.12, which for sample CAu 2 shows three non overlapped distributions. Despite the apparent difference between the two distributions we find a good match between the results. The range of dimensions in the two distribution are pretty the same.

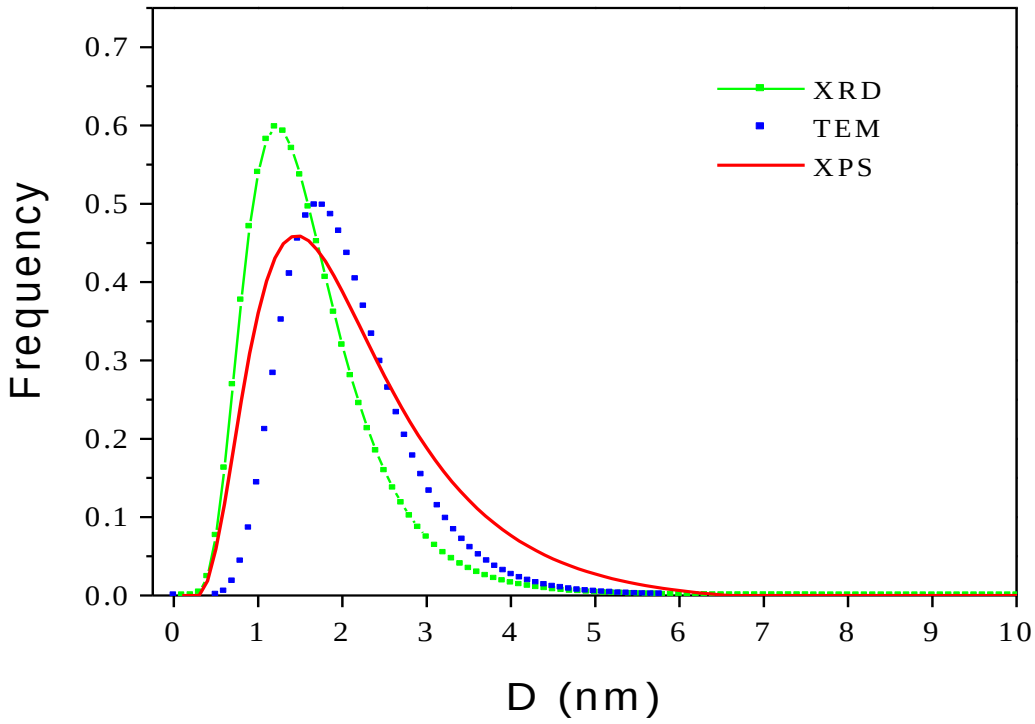

Figure 6.12. *Comparation between the size distributions obtained with XPS and TEM and XRD analysis on sample CAu 2.*

The size distribution calculated by XRD appears narrower and with a higher number of small (D< 2nm) nanoparticles respect to that calculated by our method. These differences however can be explained considering the high noise of the XRD spectrum that leads to a high

uncertainly of the calculated distribution. Moreover the sampling depths of the two techniques are very different: about 5-7 nm for XPS, while the XRD cover all the films thickness and the difference in the size distribution between near surface and the bulk could be significative.
This is an important issue because, the limited sampling depth of the XPS technique is an advantage for all those samples whose properties are influenced especially by the surface as in the case of heterogeneous catalysis or as in electrochemical gas sensors. Finally XPS results to be more sensitive respect to XRD in the case of low Au concentration as in CAu 1 sample. This is an additional advantage of XPS over XRD since it allows good NP analyses of thin catalyst films which are desirable because the lower consumption of precious materials.

6.2.5 References

[1] M. Valden, X. Lai, D.W. Goodman *Science* **281** (1998) 1647.

[2] R. Meyer C.Lemire, S. H. K Shaikhutdinov, H.-J. Freund *Gold Bull*. **37** (2004) 72124.

[3] M. Haruta, S. Tsubota, T. Kobayashi, H. Kageyama, M. J. Genet, B. Delmon *J. Catal.* **144** (1993) 175.

[4] M. Haruta *Catal. Today* **36** (1997) 153.

[5] G. K. Wertheim *Z. Phys. D.* **12** (1989) 319.

[6] H.G. Boyen, Th. Herzog, G. Kastle, F. Weigl, P. Ziemann, J.P. Spatz, M. Muller, R. Wahrenberg, M.G. Garnier, P. Oelhafen *Phys. Rev. B* **65** (2002) 075412.

[7] S. B. DiCenzo, S. D. Berry, E. H. Hartford. *Phys. Rev. B* **38** (1988) 8465.

[8] M.G. Mason, L.J. Gerenser, S.T. Lee *Phys. Rev. Lett.* **39** (1977) 288.

[9] E. Thune, E. Carpene, K. Sauthoff, M. Seibt, P. Reinke, *J. Appl. Phys*. **98** (2005) 034304.

[10] R. W. Cahn *Nature* **389** (1997) 121.

[11] W.E. Warren *X-ray diffraction*. Dover publications: New York, (1990)

[12] http://physci.llnl.gov/Research/scattering/

[13] N. Aldea, P. Marginean, V. Rednic, S. Pintea, B. Barz, A. Gluhoi, B.E. Nieuwenhuys, X. Yaning, F. Aaldea, M. Neumann *Dig. J. Nanomat. Bio.* **1** (2006) 71.

[14] S. Kohiki, S. Ikeda *Phys. Rev. B* **34** (1986) 3786.

[15] I. R. Videnovich, P. Oelhafen *J. Appl. Phys*. **97** (2005) 074308.

[16] C. N. R. Rao, G. U. Kulkarni, A. Govindaraj, B. C. Satishkumar, P. John Thomas *Pure Appl. Chem. Pure Appl. Chem.* **72** (2000) 21.

[17] J. T. Calla, Mangesh T. Bore, Abhaya K. D., Robert J. Davis, *J. Catal.* **238** (2006) 458.

[18]D. Briggs, J. T. Grant *Surface Analysis by Auger and X-ray photoelectron Spectroscopy* IM Pubblications.

[19] T. T. P Cheung *Surf. Sci* **140** (1984) 151.

[20] R. Gampp, *Deposition und Charakterisierung von Metalhaltigen, Amorphen Kohlenwasserstoffilmen zur Anwendung in Sonnenkollektoren* (VDI, Dusseldorf, 1996).

[21] P. Jiang, S. Xie, J. Yao, S. Pang H. Gao *J. Phys. D* **34** (2001) 2255.

[22] P. Zhang, T. K. Sham *Phys. Rev. Lett.* **90** (2003) 245501.

[23] H. P. Klug, L. E. Alexander *X Ray Diffraction Procedures* Wiley-Interscience.

CHAPTER 7

7.1 Characterization of Gold nanoclusters synthesized on carbon nanotubes film: evaluation of the size distributions by means of X-ray photoelectron spectroscopy

7.1.1 Introduction

To fully realize the potential of gold nanoparticles and CNTs as building blocks for functional nanoscale architectures, it will be essential to investigate the interactions between nanoparticles and CNTs in order to configure and model the functional nanoparticle-CNT hybrids for specific applications. In this chapter we use X-ray photoelectron spectroscopy technique to characterize gold nanoclusters formed on the surfaces of thiol functionalized CNT films deposited on a platinum substrate. It is well known from literature that XPS is a powerful instrument to obtain a description of the surface chemistry of the samples. On the other hand, a careful analysis of the Au 4f core lines can also give important information about the dimensions of the nanoclusters. In the previous chapter the gold nanoparticles size distributions was estimated through careful analysis of the lineshape of the Au 4f core line for gold nanoclusters supported on amorphous carbon deposited by co-sputtering of a gold-graphite target. The calculated size distributions were found to be in good agreement with the X- ray diffraction single line profile analysis as well as with the transmission electron microscopy analysis. Because of the great similarity between the two systems, the same algorithm was used to estimate the size distributions of gold nanoclusters "grown" on carbon nanotubes films.

7.1.2 Synthesis of gold nanoclusters on thiol functionalized carbon nanotubes film

The thiol functionalized carbon nanotubes (CNTSH) were synthesized using the preparative showed in the chapter 3. Briefly, drops of highly concentrated suspension of functionalized carbon nanotubes in ethanol were spreads on platinum substrate forming a black uniform film. The sample was then immersed in a diluted $HAuCl_4$ water solution for 4 hours, subsequently

washed with fresh water and then analyzed with XPS (sample CNTAuref). The sample was then irradiated with UV light in air using a Deuterium-UV lamp, 25W with λ_{irr} of 160 nm for 1 minutes (CNTAu1) and 5 minutes (CNTAu5) and then analyzed by XPS (see figure 7.1).

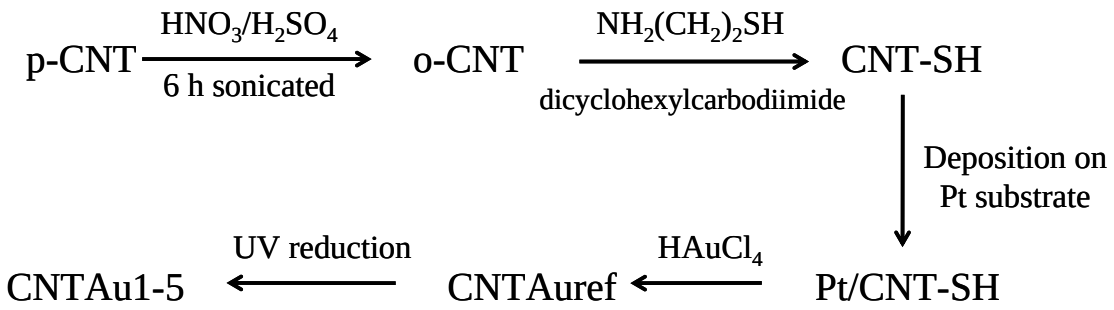

Figure 7.1. *Synthesis of CNTAuref, CNTAu1 and CNTAu5 from the pristine carbon nanotube.*

7.1.3 XPS analysis

The XPS analysis of the CNTAuref is presented in figure 7.2.

The C1s core line is fitted with five components, assigned to sp2 bond (284.45 eV), sp3 bonds (285.3 eV), C-O bonds (286.3 eV), amidic bonds (288.4 eV) and carboxylic bonds (289.5 eV). The O1s core line is fitted with four components. The peak at 531 eV assigned to the carbonyl oxygens of carboxyl and amidic bond, the component at 532.5 eV assigned to C-O, that at 533.5 eV assigned to the unreacted oxydrilic oxygens in carboxylic bonds and finally the component at 535.5 eV is assigned to water molecules adsorbed on the sample.

The S2p core line shows the presence of oxidized sulphur (1), probably formed by oxidative processes during the $HAuCl_4$ adsorption. The doublet at around 163.4 and 165 eV (2) is referred to free thiol groups present on the CNT surface. The N1s core line is centred at 399.7 eV in agreement with the amidic bond position reported in the literature. The quantitative analysis of each element is reported in table 7.1.

In figure 7.3 the Au4f core lines of the three samples are reported. The vertical marker represents the position of pure bulk gold reference at 84 eV. The XPS analysis of the three core lines put in evidence the marked differences between the samples.

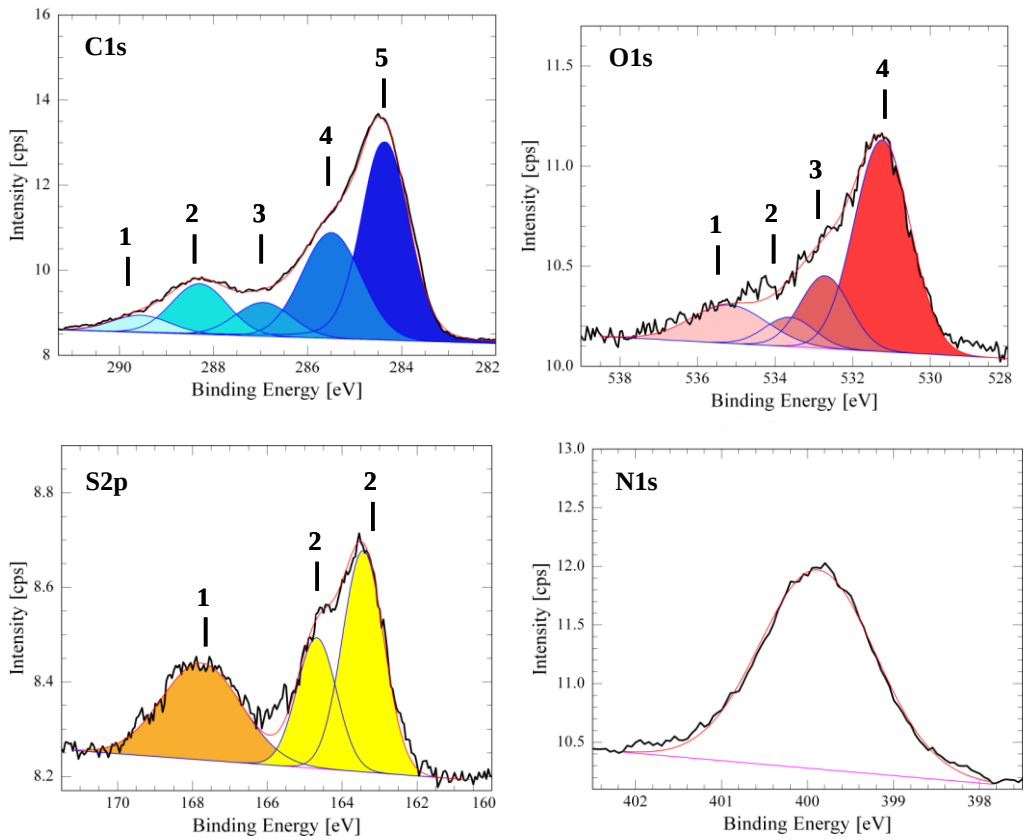

Figure 7.2. *XPS core lines of the CNTAuref sample: C1s, O1s, S2p, and N1s core lines.*

Line	Area	RSF	CONC.%at
Cl2p	58.02	0.760	4.72 %
C1s	281.74	0.296	71.34 %
S2p	33.95	0.560	4.54 %
O1s	69.50	0.730	7.14 %
N1s	58.23	0.440	9.92 %
Au4f	80.02	4.480	2.34 %

Table 7.1*. Quantitative analysis obtained from the XPS analysis on the CNTAuref sample.*

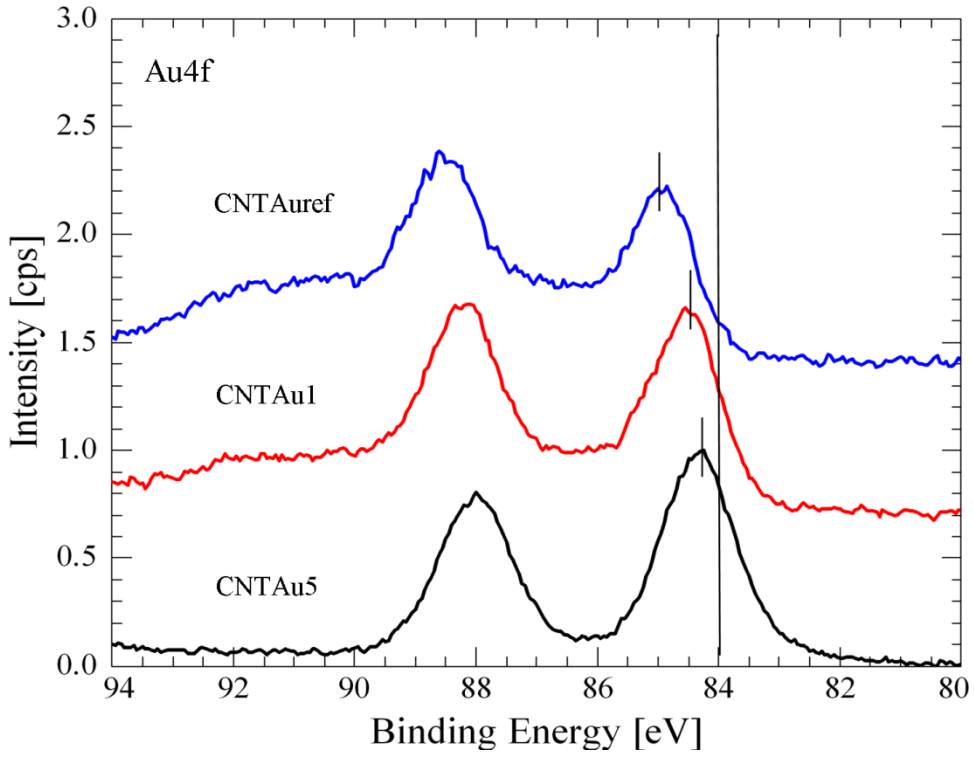

Figure 7.3. *Au 4f core lines of the three samples with different UV irradiation times.*

In particular, the positions of the Au4f$_{7/2}$ signal assigned to the Au^{0} peak are sensibly shifted to higher BE respect to the pure bulk gold. This is an indication of the presence gold condensed in small nanoclusters. Their formation proceeds from the presence of metallic nuclei that acts as centers for the successive grow of the gold nanoparticles. Core line shifts to higher binding energy are obtained for metal nanoclusters with dimensions lower than 5 nm as reported in the literature [12]. For example a shift of around 1 eV in the Au 4f$_{7/2}$ signal, as in the case of the sample CNTAuref, is associated to gold nanoclusters with dimensions around 1 nm [3]. The fit of the Au 4f core lines from the CNTAuref, CNTAu1 and CNTAu5 samples reported in figure 7.4, show the presence of at least three gold chemical species. From data obtained from literature the BE of Au^{III} Au 4f$_{7/2}$ is expected to be around 87-88 eV [4]. For Au^{I} the Au 4f$_{7/2}$ is expected around 86 eV.

Finally, the component at ~ 85 eV is assigned to Au^{0}. The quantitative analysis shows that a considerable fraction of the gold precursor is reduced in metallic form already before the UV reducing treatment. This could be induced by an auto-reduction process initiated by the thiol groups of the CNT support. This process could also explain the presence of oxidized sulphur in the sample.

On the other hand in literature it is described that X, γ, and UV radiations were used to induce a reductions of Au^{III} ions to Au^0 [5, 6]. For example Pucci et al. reported the reduction of $HAuCl_4$ molecules adsorbed on dried vinyl alcohol-containing polymers [7].

The reduction mechanism proposed was a photo-reduction process accelerated by the presence of α hydrogen atoms containing alcoholic group present in the polymer matrix that act as radical scavengers. Following the exhaustive review of Vogler, [8] the gold reduction occurs by formations of chlorine radicals and the successive formation of Cl_2 molecules. This leads to the production of Au^I that undergoes a further disproportionation with the formation of Au^0 and Au^{III}. It must be noted that the carbon nanotubes film contains a great amount of OH, -COOH and water molecules that can accelerate these reactions.

The UV treatments applied to the CNTAuref sample leads to a progressive disappearance of the Au^{III} and Au^I components due to the reduction of the gold precursors and intermediate compounds. At the same time, a visible shift to lower BE of the Au $4f_{7/2}$ maximum is obtained (see figure 7.3 samples CNTAu1, CNTAu5).

According to previous works [9] this reveals that the reducing treatment leads to an increase of the nanoclusters dimensions showing a progressive growth of the gold NP.

Differently from CNTAuref and CNTAu1, the CNTAu5 sample do not show spectral components in the BE range between 90-93 eV, indications of the total reductions of the metal precursor, confirmed also by the disappearance of the chlorine component (data not show) in agreement with the mentioned reduction mechanism. In these three samples the Au $4f_{7/2}$ is shifted respect to the pure bulk Au of about 1 eV, 0.5 eV and 0.3 eV respectively. In order to correlate the BE change to a specific nanoparticle size distribution we extrapolate the Au^0 components from the core line peak fitting. For the size distribution calculation we use the same algorithm presented in the previous chapter [9]. The results of the core line analysis are presented in figure 7.5.

The distributions were estimated by using lognormal functions commonly used to describe nanoparticles populations [10]. As reported by figure 7.5 the CNTAuref sample show a very narrow size distribution centered at around 1 nm. The very low dimensions and narrow distributions of the gold nanoclusters in this sample could be explained with an initial formation of metal nuclei composed by a low numbers of atoms that acts as seeds for the successive grow of the nanoparticles.

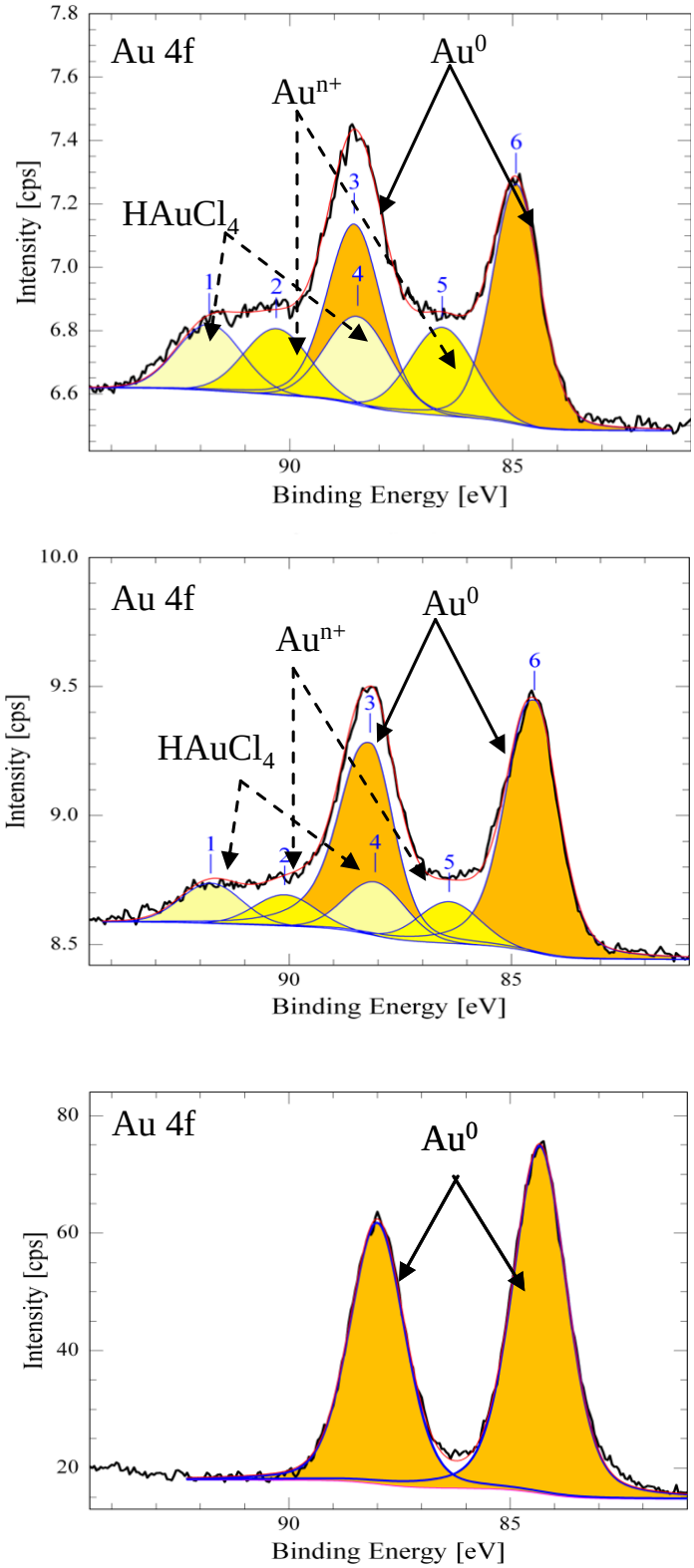

Figure 7.4. *Au 4f core line fitting of the CNTAuref (upper), CNTAu1 (middle) and CNTAu5 (down) samples.*

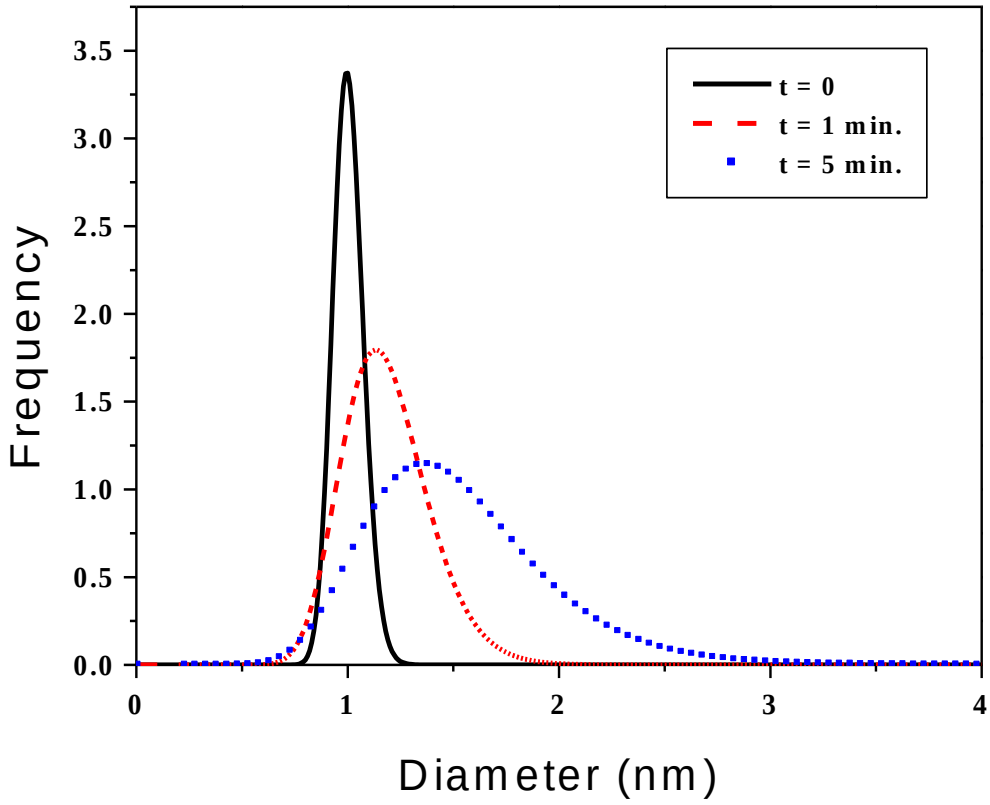

Figure 7.5. *Calculated size distributions from the Au4f core line analysis for the CNTAuref, CNTAu1 and CNTAu5 samples.*

After 1 minutes of irradiation the size distribution becomes broader and centered to a higher nanoparticles dimension. Correspondingly, the amount of oxidized gold decreases.

An increase of UV irradiation to 5 minutes leads to a total reduction of gold with the disappearance of the Au^{III} and Au^{I} components and the formation of a broader NP distribution. The calculated mean nanoparticles size for the three samples (estimated using the $M = e^{\mu+\sigma/2}$ expression) are reported in figure 7.6 (right axes) as well as the estimated Au^{0} fraction present in the sample (left axes) as a function of the irradiation time.

As it appears, the average dimensions of the gold nanoparticles are very low respected to other works reported in the literature [11, 6]. This could be explained with the softer reduction strength of the process used and to the presence of a high concentrations of functional groups and defects on the CNT that act as “cages” for the grown of the nanoparticles limiting their final dimensions.

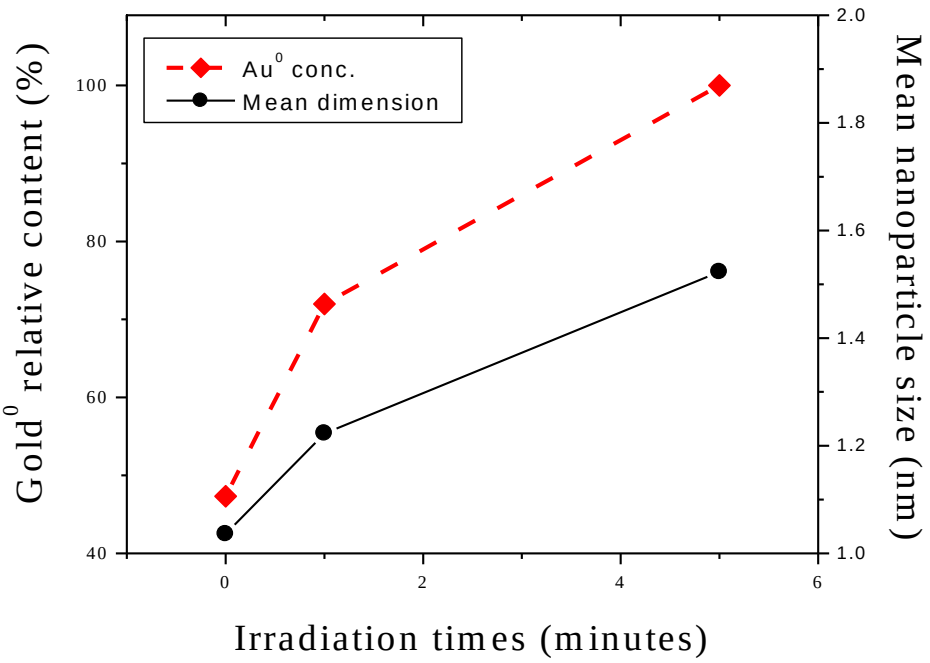

Figure 7.6. *Calculated mean nanoparticles size (right axes) and the total Au^0 concentration (left axes) plotted as a function of the UV exposing time.*

7.1.4 Conclusions

The coupling of the chemical information with the possibility to perform a detailed inspection of the Au_{4f} core line allows a careful description of the Au nanocluster formation on CNT. In particular the presented method allows to obtain information on the nanoparticle size distribution and their modifications as function of the reducing treatments. The possibility to follow the reductions of the precursor from the first stage of the reaction is fundamental to describe the kinetics of the reduction mechanism. The exact knowledge of the reaction process allows tailoring specific NP population for specific applications. Finally, this analytical technique is very useful for systems that cannot be characterized by the traditional techniques as transmission electron microscopy. Examples of these systems are patterned substrates containing small nanoparticles as a carbon nanotubes forest functionalized with small metal nanoparticles or other systems with well ordered structures grown on a substrate. In these cases the TEM analysis requires the destructions of the sample. Differently, the XPS technique allows a direct analysis without complex or destructive sample preparations that could modify their chemistry and structure.

7.1.5 References

[1] M. G. Mason *Phys. Rev. B* **27** (1983) 748.

[2] G. K. Wertheim, S. B. DiCenzo *Phys. Rev. B* **37** (1988) 844.

[3] H. G. Boyen, A. Ethirajan, G. Kastle, F. Weigl, P. Ziemann, G. Schmid, M. G. Garnier, M. Buttner, P. Oelhafen, *Phys. Rew Lett*. **94** (2005) 016804.

[4] S. Suzer *Appl. Spectrosc*. **54** (2000) 1716.

[5] E. Ozkaraoglu, I. Tunc, S. Suzer *Surf. Coat. Tech.* **201** (2007) 8202.

[6] A. M. Showkat, K. P. Lee, A. I. Gopalan, S. H. Choi, Y. C. Nho *Dia. Rel. Mat.* **16** (2007) 1688.

[7] A. Pucci, M. Bernabo, P. Elvati, L. I. Meza, F. Galembeck, C. A. P. Leite, N. Tirelli, G. Ruggeri *J. Mater. Chem.* **16** (2006) 1058.

[8] A. Vogler, H. Kunkely *Coord. Chem. Rev.* **219–221** (2001) 489.

[9] L. Minati, G. Speranza, L. Calliari, V. Micheli, A. Baranov, S. Fanchenko *J. Phys. Chem. A* **112** (2008) 7856.

[10] J. T. Calla, M. T. Bore, A. K. Datye, R. J. Davis *J. Catal.* **238** (2006) 458.

[11] R. Zhang, M. Hummelgård, H. Olin *Materials Science and Engineering: B* **158** (2009) 24.

Conclusions and Perspective

This Thesis presented a study on carbon nanotubes and carbon nanotubes-gold nanoparticles hybrids with the aim to develop new materials with peculiar characteristics for various applications. The first part of this work dealt with functionalization of CNT with thiol functional groups. In chapter 3 CNTs were treated with concentrated mixture of HNO_3 and H_2SO_4 and analyzed with several characterization techniques. XPS analysis reveals the presence of high amounts of oxygen-containing functional groups, particularly carboxylic and oxydrilic groups. The former were used for grafting thiol functional groups on the surface of the CNTs. The functionalized CNTs were then analyzed with different techniques. Thiol functionalized carbon nanotubes showed a great affinity towards gold films and gold nanoparticles. In the chapter 4 we used a different approach for the deposition of functionalized carbon nanotubes on metal substrates. Briefly, the carbon nanotubes were deposited on metal substrates by using an external electric field to induce an orientation and migration of the CNTS on a cysteamine-modified gold electrode. This technique, known as electrophoretic deposition allowed us to obtain a high density of carbon nanotubes on gold and platinum substrates as revealed by SEM and AFM analyses. The carbon nanotube films were then decorated with gold nanoparticles. The resultant CNT/Au films have shown a promising efficiency as SERS substrate for the detection of inorganic ions. In a future development, this substrate could be exploited as electrochemical sensors for the detection of biomolecules. In chapter 5 we showed that carbon nanotubes/gold nanoparticles composite presented a drastic increase of the photoluminescence emission respect to the thiol functionalized carbon nanotubes without the gold nanoparticles. Optical analysis showed that the gold nanoparticles play a fundamental role with respect to the carbon nanotubes/gold composite emission properties. The strong increase of the carbon nanotubes fluorescence in the yellow visible region was explained with a highly efficient energy-transfer between the gold nanoparticles and the emission sites of the nanotubes.

Due to the intense luminescence, functionalized CNT-based systems can be of significant interest for applications in photonics such as the production of lasers, color display and waveguides in the visible.

Finally, these materials have properties of high chemical inertness and reduced toxicity which makes them suitable fluorophores in biological experiments. They have optical properties comparable with that of luminescent semiconductor nanocrystals (quantum dots) which,

especially when cadmium-based, have very high levels of toxicity resulting in dangerous environmental pollution, lack of recycling and high disposal costs.

In chapter 6 XPS analysis of gold nanoclusters deposited on amorphous carbon was presented. In this chapter we have demonstrated that the size distribution of gold NPs in plasma deposited a-C/Au samples can be derived by line-shape analysis of the Au4f photoemission spectrum. The technique works well for the analysis of NP's with size lower than 5 nm. Because the effects of quantum confinement increase with decreasing NP size, XPS is particularly suitable for the characterization of very small NP dimensions (<1.5 nm). This is of great interest because other analytical techniques, such as XRD and TEM, lose their sensitivity in this region.

Finally in chapter 7 gold nanoclusters were directly synthesized on thiol functionalized carbon nanotubes film and characterized by means of X- ray photoelectron spectroscopy. The CNT support was produced by simple spreading of concentrate solution of thiol-functionalized CNT on platinum films. The gold nanoclusters were obtained by adsorption of gold chloride from water solution followed by UV reduction in air. The Au 4f analysis showed a progressive reduction of the gold chloride to Au^0 clusters by increasing the treatment time. Detailed analysis of the Au 4f core line enable us to obtain information on the chemical compositions, as well as information on the nanocluster size distribution modifications after each reducing treatments.

ACKNOWLEDGEMENTS

- ✓ PAM Group, Fondazione Bruno Kessler, Trento.

  Thanks to all my colleagues in particular Giorgio Speranza and Simona Torrengo for the scientific and humane support.

- ✓ Prof. Claudio Migliaresi, Dipartimento di Ingegneria dei Materiali e Tecnologie Industriali, Università di Trento.

- ✓ Dr. Maurizio Ferrari, CNR, Trento.

- ✓ Dr. Michele Vinante, Fondazione Bruno Kessler, Trento.

- ✓ Dr. Sergey Fanchenko, RRC Kurchatov Institute, Moscow, Russia.

- ✓ Dr. Alexander Baranov, MATI-RGTU, Moscow, Russia.

- ✓ Prof. Stefano Gialanella, Dipartimento di Ingegneria dei Materiali e Tecnologie Industriali, Università di Trento.

- ✓ Dr. Barbara Rossi, Dipartimento di Fisica, Università di Trento.

- ✓ Prof. Antonio Miotello, Dipartimento di Fisica, Università di Trento.